NEURAL NETWORK-BASED FAULT DIAGNOSIS OF SATELLITES FORMATION FLIGHT

Shima Mousavi Mirak

A thesis

in

The Department

of

Electrical and Computer Engineering

Presented in Partial Fulfillment of the Requirements
For the Degree of Master of Electrical Engineering
Concordia University
Montréal, Québec, Canada

April 2013

<div align="center">

Concordia University
School of Graduate Studies

</div>

This is to certify that the thesis prepared

By: **Shima Mousavi Mirak**

Entitled: **Neural Network-based Fault Diagnosis of Satellites Formation Flight**

and submitted in partial fulfillment of the requirements for the degree of

<div align="center">

Master of Electrical Engineering

</div>

complies with the regulations of this University and meets the accepted standards with respect to originality and quality.

Signed by the final examining commitee:

<div align="center">

Dr. Luis Rodrigues
_____ Chair

Dr. Amir G. Aghdam
_____ Examiner

Dr. Youmin Zhang
_____ Examiner

Prof. Khashayar Khorasani
_____ Supervisor

</div>

Approved _____
                Chair of Department or Graduate Program Director

_____
                Dean of Faculty

Abstract

Neural Network-based Fault Diagnosis of Satellites Formation Flight

Shima Mousavi Mirak

The main objective of this thesis is to develop a methodology for detecting and isolating faults (i.e. fault diagnosis) in any of multiple reaction wheels that are commonly employed as actuators in a consensus-based virtual structure controlled formation of satellites. In order to accomplish this objective, a two-level fault diagnosis system is developed based on Dynamic Neural Networks (DNNs). In the lower-level of the formation flight system hierarchy, a local fault diagnosis module is available in each individual satellite. In this level, the fault diagnosis system may consist of a dynamic neural network that is trained by using absolute measurements and states of each single satellite. Unfortunately, a local fault diagnosis system may fail to detect the presence of low severity faults. In an individual satellite these low severity faults may not cause any serious complications with the specifications of the overall mission, however they can cause significant impact on the satellite's attitude or rates in a given precision formation flight of a network of satellites. Consequently, in order to detect these low severity faults a fault detection system is required to be designed and developed at the higher-level or the formation-level of the mission hierarchy. Towards this end, the highly nonlinear dynamics of the formation flight and the reaction wheels are modeled by using dynamic multilayer perceptron neural networks. The proposed formation-level DNNs invoke the extended back propagation learning algorithm and are trained based on sets of input/output data that are collected from the relative attitude determination sensors of the 3-axis attitude control subsystems of the satellites. The DNN parameters are adjusted to minimize certain performance indices (representing the output estimation errors).

The capabilities of the proposed DNNs are investigated under various faulty situations, including single and multiple actuator fault scenarios and under high severity and low severity faulty situations. Using a Confusion Matrix evaluation method, it is demonstrated that by using the proposed fault detection and isolation (FDI) scheme,

one can achieve a high level of accuracy and precision in detecting faults. The proposed formation-level FDI system has capabilities in efficiently detecting and isolating actuator low severity faults simultaneously.

To my amzing father, my beautiful mother and my dear brothers,
for their care, love and patience

Acknowledgments

I would like to express my sincere gratitude to my supervisor, Prof. Khorasani, for his professional guidance and continuous encouragement throughout my thesis work. It has been my great honor and privilege to work under his supervision.

I am also thankful to all my colleagues at Concordia University, especially Farshid Faal, for their help and support throughout my research. I owe my deepest gratitude to my dear friends, Maysam Mokarian, Shahrzad Farzin and Behnam Dashtipour for changing my life in their own ways. They have contributed to this work simply by being-in-the-world. I am so lucky for having them in my life.

More than anyone else, I would like to thank my beloved family, especially my beautiful mother and my beloved father who have always been my role model and my inspiration in my life. No word can express how grateful I am for their boundless love and unceasing encouragement and support in every single moment of my life. This work is dedicated to them.

Contents

List of Figures

List of Tables

xviii

Chapter 1

Introduction

Spacecraft formation flight is one of the key technologies for many future space missions. According to the definition in [1] formation flight is a set of vehicles whose dynamics are coupled through common control laws. In the early years of spacecraft flights, only one individual spacecraft was involved in most of the space flight missions and it was controlled via specialized commands from distant ground stations [2]. In order to fulfill multi-task requirements of an individual spacecraft, multiple on board instruments and payloads had to be designed and embedded in the spacecraft structure and this single complex spacecraft was common in spacecraft missions for scientific observations, weather monitoring, global navigation and civil relay communications [3].

One of the main disadvantages of developing a large complex spacecraft is that the cost of design and developing the life cycle of a complex single spacecraft is normally exceedingly high that many nations in the world cannot afford the manufacturing and launch costs of rockets and satellites. On the other hand, increasing the complexity of satellite increases the likelihood of instability of the spacecraft in the mission, such that a minor failure in the spacecraft may lead to a catastrophe in the entire flight

mission [3]. As a solution to these problems, researchers from the US National Aeronautics and Space Administration (NASA) defined the concept of formation flight as grouping of multiple spacecraft such that they can communicate with each other, share payloads and transmit measurements and data in order to accomplish the objective of a single complex spacecraft, which is normally more expensive and less reliable than a group of coordinated but less complex spacecraft [3].

Replacing a single large spacecraft with a group of multiple spacecraft has many advantages: The multiple satellite approach is simpler and less expensive to manufacture and it provides a high degree of reconfigurability and redundancy in case of single vehicle failure or malfunction. Formation flying of spacecraft approach is adaptive to the failure in any of individual satellites and the failed satellite can be replaced incrementally. Using a group of multiple spacecraft in the formation flight also provides more flexibility in the mission, such that new technology can be included in the preexisting missions [4].

One of the essential problems in formation flying missions is control. In formation flight controller design, the size of the formation must be defined firstly, and the task also requires collision avoidance calculations, minimum amount of fuel consumption and minimum sensor measurements and data communication. The essential part of control problem in a group of spacecraft is developing control architectures and advance trajectory planning techniques [3].

In [87] five basic formation control architectures are defined namely: Multiple-Input, Multiple-Output (MIMO), Leader Follower (L/F), Virtual Structure (VS), Cyclic and Behavioral. In the Multiple-Input, Multiple-Output architecture, the formation is considered as a multiple-input, multiple-output plant and the formation controller is designed by using the dynamic model of this formation plant. In the L/F architecture, using a hierarchical approach, the problem of formation control

is reduced to the individual tracking problem [1]. In the VS, the group of multiple satellites behaves like a rigid body. Motions of the virtual structure and constant specified orientations and positions of the virtual structure are used to determine the trajectory that each individual satellite needs to follow. The formation control in cyclic architecture is obtained by connecting individual controllers using cyclic algorithms. In Behavioral architecture, the output of multiple controllers is combined to achieve the desired different behaviors.

One of the essential problems that are being investigated recently in the literature is the problem of Fault Detection and Isolation (FDI) for formation flight of satellites. By definition, fault detection is the process of detecting the fault occurrence in the system based on malfunctions or abnormalities in the system behavior. Once the fault is detected, the next step is fault isolation. In this step, the faulty component is identified. There are two main FDI methods available in the literature, namely: model-based approach and process history-based approach using either qualitative or quantitative modeling [9], [152].

Development of intelligent and learning-based methods for autonomously detecting faults in a formation flight, with minimal support and intervention of ground-based operators is indeed a challenging research field. The faulty component (either a faulty actuator or sensor) must be detected and isolated as early as possible, before it could lead to and result in serious damage or fatal failure in the formation control subsystem. In learning-based approaches [10] such as neural networks and fuzzy systems, a realistic model of component does not need to be provided. Due to capabilities of neural networks to cope with nonlinearity, complexity, uncertainty and noisy and corrupted data, they have been widely applied in domain of fault detection [149], [23].

Static nonlinear systems can be modeled by standard multilayer perceptron networks, but, in order to represent dynamic properties of a system, one needs to employ

a dynamic neural network [46]. Dynamic neural networks are responsive to time varying signals due to their capabilities of internally generating and embedding memory. In recent years, dynamic neural networks have been widely used in different fault identification and fault detection and isolation applications [5], [6], [7], [8].

Attitude control subsystem of a satellite is responsible for orienting satellite toward the desired attitude and stabilizing it despite the external disturbance torques. The propulsion system plays an important role in formation flying missions. Gyros and reaction wheels can play the role of attitude control in most of formation flight missions. The actuators which are responsible for the satellite attitude control are three reaction wheels on three axes of each satellite. Their main functionality is to provide reaction torques for a spacecraft and store angular momentum [82].

Developing an FDI system for detecting and isolating faults in reaction wheels of a formation flying of spacecraft is a challenging problem. The desirable autonomous FDI system must be capable of detecting faults and isolating the faulty reaction wheel in the group of satellites.

1.1 Literature Review

1.1.1 Fault Detection and Isolation

Development of fault detection and isolation methods for autonomously detecting faults in a formation flight mission, with minimal support and intervention of ground-based operators is indeed a challenging research field. The faulty component (either a faulty actuator or sensor) must be detected and isolated as early as possible, before it could lead to and result in serious damage or fatal failure in the formation control subsystem.

Detecting and isolating faults can be achieved by two main approaches, namely

model-based and history-based approaches [10], [11] and [12]. In model-based approaches, a normal operating model of the system is constructed based on the prior mathematical knowledge about the system. The output of this model is compared with the actual output of the system, to generate the residual signal. This residual signal is used as a fault indicating signal, that is, if the residual signal is close to zero, the system is healthy and if the residual signal is distinguishably greater than zero, the system is faulty. In history-based approach it is assumed that a large amount of historical information is available. This data can then be presented as *a prior* knowledge to the diagnostic system through feature extraction methods [12]. A detailed classification of fault diagnosis methods is depicted in Fig. 1.1.

In quantitative models, the physical understanding of the process is expressed in
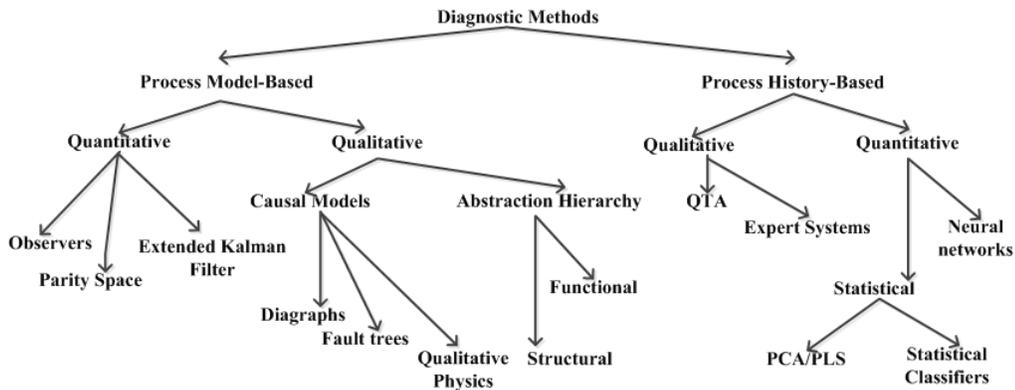
Figure 1.1: Classification of diagnostic algorithms [9].

terms of mathematical input-output relationships in the system [10]. In parameter estimation method, it is assumed that the model structure is known, however the model parameters are unknown and time varying. This method is especially suitable for multiplicative faults and additive faults on the input and output signals. Using this method, very small changes such as slowly developing and fast developing faults are detectable [12]. In state estimation methods, model structure and model parameters must be known accurately. This method is especially suitable for additive fault

5

detection, however using this method only relatively large faults are detectable. In parity equations method, model structure and model parameters must be known and must be fit the process well. This method is especially suitable for additive faults. Using this method some low severity faults can be detected. In case of abrupt faults, state estimation and parity equation methods react faster than parameter estimation method.

In qualitative methods, the physics of the process is expressed in terms of qualitative functions such as causalities or IF-THEN rules centered on different units in a process. The prior knowledge of physics of the system in the causal models can be represented in different forms, such as digraphs, fault trees, qualitative physics and abstraction hierarchies [10]. In [13] fault detection in a satellite system is performed based on a fault tree approach and the causes of a fault is determined by using the same method. In [14] two correlation models are proposed to approximate the complex correlation among sensor measurements of general systems.

The problem of fault detection and isolation in the attitude control subsystem of a satellite has been studied in [15], [16], [17], [88] and [18] recently. In [17] a Multi-Hypothesis Extended Kalman Filter (MEKF) for detection and identification of sensor and actuator failures is proposed. In [15] the FDI is accomplished by using the Interactive Multiple Models (IMM) approach. Towards this end, a bank of interactive multiple Unscented Kalman Filters (UKFs) is developed. In [88] a fault diagnosis technique is developed based on the interacting multiple model (IMM) algorithm for partial (soft) or total (hard) reaction wheel failures in the spacecraft attitude control system (ACS). In [20] a decentralized state estimation method is applied to estimate the states of the formation flying mission. In [18] a set of detection filters are designed whereby through a combination of residuals the reaction wheel FDI decision making is accomplished successfully. Since many modeling errors appear in the mathematical

model of the system, the model-based FDI problem may result in having false alarms or missing the fault effects [19].

The process history-based methods are classified into two categories, namely: qualitative and quantitative. Qualitative history features can be extracted by expert systems and Qualitative Trend Analysis (QTA). Most faults in the system leave a trend in the faulty actuator or sensor. This trend can be used to detect the underlying faults in the system, before they lead to major failures in the system [11]. Expert systems need an extensive detailed database and process experts. These methods are time consuming to develop due to large amount of information and rules and their main disadvantage is the uniqueness of knowledge and the necessity for updating rules [21].

Statistical and non-statistical classifiers are used to extract quantitative historical information. There are three main statistical feature extraction methods namely Principle Component Analysis (PCA), Partial Least Squares (PLS), and statistical pattern classifiers [11]. Quantitative feature extraction approaches essentially formulate the fault diagnosis problem as a pattern recognition problem. More details on quantitative history-based approaches have been provided in [9], [10], [11].

In [90] a robust fault detection and isolation (FDI) scheme for a general nonlinear system using a neural network-based observer is developed. Both actuator and sensor faults are considered. Two recurrent neural networks are employed to identify general unknown actuator and sensor faults. In [91] a practical solution to the problem of robust fault detection and isolation (FDI) for faults affecting the thrusters of a satellite system is proposed. This approach is based on both state estimation of an accurate linear model of the satellite system and unknown input de-coupling to achieve robust FDI in presence of severe dynamic uncertainty during main engine deployment.

In [92] a systematic and transparent methodology within a hierarchical fault diagnosis framework for multi-platform space systems is proposed. A Bayesian network-based hierarchical fault diagnosis methodology is proposed in [92] that allows fuzzy rule-based reasoning at different components in the hierarchy. In [100] a multi-level fault diagnosis methodology utilizing fuzzy rule-based reasoning is proposed to enhance the level of autonomy in the fault diagnosis at the ground station. In [89] a state space approach is used and a nonlinear-in-parameters neural network (NLPNN) is employed to identify the additive unknown reaction wheel faults. This FDI scheme is based on a hybrid model (composed of an analytical nominal model and a neural network model) of the nonlinear system. In [94] a fault tolerant diagnosis system for the RADARSAT-1 attitude control system (ACS) telemetry is developed. The proposed system is using computational intelligence to detect and isolate faults and determine the cause of failures from the telemetry data time series history using functional models of the satellite ACS.
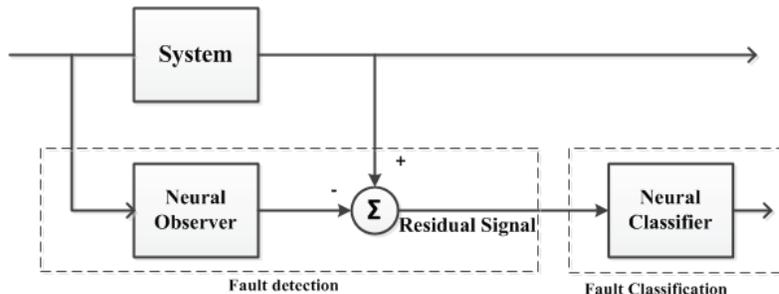
Figure 1.2: General structure of neural network-based FDI scheme.

1.1.2 Neural Networks for Fault Diagnosis

An important class of non-statistical classifiers is neural networks. In learning-based approaches such as neural networks and fuzzy systems, a realistic model of component does not need to be provided. Due to capabilities of neural networks to cope

with nonlinearity, complexity, uncertainty and noisy and corrupted data, they have been widely applied in the domain of fault identification [36], [37], [38], [39] or fault detection [22], [23], [42], [48], [24].

The general structure of neural network-based FDI is depicted in Fig. 1.2. Generating residual signals is the key part in detecting faults in a process. The dynamic model of behavior of the system is generated by using a neural network. The difference between the output of the neural network and the actual output of the system is considered as the fault indicating signal (i.e. the residual signal). Generally, instead of developing multiple linear models of the system for several operating points, it is more advantageous to develop a nonlinear model of the system that works in a wider range of operating conditions [9].

Sorsa in [23] utilized a multilayer perceptron network with hyperbolic tangent as the nonlinear element for detecting faults in a realistic heat exchanger-continuous stirred tank reactor system. In [25] the application of artificial neural networks for detecting and isolating faults in robotic manipulators is discussed. In [25] the dynamics of the robotic manipulator is reproduced by using two neural network-based approaches namely: multi-layer perceptron (MLP) neural network and radial basis function network (RBFN). In [26] the FDI scheme proposed in [25] is applied to generate and analyze the fault indicating residual signals in multiple cooperative manipulators.

The application of neural networks as a solution for the problem of fault detection and isolation has been widely discussed in the literature. Neural networks have been proposed for classification and function approximation problems. In general, neural networks that have been used for fault diagnosis can be classified into two groups, based on: (i) the architecture of the network such as radial basis functions; and (ii)

the learning strategies such as supervised and unsupervised learning [11]. In the supervised learning algorithms, using a predefined topology for the neural network, the connection weights have to be determined using the mismatch between the actual and the desired output values. In that sense, supervised learning algorithms are suitable choices for fault classification applications. The most popular neural network learning strategy in the literature is the back-propagation algorithm. The problem of fault diagnosis based on back-propagation learning method has been addressed in [139], [140], [141], [142].

Most of the work on improvement of performance of standard back-propagation algorithm are based on explicit presentation of features to the network. In [143] the performance gains of neural networks are determined through the incorporation of functional inputs in addition to the normal inputs to the neural networks. In [144] the performance of the network is improved and the network training time is reduced through data processing and filtering. In [145] a combination of feedforward neural networks and a recurrent neural network is used for better performance. In [146] the integration of neural networks and expert systems is applied for better fault diagnosis. As an improvement to the standard back-propagation learning method, basis functions generating bounded decision regions could be better suited to the problem of fault diagnosis [11]. In [147] radial basis neural networks are considered as a solution for the fault diagnosis problem.

In [148] a wavenet is proposed as an improvement for standard back-propagation method for the problem of fault diagnosis. Wavenet is a neural network with one hidden layer and its basis functions are drawn from a family of orthonormal wavelets. One important advantage of the wavenet is that due to the orthogonality property of the wavelet basis functions, the nodes may be added or removed without retraining the network.

During recent decades, most of the work in the domain of neural networks has focused on static feed-forward neural networks. These networks have many applications in the field of pattern recognition where both input and output vectors represent the spatial patterns and they are independent of time. The main motivation to develop dynamic neural structures is that the signal delays are omnipresent in the brain and play an important role in neurobiological information processing. In addition to better representation of neurobiological neurons, the dynamic neuron also offers better computational capabilities as compared to the static neuron.

In [149] a neural network approach to design of a robust fault diagnosis system is proposed. In this work a neural observer scheme is developed based on dynamic multi-layer perceptrons with a mixed structure. In [150] a fault detection and isolation (FDI) strategy based on a Dynamically Driven Recurrent Neural Network (DDRNN) architecture is proposed This fault diagnosis method is applied for detecting and isolating faults in case of actuator/thruster failure in a satellite.

In [28] the dynamics of the attitude control subsystem of a satellite is modeled by using a recurrent neural network called Elman's network. In this network, there is a feedback from the output of the hidden layer to the input of the hidden layer. This dynamic feedback allows the Elman's network to learn the time-varying patterns and dynamic features of the ACS model. In [30] an adaptive nonlinear parameter estimation technique is used based on a highly accurate dynamic model of a reaction wheel. The well-known standard back-propagation algorithm and back-propagation through-time algorithm were employed inside the neural adaptation algorithms to obtain the required performance. To make the optimization feasible for on-line application, the optimal estimation functions are approximated by MLP neural networks. In [95] a hierarchical dynamic neural network-based fault detection and isolation (FDI) scheme

for pulsed plasma thrusters (PPTs) that are employed in the attitude control subsystem (ACS) of satellites tasked to perform formation flying (FF) missions is developed.

In [27] a Dynamic Multi-Layer Perceptron (DMLP) neural network that is proposed in [32], [33], [34], [35] is used to detect faults in the attitude control subsystem of a satellite. In this work, a generalized architecture of the same dynamic neuron model is considered. In this type of neural network, instead of using of a global feedback structure, dynamic neurons are used in feed-forward neural network architecture. In [151] the same dynamic neural network architecture is used to detect faults in a highly nonlinear dynamic system corresponding to an aircraft jet engine.

1.1.3 Formation Flying of Spacecraft

The concept of formation flight of satellites is a critical technology for future space missions. One of the main problems in the field of formation flying of satellites is guidance. Based on its definition, formation flight guidance is the generation of any reference trajectory that is used as an input for a formation member's relative state tracking control law [1]. The problems in the field of formation flying guidance are divided into two main categories, namely deep space (DS) formation flight missions and planetary orbital environments (POE) missions. In deep space, relative spacecraft dynamics reduce to a double integrator form [100], but in the POE the spacecraft are subject to environmental disturbances and significant orbital dynamics. A satellite orbiting around the Earth is affected by many perturbing forces, torques and disturbances. Due to the non-symmetric and non-homogenous characteristic of the Earth, gravitational perturbation (J_2) [134], [135], and gravitational torque [55] highly affect satellites in lower altitudes. In lower altitude the atmospheric drag, is one of the dominating forces [134], [55]. Other major perturbing factors could be listed as solar

radiation [136] and solar wind [134], the magnetic field of the Earth, and the gravitational force of the Moon and the Sun [137], [138]. Fig. 1.3 shows these perturbing forces and torques and compares them in terms of severity.

In [96] the problem of formation reconfiguration is precisely defined and it is
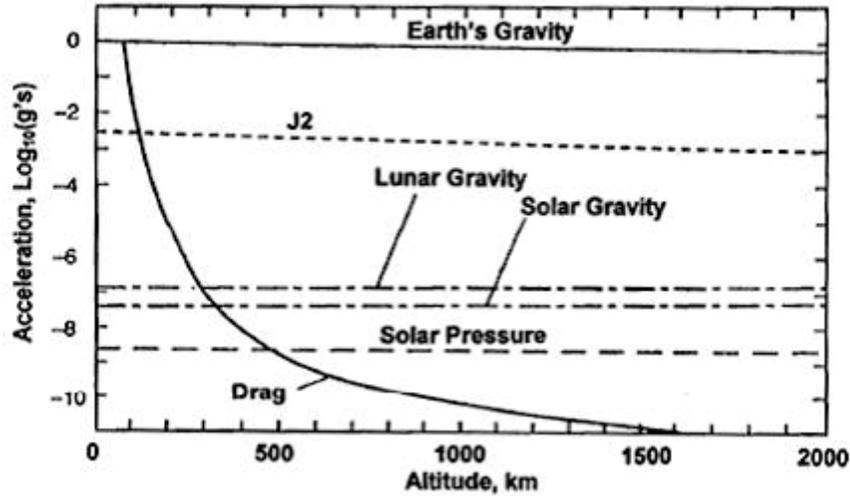
Figure 1.3: The influence of the disturbing forces at different altitudes [143].

reduced to the problem of permutation groups. In this case the fuel optimal reconfiguration trajectories are straight lines with "bang-coast-bang" control law and collision avoidance is addressed by sequentially moving the spacecraft. Given a new configuration optimal, collision avoidance-constrained reconfiguration trajectories are developed in [97], [98], [99]. In the POE dynamics are more complicated and as a result, other methods are proposed for solving the reconfiguration problem. In [101], [102], [103], [104] the problem of formation flying reconfiguration is solved by using optimal control including linear programming and primer vector theory. In [105] Hohmann transfers method and in [106] and [107] Lambert's solution is applied for solving the problem of reconfiguration in formation flights. Gauss' variation of parameters equation [107], [108], [109], [110] and multi-impulse, sub-optimal methods [111], [112], [113] have also been investigated.

One of the other problems in the field of formation flying of satellites is developing and designing of formation control techniques associated with stability analysis of the tracking control laws. In general the formation size, precision and dynamic environment all affect the formation flying controller development [87]. The first problem in the field of formation flying controller development is the formation controller architecture. In [87] five different controller architectures are defined namely: Leader/ Follower (L/F), Multi-Input/ Multi-Output (MIMO), Virtual Structure (VS), Cyclic and Behavioral structure.

In the leader follower architecture, a hierarchical arrangement of individual spacecraft controllers is used that reduces the problem of formation flying control to an individual tracking problem [87]. Most of leader/follower algorithms in the literature discuss a single leader/follower control algorithm in which all spacecraft in the formation follow the same leader. The other common architecture is the one in which each satellite follows its preceding satellite. It is normally assumed that if the follower control laws are stabilizing, then the leader/follower connection of these controllers becomes stable too. The problem of leader/follower deep space formation controller design is studied in the following papers. In [114] and [115] feedback linearization method and linear matrix inequalities (LMI) are combined to design a robust and switched controller for avoiding control saturation. In [116] and [117] a variety of control techniques including proportional/derivative (PD), time-optimal and mixed fuel-time optimal are applied. [118] develops a rule-based control law for synchronizing the rotational motion of multiple spacecraft in the mission.

The problem of leader/follower controller design in the POE is discussed in the following papers. In [119] separate discrete-time controllers are designed for in-orbital plane motion and out of plane motion. In [120] a similar decoupled controller is

designed for GEO orbits. In [121] a discrete-time LQ controller is designed for disturbance rejection and a feedforward controller is designed for providing non-equilibrium point control offsets. Considering nonlinear control, [122] and [123] design position feedback and output feedback controllers, respectively, for Keplerian relative orbital dynamics.

In the virtual structure architecture, the overall network of satellites is considered as a whole virtual rigid body. The motion of the virtual structure and the positions and orientations of individual spacecraft within the formation are used to generate reference trajectories for the spacecraft to track by using individual spacecraft controller.

Two types of virtual structures are studied in literature:, namely Iterated Virtual Structure (IVS) and Guidance Virtual Structure (GVS). In the IVS a formation structure is fit to the current spacecraft positions at each time. The spacecraft then track desired states with respect to the fitted structure. The GVS consists of an initial structure fitting step, followed by the prescribed motion of the structure to generate desired spacecraft trajectories [87]. Different fitting algorithms are discussed in [124], [125], [126] and [127]. Similar to the L/F, a formation controller in the cyclic architecture is formed by connecting individual spacecraft controllers. In Cyclic architecture, unlike leader/follower architecture, the controller connections are not hierarchical [87]. In [128] a multi-neighbor strategy is proposed, in which each spacecraft controls itself with respect to the center-of-mass (COM) of a subset of neighboring spacecraft. A similar approach has been used in [129] and [130].

In the behavioral architecture the outputs of multiple controllers designed for achieving different and possibly competing behaviors are combined. A behavior is defined to be an objective such as collision avoidance or move-to-goal functions that the spacecraft must individually or collectively perform [87]. Formation maintenance

is one of the behaviors that must be fulfilled during the formation [129], [130].

In the multiple-input, multiple-output (MIMO) architecture, formation controllers are designed by using a dynamic model of the entire formation system. In this approach, the formation is treated as a multiple-input, multiple-output plant. Within this problem formulation, all the methods of modern control may be applied to formation control. In [131] a minimal state space realization of formation relative states is developed and a LQR controller is designed. In [132] each spacecraft has a full-state LQC estimator that requires communicated information to function. In this paper a local estimator is augmented so that less information communication is needed among satellites in the formation. Nonlinear and constrained model predictive control (MPC) for MIMO architecture has been developed in [133].

1.1.4   Objective of the Research

The main objective of this work is to propose a method for detecting and isolating faults in reaction wheels of the formation flying satellites. In order to design the desirable dynamic neural network-based FDI system, different FDI methods that are used in the literature are reviewed and analyzed. Then the dynamics of each satellite and the interactions among satellites are modeled. The group of satellites is controlled based on the decentralized formation flying control via virtual structure method [31]. Finally, a reliable FDI scheme is proposed in order to detect and isolate faults in a formation flying of satellites and the capabilities of the proposed FDI method is evaluated under different faulty conditions. the general structure of our proposed FDI scheme is depicted in Fig. 1.4. In the last part of this thesis, a neural network-based method is used to determine fault type and the severity of the fault that occurs in the reaction wheels of spacecraft in formation flight.
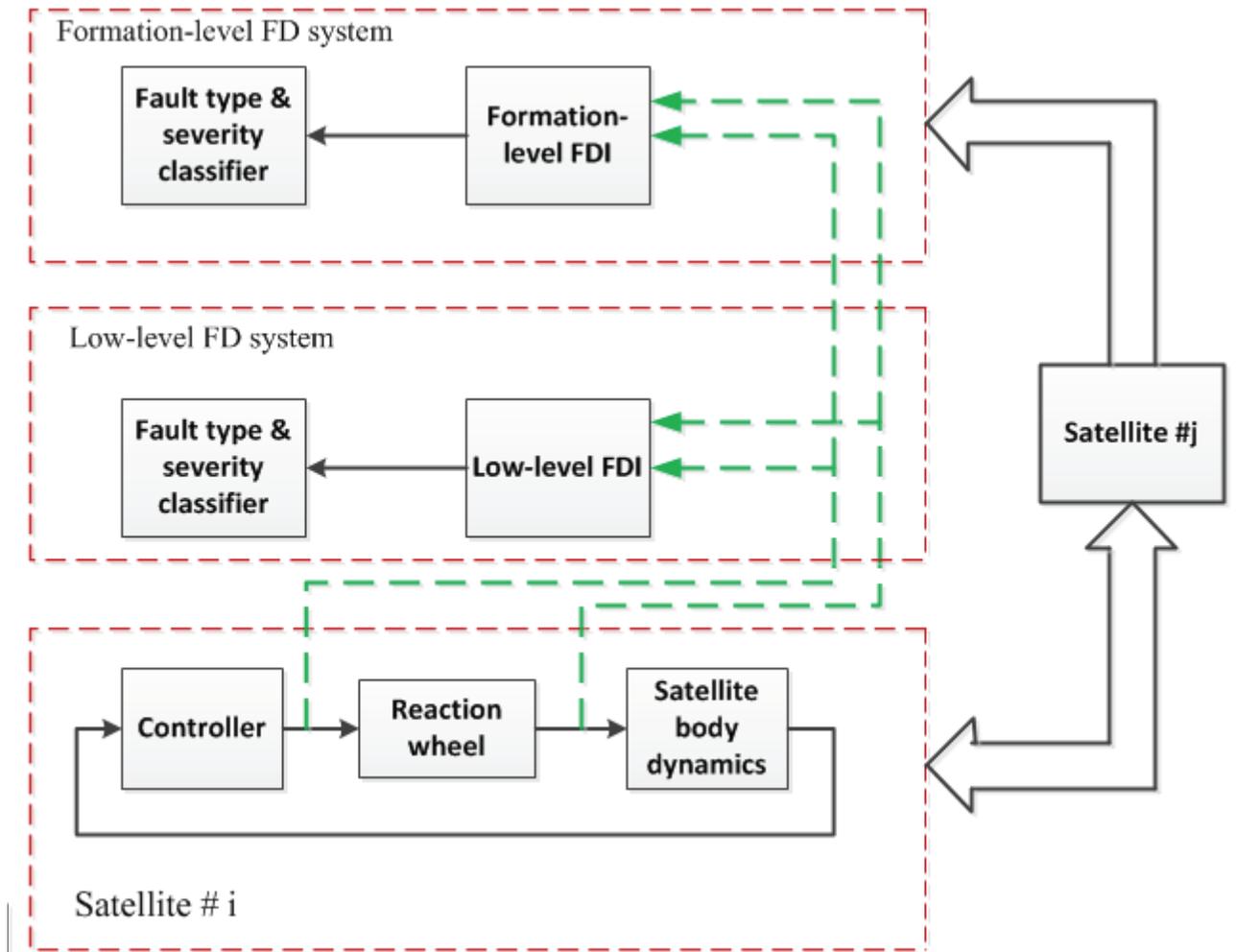
Figure 1.4: Structure of a two-level FDI system for a formation flying of satellites.

1.2 Contributions of the Thesis

The contributions of the work developed in this thesis are detailed as follows:

- A novel Fault Detection and Isolation (FDI) scheme for the Reaction Wheels (RWs) of the Attitude Control Subsystem (ACS) of formation flying satellites is proposed. Single satellite fault detection systems (i.e. local FD systems), can detect high severity faults and attitude deviations, however, they fail to detect low severity faults. These low severity faults may not cause any serious difficulties with the specifications of the overall single satellite missions, however they can cause significant impact on the satellite's attitude or rates in a given precision formation flight of a network of satellites. Therefore, in order to improve the fault diagnosis system in a network of satellites, a novel fault detection scheme is proposed. Using this FD scheme, even low severity faults can be detected and isolated before they cause any catastrophic failure in the formation system. The capabilities of the proposed method have been investigated through different faulty scenarios. By means of proposed Dynamic Neural Networks (DNNs) the proposed FDI system is capable to detect and isolate the fault occurrence in any of multiple actuators (i.e. RWs).

- The results obtained show high level of accuracy (98%) and precision (100%) and the mis-classification rate and false faulty parameters are small (2%). Therefore, the proposed DNN technique fulfills the expected requirements of accuracy and precision with minimum false alarms and mis-classifications.

- In this work a decentralized FDI scheme is proposed. The previous actuator fault diagnosis systems developed for a single satellite in the literature [43], [150], [13], [18], [29] use the absolute local measurements of an individual satellite to detect fault occurrence in the actuators. In those methods, each satellite

is only capable of detecting its own faults. In formation flying missions, fault occurrence in any of the satellites in the formation may influence the orientation of the other satellites as well, and even when the fault is too severe it may result in a failure in the whole mission. Therefore, in a formation flying missions, developing a decentralized fault diagnosis method, in which each agent in the formation is capable of detecting faults in its own actuators or actuators in the neighboring satellites is the major contribution of this thesis. A formation flying of satellites including n satellites, $\#1$, $\#2$, $\dots \#i \dots \#n$ having ring topology are tasked to perform a formation flying mission. In the first fault diagnosis scheme, a DNN-based fault diagnosis system is implemented along each axis of each spacecraft in the formation and the DNN-based fault diagnosis system in each spacecraft is trained using relative attitude measurements of that spacecraft with respect to its adjacent neighbor (for example DNNs in satellite $\#i$ are trained based on relative attitude measurements of satellite $\#i$ and satellite $\#(i+1)$). Two fault detection schemes are investigated in this work.

In the first scheme, when a fault occurs in one of the actuators of any of the satellites (for example satellite $\#i$) in the formation, the DNN-based fault diagnosis system in the faulty spacecraft can detect the faulty actuator immediately. Since the DNNs in the neighboring satellite (satellite $\#(i-1)$) is trained based on the relative attitude measurements of satellite $\#(i-1)$ with respect to the satellite $\#i$, when a fault occurs in satellite $\#i$ it affects the attitude of satellite $\#i$ and consequently the relative attitude of satellite $\#i$ with respect to the satellite $\#(i-1)$. Hence, the DNN-based fault diagnosis systems in satellite $\#(i-1)$ also gets an impact of the fault after a time delay.

In the second fault diagnosis scheme, the DNN-based fault diagnosis system along each axis of each spacecraft in the formation is trained by using relative

attitude measurements of that spacecraft with respect to its two adjacent neighbors in the formation. In this scheme, the DNNs in satellite $\#i$ are trained by using the relative attitude measurements of satellite $\#i$ with respect to its two adjacent neighbors $\#(i-1)$ and $\#(i+1)$. Therefore, when a fault occurs in one of the actuators of satellite $\#i$, the DNN-based fault diagnosis system in satellite $\#i$ can detect the fault immediately, but since the DNNs in satellite $\#(i-1)$ are trained based on relative attitude of satellite $\#(i-1)$ with respect to satellite $\#i$ and satellite $\#(i-2)$, when a fault occurs in satellite $\#i$ it affects the attitude of satellite $\#i$ and consequently the relative attitude of satellite $\#i$ with respect to satellite $\#(i-1)$. Therefore, DNNs in satellite $\#(i-1)$ can also detect the fault occurrence in satellite $\#i$ after a time delay. Also, since the DNN in satellite $\#(i+1)$ is trained using relative attitude of satellite $\#(i+1)$ with respect to satellite $\#i$ and satellite $\#(i+2)$, when a fault occurs in satellite $\#i$, it affects the attitude of satellite $\#i$ and consequently the relative attitude of satellite $\#i$ with respect to satellite $\#(i+1)$. As a result, when a fault occurs in one of the actuators of satellite $\#i$, the DNNs in satellite $\#(i+1)$ can also see the effect of fault after a time delay. This second scheme requires more information exchange among spacecraft in the formation, but it enhances the precision and accuracy of fault detection and decreases the false alarms and in the second scheme, the neighboring satellites in the formation can detect the fault with smaller time delay.

- In this work, after detecting the health status of the reaction wheel and the fault occurrence time, a neural classifier is proposed to determine the fault type (bus voltage fault, motor current fault or viscous temperature fault) and fault severity.

1.2.1 Outline of the Thesis

The organization of this thesis is as follows: In Chapter 2, a classification of available fault diagnosis methods in the literature is provided and the structure of the Dynamic Neuron (DN) and Dynamic Neural Network (DNN) that are used in this work are described. In the next section, the detailed model of the formation flying of satellites and the decentralized control algorithm that is incorporated is briefly described. In Chapter 3, the decentralized fault detection scheme for the formation of flying satellites is described and the capability of the proposed scheme in detecting and isolating faults is evaluated under different faulty cases. In Chapter 4, a method for fault type classification and fault severity estimation is proposed. Finally, the conclusion and recommendations for future work is provided in Chapter 5.

Chapter 2

Background Information

During recent years, the problem of developing fault detection and isolation (FDI) strategies for dynamical systems has been widely researched. A traditional approach in fault diagnosis is based on hardware redundancy that requires additional sensors or actuators to measure and control a specific variable. This method usually employs a voting technique to determine the health status of the system. Although the hardware redundancy method is very reliable and has been widely used in many systems, its main disadvantage is the need for multiple equipment and hardware that leads to extra maintenance cost and additional space to accommodate the redundant components [40].

Recently, much research has been performed on developing mathematical/analytical based approaches for fault detection and isolation in dynamical systems. These model-based approaches are mainly based on developing a mathematical model of the system. Constructing mathematical models for nonlinear and complex systems is quite time consuming and complex [27]. Due to limitations and difficulties of model-based FDI schemes [21], [41], [42] in this thesis an artificial neural network-based method is employed for fault detection and isolation purposes.

Specifically, during recent years a great deal of attention has been paid on developing dynamic neural networks, due to their capabilities in modeling and identification of nonlinear dynamical systems, control and filtering applications [39], [44], [45]. Dynamic neural networks can eliminate some of the shortcomings of static neural networks. The first drawback of static neural networks is that the information flows only in one direction. This implies that the information flows from the input neuron A to B, to C never comebacks to A in feedforward networks. On the other hand the structure of static neuron is mainly based on a simple summation operation and it is not dynamic in nature. Hence, it cannot provide a complete model for dynamic systems. Time delays are one of the inherent characteristics of biological neurons. This property is not taken into account in static neuron models.

In the structure of dynamic neural networks feedback is employed between the neurons of a layer, and/or between the layers of the network. The feedback paths from the outputs to the inputs, implies that the network has a local memory and its response is recursive. This implies that the network receives the inputs, calculates output and adjusts the weights, and then the output is recalculated. After successive iterations, the weight parameters are adjusted such that the error between the actual output and the network output becomes smaller and smaller. Different types of dynamic neural network approaches have been discussed in literature, including recurrent neural networks [46], [47], brain-state-in-a-box (BSB) neural model [46], [50], time-delay neural networks (TDNNs) [46], [48] and dynamic neural unit [49], [33].

The common feature of all types of dynamic neural networks is their capability of internally generating and embedding memory. This adds dynamic properties to the network, so that it will be responsive to time-varying signals. One way to introduce dynamic properties to a standard multilayer perceptron (MLP) network is by adding multiple recurrent connections with time delay units. An alternative approach is
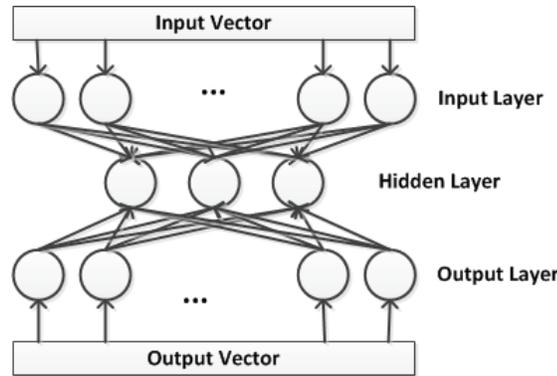
Figure 2.1: Multilayer perceptron architecture [86].

to add dynamic properties to a MLP network by embedding dynamic neurons that contain infinite impulse response (IIR) filters in the structure of a static feedforward MLP network.

2.1 The Architecture of the Multilayer Perceptron

A multilayer perceptron (MLP) neural network is a static neural network that receives the input data and maps the input data set into appropriate output data set [86]. The structure of a feed-forward multilayer perceptron network is depicted in Fig. 2.1.

2.1.1 The Generalized Delta Rule

The learning rule for the multilayer perceptron is known as "the generalized delta rule" or the "back-propagation rule". The generalized delta rule repetitively calculates an error function for each input and backpropagates the error from one layer to the previous one. The weights for a particular node are then adjusted in direct proportion to the error in the units to which it is connected.

Let

$$E_p = \text{error function for pattern } p \text{ ;}$$

$$t_{pj} = \text{target output for pattern } p \text{ on node } j \text{ ;}$$

$$o_{pj} = \text{actual output for pattern } p \text{ on node } j \text{ ;}$$

$$o_{ij} = \text{weight from node } i \text{ to node } j \text{ ;}$$

The error function E_p is defined to be proportional to the square of the difference $t_{pj} - o_{pj}$:

$$E_p = \frac{1}{2} \sum (t_{pj} - o_{pj})^2 \tag{2.1}$$

The activation of each unit j, for pattern p, can be written as:

$$net_{pj} = \sum w_{ij} o_{pi} \tag{2.2}$$

The output from each unit j is determined by the nonlinear transfer function f_j:

$$o_{pj} = f_j(net_{pj}) \tag{2.3}$$

We assume f_j is a sigmoid function:

$$f(net) = \frac{1}{1 + e^{-k.net}} \tag{2.4}$$

where k is a positive constant that controls the "spread" of the function. The delta rule implements weight changes that follow the path of a steepest descent on a surface in the weight space. The height of any point on this surface is equal to the error measure E_p. This can be shown by verifying that the derivative of the error function with respect to each weight is proportional to the weight change dictated by the delta rule, with a negative constant of proportionality, i.e.,

$$\Delta_p w_i = \propto -\frac{\partial E_p}{\partial w_{ij}} \qquad (2.5)$$

2.1.2 The Multilayer Perceptron Learning Algorithm Using The Generalized Delta Rule

In order to train a multilayer perceptron neural network, the following three steps must be followed:

- Initialize weights (to small random values) and transfer function.

- Present input.

- Adjust weights by starting from output layer and working backwards.

$$w_{ij}(t+1) = w_{ij}(t) + \eta \delta_{pj} o_{pi} \qquad (2.6)$$

where $w_{ij}(t)$ represents the weights from node i to node j at time t, η is a learning gain term, and δ_{pj} is an error term for pattern p on node j.

- For output layer units:

$$\delta_{pj} = k.o_{pj}(1 - o_{pj})(t_{pj} - o_{pj}) \qquad (2.7)$$

- For hidden layer units:

$$\delta_{pj} = k.o_{pj}(1 - o_{pj}) \sum (\delta_{pk} w_{jk}) \qquad (2.8)$$
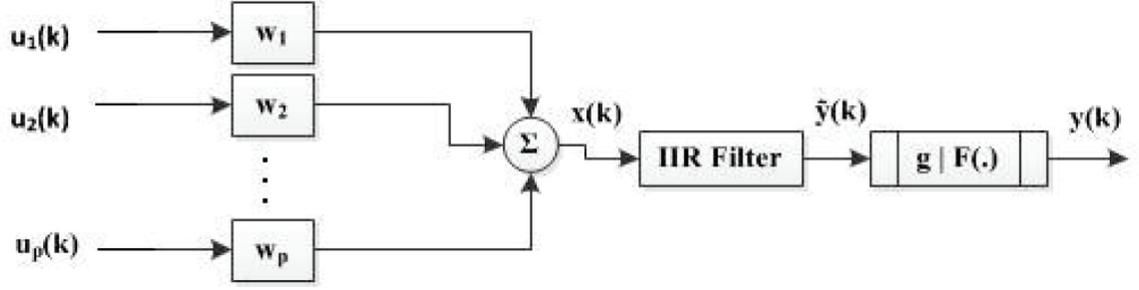
Figure 2.2: Structure of a dynamic neuron model with P inputs [53].

where the sum is over the k nodes in the following layer. The learning rule in a multilayer perceptron is not guaranteed to produce convergence, and it is possible for the network to fall into a situation (the so called local minima) in which it is unable to learn the correct output.

2.2 Dynamic Neuron Model

A Dynamic neuron is constructed by adding an Infinite Impulse Response (IIR) filter to a conventional of static neuron. The structure of an IIR filter is depicted in Fig. 2.3. By adding this IIR filter to the general structure of the static neuron, the neuron activity depends on its internal states and therefore, the neuron does indeed process past values of its own activity $y(k)$ and its inputs $u_p(k)$, for $p = 1, 2, \ldots P$; where P is the number of inputs and k is the discrete time samples. The structure of a dynamic neuron is depicted in Fig. 2.2. The dynamic neuron receives P inputs and in the first step, the weighted sum of the inputs is calculated according to equation 2.9 [53]:

$$x(k) = w^T u(k) = \sum_{p=1}^{P} w_p u_p(k) \tag{2.9}$$

where $w = [w_1, w_2 \ldots w_p]^T$ denotes the weight vector and $u = [u_1(k), u_2(k) \ldots u_p(k)]^T$

27
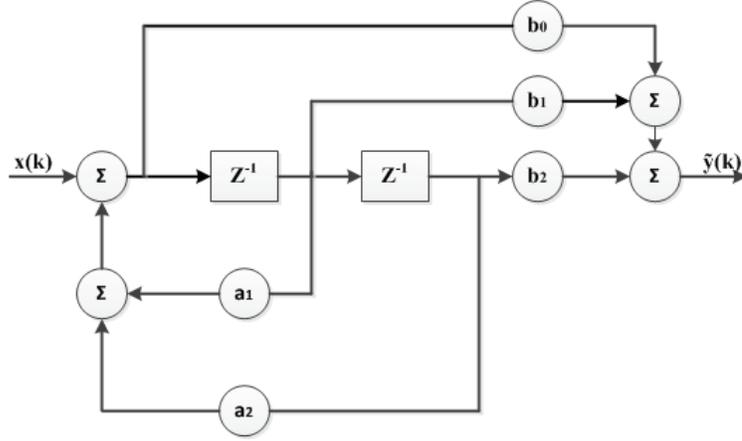
Figure 2.3: Structure of a second order IIR filter [34].

denotes the input vector.

In the next step, the calculated weighted sum of the inputs $x(k)$ is passed through the embedded IIR filter. The characteristics of the filter can be described by following expression:

$$\tilde{y}(k) = \sum_{i=1}^{n} b_i x(k-i) - \sum_{i=1}^{n} a_i \tilde{y}(k-i) \tag{2.10}$$

where n denotes the filter order, $a = [a_1, a_2 \ldots a_p]^T$ is the feedback weight vector, $b = [b_1, b_2 \ldots b_n]^T$ is feedforward weight vector, and $x(k)$ and $\tilde{y}(k)$ denote the input and output of the filter respectively. Finally, the neuron output is expressed as:

$$y(k) = F(g.\tilde{y}(k)) \tag{2.11}$$

where g is the slop parameter of the activation function and $F(.)$ is the nonlinear activation function. In this structure the slop parameter g has an adaptive nature thus the dynamic neuron can model the biological neuron better. In case of a nonlinear squashing activation functions i.e. hyperbolic tangent or sigmoidal, the undesirable saturation effect can be compensated by application of the slop parameter g [52].

2.2.1 Extended Dynamic Back-propagation Algorithm

Dynamic multilayer perceptron (DMLP) is obtained by embedding proposed dynamic neurons in feed-forward multilayer perceptron architecture. Since there are no recurrent links in dynamic multi-layer perceptron network, the DMLP can be trained based on the back-propagation rule. In an Extended Dynamic Back-Propagation (EDBP) algorithm [52], the calculated output of the network is propagated back to the network, through the hidden layers, containing dynamic neurons. This method can work in both on-line and off-line training modes [52].

Consider a dynamic neural network with M-layer of dynamic neurons described by the differentiable activation function $F(.)$. Fig. 2.4 shows the structure of an M-layered feedforward neural network. In this figure, S_m denotes the number of neurons in the m-th layer and u_s^m denotes the output of the s-th neuron of the m-th layer at discrete time k (m=1,2...,M,s=1,2...,S_m). The activity of the s-th neuron of the m-th layer is defined according to equation (2.12):

$$
\begin{aligned}
u_s^m(k) =& F(\tilde{y}_1(k)) = F(g_s^m.\tilde{y}(k)) = F(g_s^m(\sum_{i=1}^{n} b_i x(k-i) - \sum_{i=1}^{n} a_i \tilde{y}(k-i)) \\
=& F(g_s^m(\sum_{i=0}^{n} b_{is}^m x(k) \sum_{p=1}^{S_{m-1}} w_{sp}^m u_p^m(k-i) - \sum_{i=1}^{n} a_{is}^m \tilde{y}_s^m(k-i)))
\end{aligned}
\tag{2.12}
$$

The main objective of the learning process is to adjust the parameters of the network, based upon a given set of an input-output data. Starting from a small number of hidden layers and neurons, number of hidden layers can be increased until that a desired performance index (J) is satisfied:

$$
J = \frac{1}{2}\sum_{k=0}^{N} e(k)^2 = \frac{1}{2}\sum_{k=0}^{N} (y_d(k) - y(k))^2
\tag{2.13}
$$
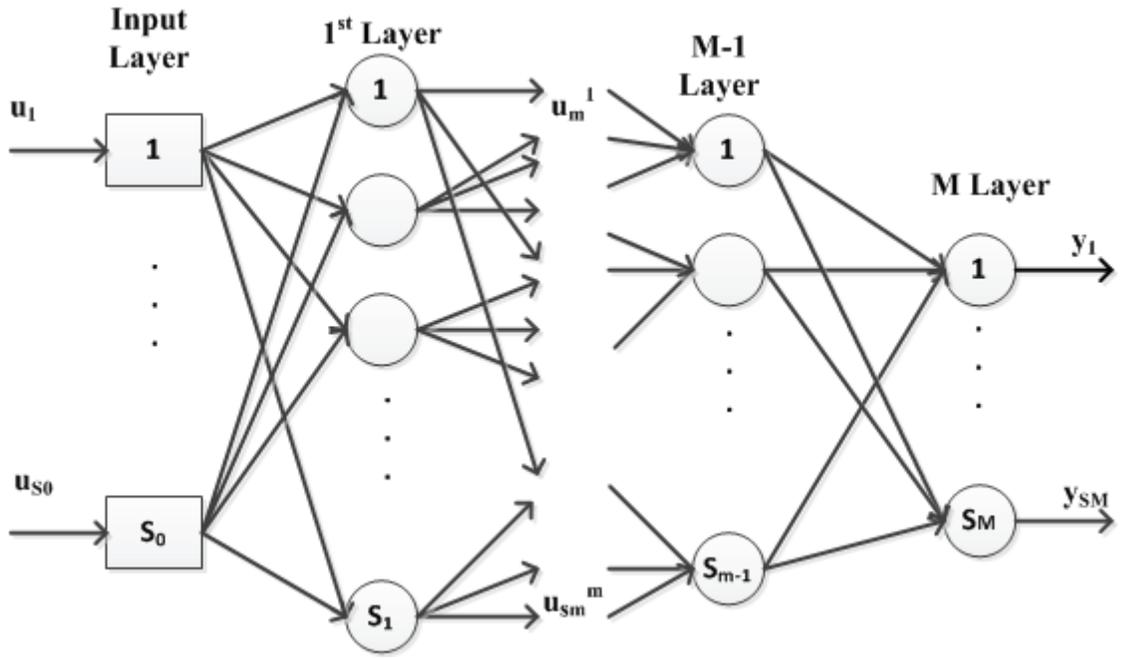
Figure 2.4: The M-Layered feedforward neural network [7].

Where $e(k)$ denotes the output error as a difference between the actual output of the system $(y(k))$ and the desired output of the system $y_d(k)$. The unknown network parameters that must be adjusted are:

- Weight matrix $[w_{sp}^m] : m = 1 \ldots M, s = 1 \ldots S_m, p = 1 \ldots S_{m-1}$.

- Filter feedback parameter matrix $[a_{is}^m] : m = 1 \ldots M, s = 1 \ldots S_m, i = 1 \ldots n$.

- Filter feedforward parameter matrix $[b_{is}^m] : m = 1 \ldots M, s = 1 \ldots S_m, i = 1 \ldots n$.

- Slope parameter matrix $[g_s^m] : m = 1 \ldots M, s = 1 \ldots S_m$.

According to the Extended Dynamic Back-Propagation (EDBP) algorithm, the parameters of the s-th neuron of the m-th layer are adjusted according to equation (2.14):

$$v_s^m(k+1) = v_s^m(k) + \eta \delta_s^m(k) S_{vs}^m(k) \tag{2.14}$$

30

where $v = [w, a, b, g]$ represents the parameter vector (i.e. weight vector, filter parameters or slop parameter), η is the learning rate, δ_s^m is the generalized output error and S_{vs}^m denotes the sensitivity function for the elements of the parameter vector v.

The generalized output error is described as follows [5]:

- Hidden layers generalized output error:

$$\delta_s^m(k) = \sum_{z=1}^{S_{m+1}} (\delta_s^{m+1}(k)g_z^{m+1}b_{0z}^{m+1}w_{zs}^{m+1})F'(\tilde{y}_{1s}^m(k)) \qquad (2.15)$$

- Output layer generalized output error:

$$\delta_s^M(k) = e_s(k)F'(\tilde{y}_{1s}^M(k)) \qquad (2.16)$$

The sensitivity function is defined as follows:

- Sensitivity with respect to the weight parameter w_{sp}^m:

$$S_{w_{ps}}^m = g_s^m(\sum_{i=0}^{n} b_{is}^m u_p^m(k-i) - \sum_{i=1}^{n} a_{is}^m S_{w_{ps}}^m(k-i)) \qquad (2.17)$$

- Sensitivity with respect to the feedback parameter a_{is}^m:

$$S_{a_{is}}^m(k) = -g_s^m \tilde{y}_s^m(k-i) \qquad (2.18)$$

- Sensitivity with respect to the feedforward parameter b_{is}^m:

$$S_{b_{is}}^m(k) = g_s^m x_s^m(k-i) \qquad (2.19)$$

31

- Sensitivity with respect to the slope parameter g_s^m:

$$S_{g_s}^m(k) = \tilde{y}_s^m(k) \tag{2.20}$$

Based on equations (2.14) to (2.20) the updating laws for the network parameters may be rewritten as follows:

- Hidden layers parameters:

  - Weight parameter w_{sp}^m:

$$
w_{sp}^m(k+1) = w_{sp}^m(k) + \eta \Big(\sum_{z=1}^{S_{m+1}} (\delta_s^{m+1}(k) g_z^{m+1} b_{0z}^{m+1} w_{zs}^{m+1}) F'(\tilde{y}_{1s}^m(k)) \Big)
$$
$$
g_s^m \Big(\sum_{i=0}^{n} b_{is}^m u_p^m(k-i) - \sum_{i=1}^{n} a_{is}^m S_{w_{ps}}^m(k-i) \Big) \tag{2.21}
$$

  - Filter feedback parameter a_{is}^m:

$$
a_s^m(k+1) = a_s^m(k) - \eta \Big(\sum_{z=1}^{S_{m+1}} (\delta_s^{m+1}(k) g_z^{m+1} b_{0z}^{m+1} w_{zs}^{m+1}) F'(\tilde{y}_{1s}^m(k)) \Big)
$$
$$
g_s^m \tilde{y}_s^m(k-i) \tag{2.22}
$$

  - Filter feedforward parameter b_{is}^m:

$$
b_s^m(k+1) = b_s^m(k) + \eta \Big(\sum_{z=1}^{S_{m+1}} (\delta_s^{m+1}(k) g_z^{m+1} b_{0z}^{m+1} w_{zs}^{m+1}) F'(\tilde{y}_{1s}^m(k)) \Big)
$$
$$
g_s^m x_s^m(k-i) \tag{2.23}
$$

– slope parameter g_s^m

$$g_s^m(k+1) = g_s^m(k) - \eta \left(\sum_{z=1}^{S_{m+1}} (\delta_s^{m+1}(k) g_z^{m+1} b_{0z}^{m+1} w_{zs}^{m+1}) F'(\tilde{y}_{1s}^m(k)) \right) \tag{2.24}$$
$$g_s^m \tilde{y}_s^m(k)$$

- Output layer parameters:

  – Weight parameter w_{sp}^m:

$$w_{sp}^m(k+1) = w_{sp}^m(k) + \eta(e_s(k) F'(\tilde{y}_{1s}^M(k))) g_s^m \left(\sum_{i=0}^{n} b_{is}^m u_p^m(k-i) \right.$$
$$\left. - \sum_{i=1}^{n} a_{is}^m S_{w_{ps}}^m(k-i) \right) \tag{2.25}$$

  – Filter feedback parameter a_{is}^m:

$$a_s^m(k+1) = a_s^m(k) - \eta(e_s(k) F'(\tilde{y}_{1s}^M(k))) g_s^m \tilde{y}_s^m(k-i) \tag{2.26}$$

  – Filter feedforward parameter b_{is}^m:

$$b_s^m(k+1) = b_s^m(k) + \eta(e_s(k) F'(\tilde{y}_{1s}^M(k))) g_s^m x_s^m(k-i) \tag{2.27}$$

  – Slope parameter g_s^m:

$$g_s^m(k+1) = g_s^m(k) + \eta(e_s(k) F'(\tilde{y}_{1s}^M(k))) \tilde{y}_s^m(k) \tag{2.28}$$

33

2.3 Spacecraft Attitude Representation

Representation of the orbital and translational motion of a rigid body in space depends on its reference coordinate system. Many different coordinate systems are used to analyze process and display data, because in various physical processes, calculations may be easier to perform or better understood in one coordinate system rather than another. In this thesis, four coordinate systems and two different attitude representation techniques that are mostly used in the field of aerospace attitude control are presented.

2.3.1 Coordinate Systems

Representation of position and orientation of a spacecraft depends on its reference coordinate system. In this section, three coordinate systems that are commonly used in the field of aerospace attitude control are introduced. Specifically,

- Earth Centered Inertial Frame (ECI). This is a non-accelerated reference frame in which Newton's laws are valid. The origin of this frame is located at the center of Earth. The z-axis is oriented toward the North Pole, the x-axis points towards to the first point of Aries. This axis is in the equatorial and ecliptic planes and the y-axis completes the right-handed orthogonal set. This coordinate system is shown in Fig. 2.5 [54].

- Earth Centered earth Fixed (ECF). This coordinate system has its origin in the center of the Earth. The x-axis points to Greenwich meridian and it is located in the equatorial plane. The z-axis coincides with the Earth's rotational axis and is positive towards to North Pole and the y-axis completes the right-handed orthogonal set. This coordinate system is shown in Fig. 2.6 [54].

- Satellite Body Fixed. In this coordinate system, the origin is located in the
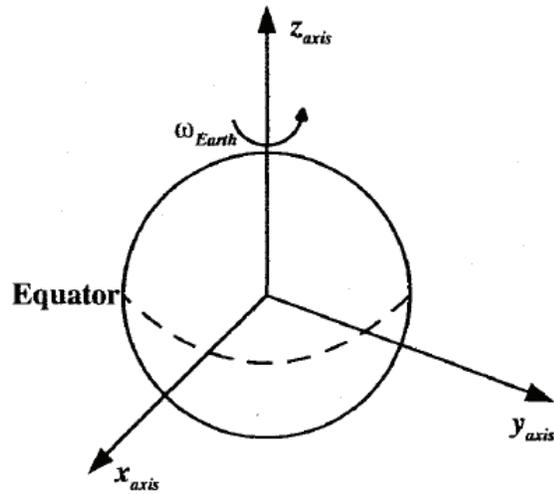
Figure 2.5: Earth centered inertial frame [153].
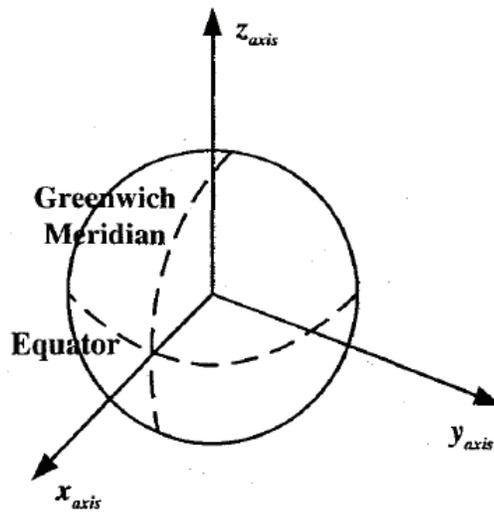
Figure 2.6: Earth centered Earth fixed frame [153].
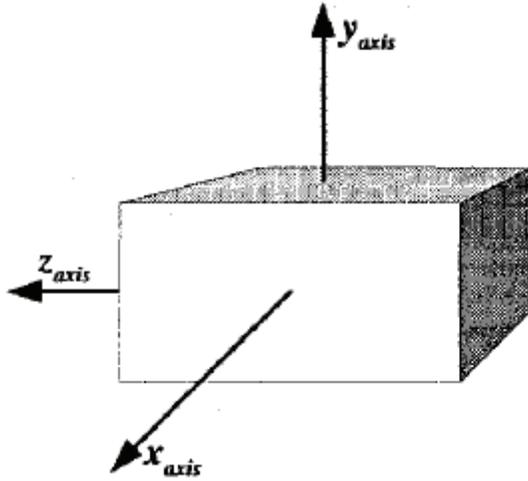
Figure 2.7: Satellite body fixed frame [153].

center of gravity (mass) of the satellite. The x-axis is parallel to the Orbiter structural body axis, the z-axis is parallel to the Orbiter plane of symmetry and perpendicular to the x-axis and y-axis completes the right-handed orthogonal set [54]. This coordinate system is shown in Fig. 2.7.

- Local Orbital Frame. In this coordinate system, the origin is located in the center of mass of the vehicle. The x-axis lies in the vertical orbital plane, perpendicular to the z-axis and it is positive in the direction of the motion of the vehicle. The z-axis lies along the geocentric radius vector to the vehicle and is positive towards the center of the Earth and y-axis completes the right-handed orthogonal set. Fig. 2.8 shows the local orbit reference frame.

2.3.2 Attitude Representation

The formulation of spacecraft attitude dynamics and control problems involves representation of the satellite kinematics. The orientation of a rigid body in space can be represented either by using Euler angles or the unit quaternions [55].

- Euler Angles In this scheme, the deviation angles with respect to a reference

36
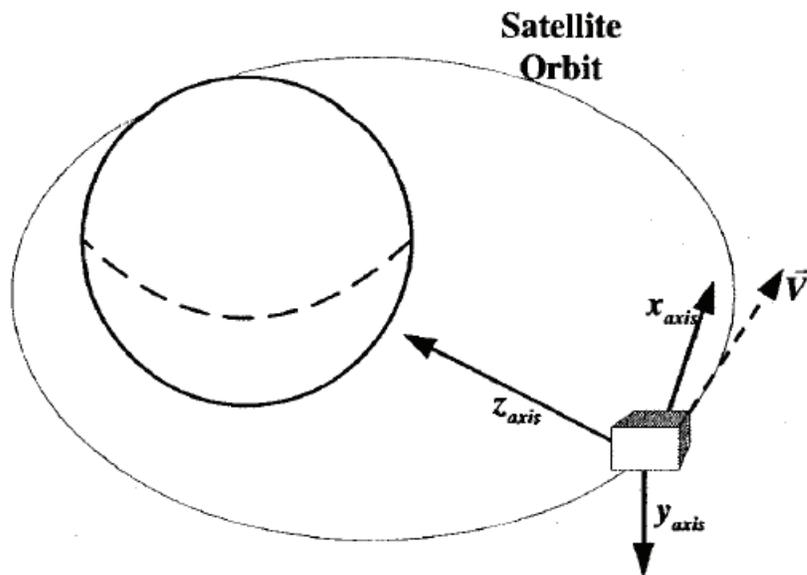
Figure 2.8: Local orbit frame [153].

frame are used to represent the attitude of the satellite. These deviation angles are given as roll angle φ, pitch angle θ, and yaw angle ψ, about the satellite body fixed coordinate system. One scheme for orienting a rigid body to a desired attitude is called a *body-axis rotation*. This representation involves successively rotating the rigid body about the axes of the rotated, body-fixed reference frame [56]. The most common sequence of rotation is defined by a first rotation about z-axis (yaw angle), a second rotation about y-axis (pitch angle) and a final rotation about x-axis (roll angle).

Consider three successive body-axis rotations that describe the orientation of a reference frame B relative to a reference frame A. Suppose that the following rotation sequence is considered:

$$C_3(\psi) : A' \leftarrow A \tag{2.29}$$

$$C_2(\theta) : A" \leftarrow A' \tag{2.30}$$

37

$$C_1(\varphi) : B \leftarrow A" \tag{2.31}$$

where each of these rotations is described as follows:

$$\begin{bmatrix} \vec{a_1}' \\ \vec{a_2}' \\ \vec{a_3}' \end{bmatrix} = \begin{bmatrix} cos\psi & sin\psi & 0 \\ -sin\psi & cos\psi & 0 \\ 0 & 0 & 1 \end{bmatrix} \begin{bmatrix} \vec{a_1} \\ \vec{a_2} \\ \vec{a_3} \end{bmatrix} = C_3(\psi) \begin{bmatrix} \vec{a_1} \\ \vec{a_2} \\ \vec{a_3} \end{bmatrix} \tag{2.32}$$

$$\begin{bmatrix} \vec{a_1}" \\ \vec{a_2}" \\ \vec{a_3}" \end{bmatrix} = \begin{bmatrix} cos\theta & 0 & -sin\theta \\ 0 & 1 & 0 \\ sin\theta & 0 & cos\theta \end{bmatrix} \begin{bmatrix} \vec{a_1}' \\ \vec{a_2}' \\ \vec{a_3}' \end{bmatrix} = C_2(\theta) \begin{bmatrix} \vec{a_1}' \\ \vec{a_2}' \\ \vec{a_3}' \end{bmatrix} \tag{2.33}$$

$$\begin{bmatrix} \vec{b_1} \\ \vec{b_2} \\ \vec{b_3} \end{bmatrix} = \begin{bmatrix} 1 & 0 & 0 \\ 0 & cos\varphi & sin\varphi \\ 0 & -sin\varphi & cos\varphi \end{bmatrix} \begin{bmatrix} \vec{a_1} \\ \vec{a_2} \\ \vec{a_3} \end{bmatrix} = C_1(\varphi) \begin{bmatrix} \vec{a_1}" \\ \vec{a_2}" \\ \vec{a_3}" \end{bmatrix} \tag{2.34}$$

In equations (2.29) and (2.31), A' and $A"$ are two intermediate reference frames. By combining the preceding equations of rotation, we obtain:

$$\begin{bmatrix} \vec{b_1} \\ \vec{b_2} \\ \vec{b_3} \end{bmatrix} = C_1(\varphi)C_2(\theta)C_3(\psi) \begin{bmatrix} \vec{a_1} \\ \vec{a_2} \\ \vec{a_3} \end{bmatrix} \tag{2.35}$$

These three angles θ, φ and ψ are called the Euler angles [56]. In order to avoid singularity that may occur in the Euler angles representation, another attitude representation, namely the quaternions representation, is introduced next [57].

- Euler Parameters or the Quaternions. The four Euler parameters are defined as follows:

$$q_1 = e_1 sin(\theta/2) \tag{2.36}$$

$$q_2 = e_2 sin(\theta/2) \tag{2.37}$$

$$q_3 = e_3 sin(\theta/2) \tag{2.38}$$

$$q_4 = cos(\theta/2) \tag{2.39}$$

$$e_1^2 + e_2^2 + e_3^2 = 1 \tag{2.40}$$

where θ represents the rotation angle and $\mathbf{e} = [e_1, e_2, e_3]^T$ represents the rotation axis. We define a vector $\mathbf{q} = [q_1, q_2, q_3]^T$ such that:

$$\mathbf{q} = \mathbf{e}sin(\theta/2) \tag{2.41}$$

$$\mathbf{q}^T\mathbf{q} + q_4^2 = q_1^2 + q_2^2 + q_3^2 + q_4^2 = 1 \tag{2.42}$$

The Euler parameters are also called quaternions [56]. Suppose that q^a and q^b represent attitude of satellite a and b in unit quaternions, respectively. By definition, the relative attitude of satellite a with respect to satellite b is [58]:

$$q^{a/b} = q^{a*}q^b \tag{2.43}$$

where q^{a*} is the conjugate of a unit quaternion q^a and according to the definition

39

[59]:

$$q^* = [-\hat{q}^T \ \bar{q}]^T \in \mathbb{R}^4 \tag{2.44}$$

The product of two quaternions is defined as:

$$qp = \begin{bmatrix} \bar{q}\hat{p} + \bar{p}\hat{q} + \hat{q} \times \hat{p} \\ \bar{q}\bar{p} - \hat{q}^T\hat{p} \end{bmatrix} \tag{2.45}$$

where for vectors $v = [v_1, v_2, v_3]^T$ and $w = [w_1, w_2, w_3]^T$, the cross product is defined as [59]:

$$v \times w = v^\times w \tag{2.46}$$

$$v^\times = \begin{bmatrix} 0 & -v_3 & v_2 \\ v_3 & 0 & -v_1 \\ -v_2 & v_1 & 0 \end{bmatrix} \tag{2.47}$$

2.4 Equations of Motion

The equations of motion that describe the rotational dynamics of a satellite can be described by a set of nonlinear dynamic and kinematic equations as follows.

- Attitude Dynamic Equations of a Satellite. In order to provide a modeling of the satellite dynamics, it is assumed that each spacecraft acts as a rigid body and as a point mass model for orbital dynamics. With these assumptions, according to the Newton-Euler's rotational equations of motion of a rigid body, the attitude

dynamics of the spacecraft becomes [60]:

$$\vec{T} = \dot{\vec{h}} + \vec{\omega} \times \vec{h} = I.\dot{\vec{\omega}} + \vec{\omega} \times (I.\vec{\omega}) \qquad (2.48)$$

$$\vec{T}^b = \vec{T}^b_{grav} + \vec{T}_{aero} + \vec{T}_{react} \qquad (2.49)$$

where I is the matrix of inertia, ω is the rotational rates of body frame, h is the angular momentum, T is the torques acting on the satellite in the body frame, $\vec{T}^b_{grav}$ is the gravitational torque working on the satellite body, $\vec{T}_{aero}$ is the aerodynamic torque and $\vec{T}_{react}$ is the reaction wheel torque.

A satellite orbiting the Earth is influenced by many perturbing forces, torques and disturbances and noise. Gravitational perturbation (J2) and gravitational torque highly affect a satellite in the lower altitudes due to the non-symmetric and non-homogenous characteristics of the Earth. The atmospheric drag is a dominating force at low altitudes whereas for high altitude orbits it may be ignored. Other major perturbing factors could be listed as solar radiation and solar wind, the magnetic field of the Earth, and the gravitational force of the Moon and the Sun [60].

- Attitude Kinematic Equations of a Satellite. The kinematic equations of the spacecraft are represented by using the quaternion attitude representation technique, namely:

$$\frac{d}{dt}\mathbf{q} = \frac{1}{2}[\Omega]\mathbf{q} \qquad (2.50)$$

41

where Ω is defined as:

$$\begin{bmatrix} \Omega \end{bmatrix} = \begin{bmatrix} 0 & \omega_z & -\omega_y & \omega_x \\ -\omega_z & 0 & \omega_x & \omega_y \\ \omega_y & -\omega_x & 0 & \omega_z \\ -\omega_x & -\omega_y & -\omega_z & 0 \end{bmatrix} \tag{2.51}$$

2.5 Formation Flying of Satellites

During the recent decade, spacecraft formation flying has become an exciting field of research. Spacecraft formation missions have several benefits over the single-satellite mission, namely:

- There is a lower launch risk if the system is distributed across several launch platforms.

- The greater range of structural configurability may offer a lower launch cost for a fleet of vehicles.

- Although the initial design cost for several spacecraft may be higher than a single spacecraft, the benefits of mass production can eventually result in lower per-vehicle cost.

- Using a group of spacecraft provides a level of redundancy in a high risk environment. If a fault occurs in one spacecraft in the formation, the mission will not be entirely compromised. In such a case the other spacecraft in the formation will be able to operate until the faulty spacecraft is replaced or repaired.

- The reconfigurability of the spacecraft in the formation is also beneficial for technology upgrades. This allows the new vehicles in the formation to be dynamically introduced to the system.

- The inherent redundancy in the formation flying system allows each individual spacecraft to be less robust- and thereby less expensive- with less risk to the mission.

Considering all these benefits, teams of space vehicles have been suggested for a variety of scientific and strategic space missions [61].

2.5.1 Formation Flying Control Architectures

Five formation control architectures are reported in the literature [1], namely Leader/Follower, virtual structure, Multi-Input/Multi-Output, Behavioral and Cyclic.

- Leader/Follower. In the leader/follower approach one spacecraft is designated as the leader and the rest of spacecraft in the formation are designated as the followers. In this architecture, the leader satellite tracks a prescribed state profile (i.e. attitude and position) and each spacecraft in the formation tracks the attitude and position of the leader spacecraft with a (possibly time varying) prescribed offset [62]. Numerous variations on the leader/follower architecture, including designating multiple leaders or forming a chain is studied in the literature [67]. Several leader/following approaches are discussed in [62], [64], [65], [66].

- Virtual Structure. In the virtual structure architecture the entire formation flying of spacecraft is treated as a single rigid body. In this scheme, the desired state profile of the virtual structure is defined and in the next step the motion dynamics of the virtual structure is translated into the desired motion of each single spacecraft in the formation and finally the tracking control laws for each spacecraft are derived. The application of virtual structure control architecture in multi-agent systems is studied in [68], [69], [70].

- Behavioral. In the behavioral approach several desired behaviors including collision avoidance, obstacle avoidance, goal seeking and formation keeping behaviors are prescribed to each agent and the control action of each agent is the weighted average of the control for each behavior. This formation flying control approach is reported in [71], [129], [72], [73], [74].

- Multi-Input/Multi-Output. In the Multi-Input/ Multi-Output approach, the entire formation flying dynamics is modeled as a multi-input/multi-output plant. In this approach, all the modern control techniques may be applied to control the formation. In [84], [85], [86] different multi input/multi-output formation control methods are studied.

- Cyclic. In the cyclic approach, the formation controller is designed by connecting individual spacecraft controllers. The cyclic formation flying control approach is similar to leader-follower control architecture; however in the cyclic approach the spacecraft controller connections are not hierarchical. This approach is studied in [75], [76], [77].

The main advantage of the virtual structure control approach is that it is easy to prescribe the behavior for the group of agents and the virtual structure can maintain a tight formation during the mission [31]. Motivated by advantages of this approach, a decentralized formation flying control scheme via the virtual structure is used in this thesis.

2.5.2 Dynamics of Earth Orbiting Formations

One of the problems in modeling of a formation flight is providing a dynamic model of multiple spacecraft in space. The three-body problem describes the motion of three point masses under their mutual gravitational interactions. From astronomical

point of view the moon's traveling around the Earth, or the motion of stars together with their planets in a specific constellation or even the Universe can be considered as an N-body problem. In order to simplify this problem, necessary steps are made according to the order of the magnitude of certain objects in the original dynamic motion equation. In a three-body system of the Earth, the Moon and the man-made spacecraft, the size of man-made spacecraft is obviously much smaller that the Earth and the Moon. The Hill problem [154] and the linearization model studying spacecraft rendezvous and docking with a short separation distance in between by the Clohessy and Wiltshire [83] has become the basis of formation flight dynamic equations. The Hill- Clohessy-Wiltshire (HCW) equations have high fidelity because the perturbations do not affect it so much and the relative motions and the time scales are small [3].

2.5.3 Formation Dynamics: Linearized Equations of Motion

The linearized equations of motion for a formation flying are given by:

$$\ddot{x}_i - 2\omega_0\dot{y}_i - 3\omega_0^2 x_i = \frac{Q_{x_i}}{m_i} \tag{2.52}$$

$$\ddot{y}_i + 2\omega_0\dot{x}_i = \frac{Q_{y_i}}{m_i} \tag{2.53}$$

$$\ddot{z}_i + \omega_0^2 z_i = \frac{Q_{z_i}}{m_i} \tag{2.54}$$

where in case of a circular reference orbit, the angular rate of the orbital frame (called the mean motion) is constant and satisfies the relationship:

$$\omega_0^2 = \frac{\mu}{R_0^3} \tag{2.55}$$

Further $\dot{R}_0 = \ddot{R}_0 = 0$ where R_0 is the radius of the earth-centered orbit and $\mu = 3.986 \times 10^5 [\frac{Km^3}{s^2}]$ denotes the gravitational parameter of the Earth. In equations (2.52) to (2.54) the parameters x_i, y_i and z_i represent the position of the i-th spacecraft in the rotating frame F_0 and Q_{xi}, Q_{yi} and Q_{zi} represent the generalized force vector components that also contain all disturbance forces acting on the formation. These equations are called the Hill-Clohessy-Wiltshire (HCW) equations [83].

2.5.4 Formation Flying Architecture and Controller Design

In this work the formation flying virtual structure architecture consists of four space-craft that are located on a plane. In this structure, instead of using a set of desired location and orientation for each spacecraft, we take advantage of virtual structure approach to define the desired pattern of the virtual structure.

The state of the virtual structure is defined by using a coordination vector as $\xi = [r_F{}^T, v_F{}^T, q_F{}^T, \omega_F{}^T, \lambda_F{}^T, \dot{\lambda}_F^T]^T$ where r_F, v_F, q_F and ω_F represent the position, velocity, attitude and angular velocity of the virtual structure with respect to the iner-tial frame and λ represents the expansion or contraction rate of the virtual structure. If each satellite has knowledge of the state of the formation, ξ and its own desired po-sition and orientation with respect to the virtual structure, then the formation flying control problem is transformed to the individual satellite control problem. Therefore the virtual structure state parameter, ξ is the minimum amount of information needed by each spacecraft in the formation to coordinate itself with the group. In this ap-proach, the desired formation pattern is defined by $\xi^d = [r_F^{d^T}, v_F^{d^T}, q_F^{d^T}, \omega_F^{d^T}, \lambda_F^{d^T}, \dot{\lambda}_F^{d^T}]^T$. This vector defines the desired states of the formation flying. In this work it is assumed that the formation is a piecewise rigid structure, implying that $v_F^d = \omega_F^d = \dot{\lambda}_F^d = 0$. In this approach the formation maneuver goal can be achieved through a set of forma-tion patterns [31]. In [31] the formation pattern is defined such that each spacecraft
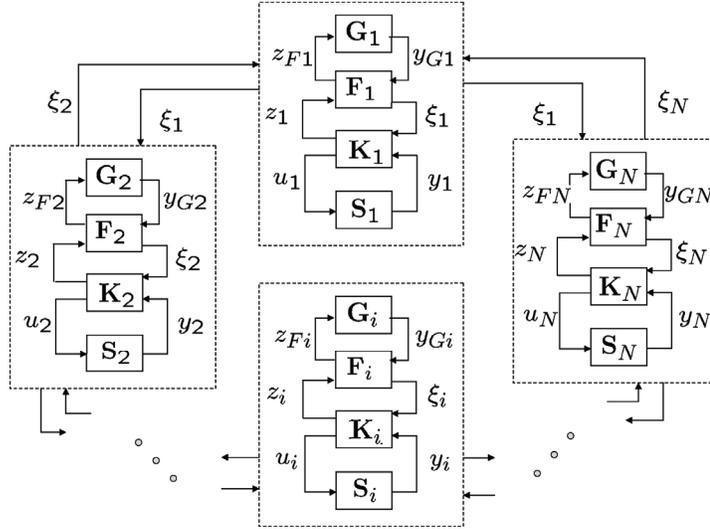
Figure 2.9: Decentralized control architecture via the virtual structure approach [31].

tracks a trajectory specified by the state of the virtual structure. In this approach the certain shape of the formation is preserved and collision avoidance is handled more efficiently.

Each spacecraft in the formation instantiates a local copy of the coordination vector. We represent the coordination vector instantiated in the i-th satellite with $\xi_i = [r_{Fi}^T, v_{Fi}^T, q_{Fi}^T, \omega_{Fi}^T, \lambda_{Fi}^T, \dot{\lambda}_{Fi}^T]^T$. The satellites in the formation communicate their instantiation of the coordination vector using a bidirectional ring topology. In this decentralized approach, instead of a discrete-event supervisor and formation control module at a centralized location, each spacecraft has a local copy of the discrete-event supervisor, G and the formation control module F, denoted by G_i and F_i for the i-th satellite, respectively. The structure of the decentralized controller architecture via the virtual structure is depicted in Fig. 2.9.

Before the group maneuver starts, a sequence of formation patterns is prescribed to each discrete-event supervisor G_i. The goal of G_i is the transition through a set of formation patterns so that the group maneuver goal can be accomplished sequentially. When the group maneuver starts, each discrete-event supervisor, G_i, outputs

the current formation pattern, y_{Gi} to the formation control module, F_i. The local formation control module instantiates a local copy of the coordination vector, ξ_i. The goal of F_i is to evolve the coordination vector ξ_i to the desired formation pattern ξ^d and synchronize ξ_i with the coordination vector instantiations in other spacecraft.

In [58], it is assumed that the spacecraft communicate the coordination vector instantiations using a bidirectional ring topology. That is, spacecraft $\#i$ sends its instantiation, ξ_i, to its two adjacent neighbors, spacecraft $\#(i+1)$ and $\#(i-1)$ and it receives the coordination vector instantiations of spacecraft $\#(i+1)$ and $\#(i-1)$. The formation control module, F_i, sends its coordination vector instantiation, ξ_i to the local spacecraft controller, K_i.

In the local spacecraft controller module, K_i, the desired states of the spacecraft $\#i$ is derived from equations (2.56) and (2.57) based on ξ_i:

$$[r_i^d]_0 = [r_F]_0 + C_{0F}\Lambda[r_{iF}^d]_F \tag{2.56}$$

$$[v_i^d]_0 = [v_F]_0 + C_{0F}\dot{\Lambda}[r_{iF}^d]_F + [\omega_F]_0 \times (C_{0F}\Lambda[r_{iF}^d]_F) \tag{2.57}$$

$$[q_i^d]_0 = [q_F]_0[q_{iF}^d]_F, \qquad [\omega_i^d]_0 = [\omega_F]_0 \tag{2.58}$$

where C_{0F} is the rotational matrix from the initial frame F_0 to the formation frame F_F. The reference frame F_F is fixed at the virtual center of the formation, that is, the virtual structure, as a formation frame and $\Lambda = diag(\lambda_F)$.

Unlike the desired states of the formation, $(r_{iF}^d, q_{iF}^d, q_{iF}^d, \omega_{iF}^d)$ relative to the formation frame, the desired states of each individual spacecraft in the formation $(r_i^d, v_i^d, q_i^d, \omega_i^d)$ relative to the initial frame are time varying and their evolution equations are given

by:

$$[\dot{r}_i^d]_0 = [v_i^d]_0 \tag{2.59}$$

$$[\dot{v}_i^d]_0 = [\dot{v}_F]_0 + 2[\omega_F]_0 \times (C_{0F}\dot{\Lambda}[r_{iF}^d]_F) + C_{0F}\ddot{\Lambda}[r_{iF}^d]_F + [\dot{\omega}_F]_0 \times (C_{0F}\Lambda[r_{iF}^d]) \tag{2.60}$$

$$[\dot{q}_i^d]_0 = [\dot{q}_F]_0[q_{iF}^d]_F, \qquad [\dot{\omega}_i^d]_0 = [\dot{\omega}_F]_0 \tag{2.61}$$

where the local controller K_i, is designed to guarantee that each spacecraft will track its desired states z_{Fi} and z_i indicate the formation and local controller feedback respectively [58].

2.5.5 Formation Control Strategies for Each Spacecraft

The desired states of each spacecraft in the formation must satisfy the translational and rotational dynamics of the spacecraft. The translational dynamics of each space-craft relative to F_0 are given by:

$$\frac{dr_i^d}{dt_0} = v_i^d, \qquad m_i\frac{dv_i^d}{dt_0} = f_i^d \tag{2.62}$$

where m_i and f_i are the mass and the control force of the i-th spacecraft, respectively. The rotational dynamics of each satellite relative to F_0 are given by:

$$\frac{d\hat{q}_i^d}{dt_0} = -\frac{1}{2}\omega_i^d \times \hat{q}_i^d + \frac{1}{2}\bar{q}_i^d\omega_i^d \tag{2.63}$$

$$\frac{d\bar{q}_i^d}{dt_0} = -\frac{1}{2}\omega_i^d.\hat{q}_i^d \tag{2.64}$$

$$J_i \frac{d\omega_i^d}{dt_0} = -\omega_i^d \times (J_i \omega_i^d) + \tau_i^d \tag{2.65}$$

The control force, f_i and the control torque, τ_i for the i-th spacecraft are given by:

$$f_i = m_i[\dot{v}_i^d - K_{ri}(r_i - r_i^d) - K_{vi}(v_i - v_i^d)] \tag{2.66}$$

$$\tau_i = J_i \dot{\omega}_i^d + \frac{1}{2}\omega_i \times J_i(\omega_i + \omega_i^d) - K_{qi}\widehat{q_i^{d*}q_i} - K_{wi}(\omega_i - \omega_i^d) \tag{2.67}$$

where J_i is the moment of inertia for the i-th spacecraft, K_{vi}, K_{ri} and K_{wi} are symmetric positive definite matrices, K_{qi} is a positive scalar, and $\hat{q}$ represents the vector part of the quaternion.

2.5.6 Formation Control Strategies for Each Virtual Structure Instantiation

In [58] a behavior-based approach is applied to synchronize the coordination vector instantiations during the maneuver as well as to evolve it to its desired goal at the end of the maneuver. The goal seeking error, E_G is defined as the total difference between the current instantiation ξ_i and the desired goal ξ^d:

$$E_G(t) = \sum_{i=1}^{N} ||\xi_i - \xi^d||^2 \tag{2.68}$$

The synchronization error, E_S is also defined as the total difference between neighboring instantiations:

$$E_S(t) = \sum_{i=1}^{N} ||\xi_i - \xi_{i+1}||^2 \tag{2.69}$$

Defining the total error as $E(t) = E_G(t) + E_S(t)$, the control objective is to drive $E(t)$ to zero asymptotically. In the virtual structure method, the coordination vector represents the states of the virtual structure and it is supposed that the i-th coordination vector satisfies the following rigid-body dynamics:

$$
\begin{bmatrix}
\dot{r}_{Fi} \\
m_F \dot{v}_{Fi} \\
\dot{q}_{Fi} \\
J_F \dot{\omega}_{Fi} \\
\dot{\lambda}_{Fi} \\
\ddot{\lambda}_{Fi}
\end{bmatrix}
=
\begin{bmatrix}
v_{Fi} \\
f_{Fi} \\
\frac{1}{2}\Omega(\omega_{Fi})q_{Fi} \\
-\omega_{Fi} \times J_F\omega_{Fi} + \tau_{Fi} \\
\dot{\lambda}_{Fi} \\
v_{Fi}
\end{bmatrix}
\tag{2.70}
$$

The proposed control force, f_{Fi} and the control torque, τ_{Fi} are given by:

$$
\begin{aligned}
f_{Fi} =& m_F\{-K_G(r_{Fi} - r_F^d) - \Gamma_{Gi}v_{Fi} - K_S[r_{Fi} - r_{F(i+1)}] - D_S[v_{Fi}- \\
& v_{F(i+1)}] - K_S[r_{Fi} - r_{F(i-1)}] - D_s[v_{Fi} - v_{F(i-1)}]\}
\end{aligned}
\tag{2.71}
$$

$$
\begin{aligned}
\tau_{Fi} =& - k_G\widehat{q_F^{d*}q_{Fi}} - \Gamma_{Gi}\omega_{Fi} - k_S\widehat{q_{F(i+1)}^*q_{Fi}} - D_S[\omega_{Fi} - \omega_{F(i+1)}] \\
& - k_S\widehat{q_{F(i-1)}^*q_{Fi}} - D_S[\omega_{Fi} - \omega_{F(i-1)}]
\end{aligned}
\tag{2.72}
$$

where Γ_{Gi} is the formation feedback term, and it is a positive definite matrix, m_F and J_F are the virtual mass and the virtual inertia of the virtual structure, K_G is a symmetric positive definite matrix, K_S and D_S are positive semidefinite matrices, and $\hat{q}$ represents the vector part of the quaternion.
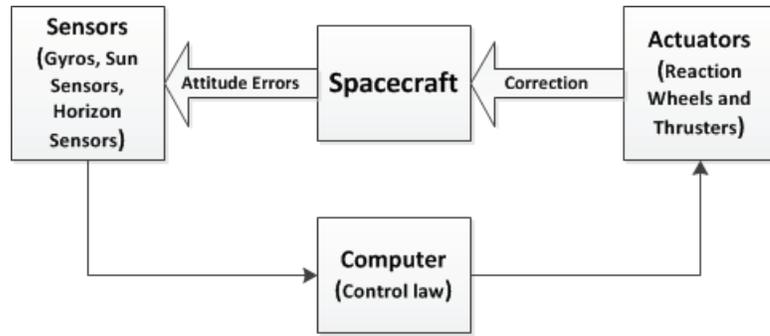
Figure 2.10: Attitude control operation [80].

2.6 Modeling of the Attitude Control Subsystem of a Spacecraft

The Attitude Control Subsystem (ACS) of a spacecraft deals with the orientation of the spacecraft with respect to one of the reference frames. The attitude control task requires sensors to measure the current attitude of the vehicle, actuators such as reaction wheels or thrusters to correct the attitude of the spacecraft and a control algorithm to determine the magnitude and direction of the torque in response to disturbances.

The block diagram of the attitude control operation of a spacecraft is depicted in Fig. 2.10. If the spacecraft drifts off from the desired attitude, the error is detected by sensors that are implemented in the spacecraft. The control law determines the response force or torque that is required to correct the attitude orientation and directs the proper actuator to correct it [80].

2.6.1 ACS Sensors and Actuators

Depending on the mission requirements and environmental situations the spacecraft must be equipped with specific sensors and actuators.

- Sensors. The sensors in the spacecraft determine the complete attitude information (i.e. angles and angular velocities) of a spacecraft with respect to a reference frame. Some of the commonly used sensors in the spacecraft systems are listed below:

  - **Sun sensors**: When the sun sensors are illuminated by sun radiation, the specific material in them produces an output current signal. Measuring this electric signal, the Sun incidence angle with the surface illuminated can be determined. These sensors have been designed with different accuracies and normally the sun sensors can be calibrated based on the mission requirements. In addition to attitude determination purpose, the sun sensors can be used for instrument pointing, solar panel pointing and thermal requirement verification [81].

  - **Horizon sensor (Earth sensor)**: When the spacecraft is rotating close to a planet, in order to determine the satellite attitude, the precise position of the center of the planet has to be evaluated. These sensors work based on analyzing the area in Field of View (FOV) of a satellite that are not illuminated (deep space), compared to the illuminated area (planet). In general, in order to reduce the effects of interference, the infrared sensors are designed for which the ratio of the Earth radiation to the Sun radiation is "1 to 400" [81]. The accuracy level of the Earth sensor is almost in the same level as that of the Sun sensor.

  - **Magnetic field sensor**: In order to provide attitude information, this sensor measures the magnetic field vector. The measurement of this sensor must be coupled with mathematical model of the magnetic field and the position of the satellite. It is not simple to measure a constant magnetic field and there is always uncertainty in the direction and the amount of

the magnetic field that is determined by these sensors. That is the reason why the magnetometers must always be coupled with other measurements to provide reliable attitude determination [81].

– **Star sensor**: This sensor determines the attitude of the vehicle based on the position of the stars in the space. The maximum attitude determination accuracy that is attainable using the sun sensors is $\frac{1}{8}$ of a degree. If the orbit has a phase in the eclipse, sun is not always visible and sun sensors cannot be used for attitude determination. Using the star sensors the accuracy of the attitude determination is improved and by selecting the appropriate star to observe, no eclipse problem arises. Due to these advantages, sun sensors are more expensive in terms of construction and operation on board of a satellite.

– **Gyroscopes**: The gyroscopes are used to measure the angular velocity of the spacecraft. They provide information on the rotational rates of the spacecraft in the inertial frame.

• Actuators. The main responsibility of actuators in a spacecraft is generating torques or forces that are required to change the orientation or position of the spacecraft. Some of the most known actuators in spacecraft attitude stabilization is presented below:

– **Reaction Wheel**: Reaction wheels work based on acceleration and deceleration of spinning rotors. The actuators which are responsible for satellite attitude control are three reaction wheels on three axes of each satellite. Their main functionality is to provide reaction torque for a spacecraft and store angular momentum [82]. The advantage of using reaction wheels as

actuators in attitude control subsystem of a satellite over other types of actuators (like magnetic actuators) is that their capability of controlling the satellite is independent from their geographical location and altitude [82]. The disadvantage is mainly in moving parts, the weight and the expense. In general, a reaction wheel structure consists of a rotating flywheel that is driven by an internal brushless DC motor [82].

– **Magnetotorquer**: Magnetic actuators produce a torque by inducing a magnetic dipole in a coil that is surrounded by the magnetic field of Earth. Due to the variation in the Earth's magnetic field, the effectiveness of these actuators depends on their height from the Earth. As the spacecraft moves in its orbit, the direction of the magnetic field changes and the attitude control system gains controllability about the three axes. Magnetotorquers can normally provide torques in the range of 10^{-3} to $10^{-6}Nm$.

– **Thrusters**: The simplest way to create torques is to create a set of forces with directions not aligned with the center of mass, and this can be obtained by mass explosion techniques. In thrusters, acceleration of a propellant is used to generate a force in the direction of which the propellant is discharged. Due to ignition transient, jet thrusters are not used for precise attitude control. The torque needed in control purposes is in the order of milli-Newton-meters, but the force generated in chemical thrusters is in the order of at least one Newton. In order to make it compatible with attitude control, they are switched on and off with a given modulation, but this even increases the problem due to ignition transients and mechanical problems in the thruster. Using chemical thrusters it is not possible to control the magnitude of the force. These problems can be solved by using electric thrusters. Electric thrusters can be easily modulated in amplitude,
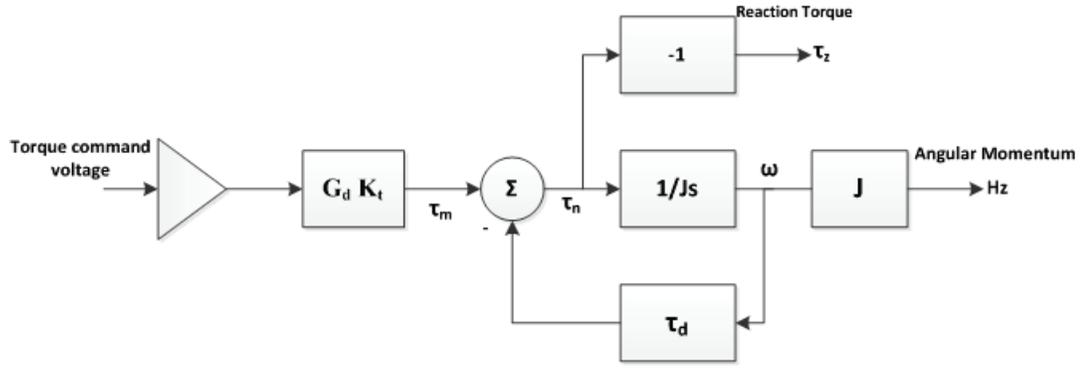
Figure 2.11: Ideal reaction wheel model.

they have reduced propellant consumption and they are well suited for fine attitude control. Due to the large power consumption of electric thrusters, these actuators are always coupled with large solar panels [81].

2.7 Mathematical Model of Nearly Ideal Reaction Wheel

The fundamental block diagram of a nearly ideal reaction wheel is depicted in Fig. 2.11. An ideal reaction wheel does not have any friction torque, and the only loss that is subtracted from the motor torque is the friction torque. In this block diagram, the torque command voltage is the only input which controls the motor current and the motor torque. The angular momentum stored in the flywheel, H_z is calculated from the equation (2.73):

$$\vec{H}_z = J\vec{\omega} \tag{2.73}$$

According to the Newton's third law, the reaction torque applied to the spacecraft is the opposite of the net torque on the flywheel. The reaction torque, τ_z, can be

56

derived according to the Newton's second law and is given by:

$$\tau_z = -\tau_n = \frac{-\partial H}{\partial t} = \frac{\partial(J\omega)}{\partial t} = -J\frac{d\omega}{dt} \tag{2.74}$$

The net torque is the motor torque, τ_m, less any frictional losses, τ_d or :

$$\tau_n = \tau_m - \tau_d \tag{2.75}$$

2.7.1 Mathematical Model of High Fidelity Reaction Wheel

In general, reaction wheel structure consists of a rotating flywheel that is driven by an internal brushless DC motor. A detailed block diagram of a high fidelity reaction wheel is depicted in Fig. 2.12. This model consists of five main sub-blocks: (1) motor torque control, (2) speed limiter, (3) EMF torque limiting, (4) motor disturbances, and (5) bearing friction and disturbances. Table 2.1 provides the typical parameters for the ITHACO's standard type A reaction wheel [84].

2.7.2 Reaction Wheel Dynamics

The fundamental relationships for a high fidelity mathematical model of a reaction wheel system are provided in the section below.

- Motor Torque Control: The motor driver is basically a voltage controlled current source with a gain, G_d. The motor current is proportional to the torque command voltage. The motor torque control block generates a motor current that is proportional to the torque command voltage and converts this current into torque through the motor current constant, K_t according to equation (2.76):

$$K_t = \frac{\tau_m}{I_m} \tag{2.76}$$

57
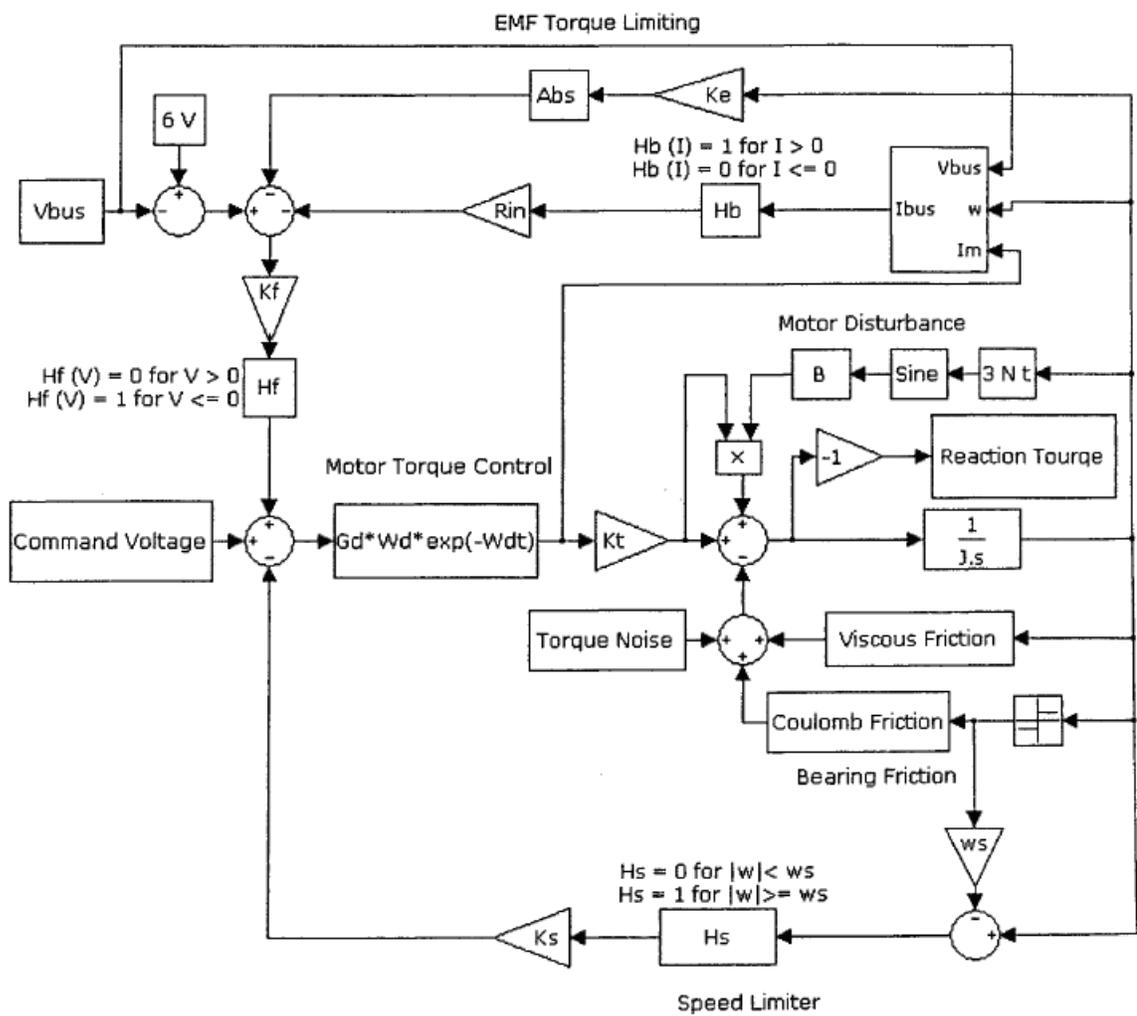
Figure 2.12: Detailed high fidelity reaction wheel block diagram [84].

Table 2.1: Typical values of type A reaction wheel [84].

Variable	Nomenclature	Unit	Value
J	Flywheel inertia	$N.m.s^2$	0.0077
G_d	Driver gain	A/V	0.190
K_t	Motor torque constant	$N.m/A$	0.029
K_e	Motor back-EMF constant	$V/rad/s$	0.029
K_s	Over-speed circuit gain	$V/rad/s$	95
ω_s	Over-speed circuit threshold	rad/s	690
τ_c	Coulomb friction	$N.m$	0.002
N	Number of motor poles	-	36
B	Motor torque ripple coefficient	-	0.22
R_{in}	Input resistance	Ω	2.00
	Torue command range	V	± 5
K_f	Voltage feedback gain	V/V	0.50
P_q	Quiescent power	W	3.00
ω_a	Torque noise high pass filter frequency	rad/sec	0.20
θ_a	Torque noise angle deviation	rad	0.05
R_b	Bridge resistance	Ω	2.00

- EMF Torque Limiting: In low bus voltage conditions, due to the increasing back-EMF, K_e of the motor, the motor torque may be limited at high speeds. Once the back-EMF increases to the motor driver's saturation point, this may result in eliminated voltage headroom and reduced torque capacity. The back-EMF limiting is coupled to power consumption based on equation (2.77):

$$P_{INPUT} = \frac{V_{BUS}}{V_{BUS} - 1}[\frac{\tau_m^2}{k_t^2}R_B + \frac{0.04|\tau_m|V_{BUS}}{k_t} + P_q + \omega\tau_m\frac{k_e}{k_t}] \qquad (2.77)$$

If we substitute the equation (2.76) into equation (2.77) it yields:

$$I_{BUS} = (\frac{1}{V_{BUS} - 1})(I_m^2 R_B + 0.04|I_m|V_{BUS} + P_q + \omega I_m k_e) \qquad (2.78)$$

In the schematic model of a high fidelity reaction wheel, a heavyside function H_b is included in the block diagram. The main responsibility of this function is to eliminate the voltage drop when the power is not being drawn from the

bus [84].

- Speed Limiter: The main responsibility of speed limiter circuit is to prevent the flywheel from reaching unsafe speeds. Once the speed of the wheel exceeds the established threshold, ω_s, speed limiter circuit measures the wheel speed with an analog tachometer circuit and provides it as a high-gain negative feedback, k_s, into the torque command. A heavyside function H_s is included in the block diagram of the speed limiter that enables the negative feedback by comparing the wheel speed with the threshold, ω_s [84].

- Motor Disturbances: Due to the motor excitation and the magnetic construction, the torque motor in the reaction wheel can be a source of high frequency disturbances. In the most current reaction wheels, brushless DC motors are employed. These motors generate torque ripple disturbances at the communication frequency and cogging at a frequency corresponding to the number of motor poles and rate of rotation. Torque ripple is the amount of variation in motor torque, depending on the communication method and the back-EMF shape. Codding is a type of disturbance that is always present in conventional brushless DC motors that may lead to undesirable behavior specially when operating near zero speed. Cogging is due to the change in reluctance of the iron stator as the magnets in DC motor are rotated [84].

- Bearing Friction and Disturbances: The drag friction in the reaction wheels of a satellite generally can be broken into two components, including the viscous friction, τ_v and the coulomb friction, τ_c. The viscous friction in the bearings is due to the bearing lubricant and it varies with speed and temperature. The viscous drag friction has been characterized for the ITHACO's Type A and B

reaction wheels to be given by:

$$\tau_v = (0.049 - \frac{0.0002}{°C}(T + 30°C))\frac{mN - m}{rad/sec} \qquad (2.79)$$

The coulomb friction, τ_c, is independent of the temperature or speed of the wheel and it is mainly caused by rolling friction and its polarity depends on the direction of rotation of the wheel [84].

- Torque Noise: Torque noise is the very low frequency torque variation of the bearings and it is a function of lubricant dynamics. This noise is present in typical band-width of the spacecraft controllers and it has the most significant effect on spacecraft pointing. Torque noise is specified as the deviation from the ideal location of the rotor at any constant speed. This specification can be translated into a torque disturbance by the following equation:

$$\tau_a = J\theta_a\omega_a^2 sin\omega_a t \qquad (2.80)$$

2.8   Reaction Wheel Fault Types

In general, there are three types of faults that occur in reaction wheels of a satellite and may result in serious damage or catastrophic failures:

- **Bus Voltage Fault**: The bus voltage must be high enough to avoid elimination of the voltage headroom. When the bus voltage drops down, the motor torque may be limited due to the increasing amount of back-EMF of the motor and it will lead to reduced torque capacity of the wheel and instability in the attitude of the satellite. For very low values of bus voltage, the entire attitude control system will break down and the attitude of the satellite will be out of control.

61

- **Motor Current Fault**: Motor torque is directly related to the motor current through a constant parameter k_t. When the motor current drops from its nominal value, the corresponding motor torque will drop down accordingly. When the current loss becomes serious, the reaction wheel cannot provide enough reaction torque and the attitude control loop of the satellite tends to become unstable.

- **Temperature Fault**: The viscous friction in a satellite's reaction wheel is the main friction factor and is highly related to the temperature. When the temperature becomes too high, this implies that the bearings have been damaged and this results in increased viscous friction. The temperature fault may lead the satellite into abnormal operating condition.

2.9   Conclusion

In this chapter the structure of static and dynamic neural networks that will be used for FDI purposes in the next chapters is presented in detail. In this thesis, a Dynamic Multilayer Perceptron (DMLP) network will be utilized as a fault detection tool and a static multi layer perceptron network is applied as a fault type recognition tool. in the next section. A review on the attitude control subsystem (ACS) of a satellite was also provided and various attitude representations and coordinate systems are explained.

A list of actuators and sensors has also been provided in detail. The concept of fomration flying system and five different control approaches for formation flight control are introduced. The decentralized control architecture via the virtual structure that will be used in the following chapters of this thesis to simulate attitude maneuvers under healthy and faulty actuator situations is also described in this chapter.

Chapter 3

Actuator Fault Detection for Formation Flight of Satellites

In order to develop a fault detection (FD) system that has the capability of detecting and isolating low severity faults, a decentralized dynamic neural network-based approach is proposed in this chapter. Details on the structure of the dynamic neural structure, the neuron's dynamic model and the extended dynamic back-propagation (EDBP) training algorithm have already been provided in chapter 2.

3.1   Fault Detection for a Single Spacecraft

In [43] the dynamic neural network (DNN) that was introduced in Section 2.2 is applied for detecting and isolating faults on a three-axis ACS model. The components of the developed neural fault detection scheme are depicted in Fig. 3.1. This DNN is specially developed for fault detection purposes in the attitude control subsystem of a satellite. where $V_{torquecommand}$ and $\tau_{reaction}^{estimated}$ represent the normalized command voltage and estimated reaction torque, respectively and $\tau_{reaction}^{actual}$ represents the normalized desired value of the output reaction torque. The proposed DNN needs only
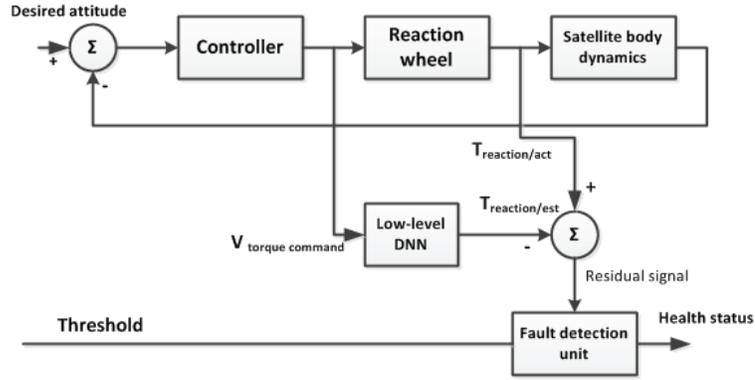
Figure 3.1: Neural network based FD system of a single satellite.

one input in order to construct a suitable identification model and produce an output.

3.1.1 Training Phase

In this thesis, the modeled ACS actuator, that is the reaction wheel, has one input (torque command voltage) and one output (reaction torque) along each satellite axis. These input/output data pairs are collected under healthy operating condition of the spacecraft and are used for training purposes. Preprocessing steps are performed on the input/output data pairs so that all the data used for DNN training are normalized in the range of [-1, +1]. The training process is then carried out based on an extended dynamic back-propagation algorithm for each axis.

The network parameters are initialized with small random values and the IIR filter's denominator coefficients are initialized to zeros. The structure of the dynamic neural network contains one hidden layer of hyperbolic tangent activation functions and one output layer of linear activation functions. The neurons embedded in the structure of the dynamic neural network have second order IIR filters. The training process is started from a relatively small network structure and the optimum structure is obtained by incrementally increasing the number of hidden neurons until required performance specifications are met. The training phase is conducted for each DNN

that is employed along each axis of the satellite. The best results are obtained using a N_{1-8-1} structure, which implies that there is one neuron in the input layer, 8 neurons in the hidden layer and one neuron in the output layer. The learning rate parameter is set to 0.01. The training process is accomplished by using Monte Carlo's simulations under different noisy conditions for 50000 steps and each step is 0.001 sec. The networks are trained for 100 different pairs of input/output data in presence of a normally distributed noise with zero mean and standard deviation of 0.01 differences between the maximum and the minimum values in the input/output data intervals. The average value of the mean square error in the 100 training iterations is 0.0141 and its standard deviation is 0.0002, which is quite acceptable. The performance of the networks during the training phase for 3 axis of satellite #1 is depicted in Fig. 3.2.

3.1.2 Testing Phase

The representation capability of the trained DNNs is evaluated in the testing phase. In the testing phase another input/output data set is used to evaluate the capabilities of the trained DNNs to model the reaction wheel system. The testing step is accomplished for 100 different pairs of input/output data in presence of a normally distributed noise with zero mean and standard deviation of 0.01 differences between the maximum and the minimum values in the input/output data intervals. The average value of the mean square error in the 100 testing samples is 0.16 and its standard deviation is 0.02, which is quite acceptable. Fig. 3.3 shows the output of the actual and the neural model in the testing phase in the three axes of the satellite #1. The results indicate that the trained DNNs have the ability to represent dynamic model of the reaction wheels, and therefore they can detect malfunctions that could occur in actuators of the spacecraft system. the testing phase for the other axes of the satellite
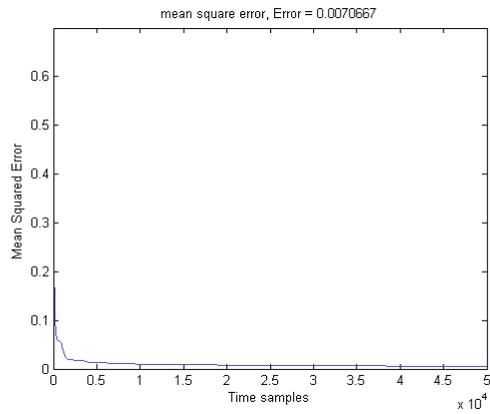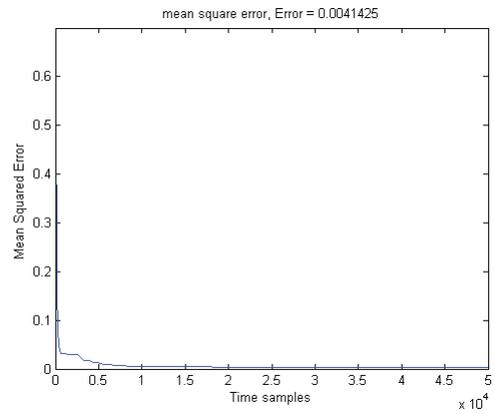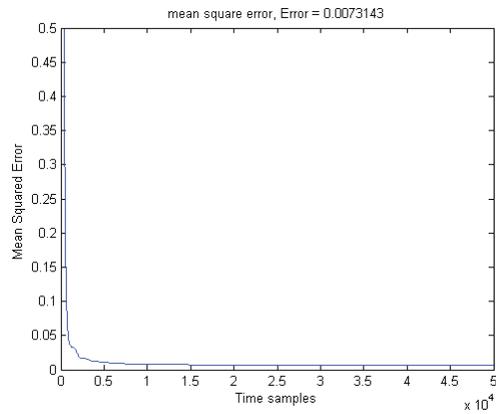
Figure 3.2: The performance index (mean squared error of the output reaction torque) curve for the dynamic neural network- satellite #1 (a) x-axis, (b) y-axis (c) z-axis.

can be accomplished in a similar way.

3.1.3 Reaction Wheel Fault Detection Strategy

The trained dynamic neural networks are to be used to detect reaction wheel faults in the satellite. After training and testing the proposed DNNs, they will be used to generate residual signals. The difference between the actual output of the reaction wheel that is measured by using the torque sensors in the satellites and the estimated output that is obtained from the DNN is called residual signal. This signal is used for health status determination of actuators in the satellites.

The general fault detection scheme is depicted in Fig. 3.1. In this thesis a simple threshold technique is used for each axis. In this method, a lower and upper threshold bounds are determined for each axis of a satellite and any deviation from this range is considered as a fault. In order to determine the threshold boundaries, first the residual signals that are generated during various healthy operating conditions are analyzed. The mean value $(\bar{X})$ and the standard deviation (σ) of these signals are calculated, and the threshold value is then calculated by using the following formula:

$$t.h = \bar{X} \pm 3\sigma \qquad (3.1)$$

3.2 Actuator Fault Scenarios

3.2.1 Single Fault Scenarios

In order to investigate fault detection capabilities of the constructed residual generators, different faulty cases under various noisy situations are considered. Specifically,

- Bus voltage (V_{BUS}) Fault. In the low bus voltage conditions, the motor torque may be limited at high speeds due to the increasing back-EMF (k_e) of the motor
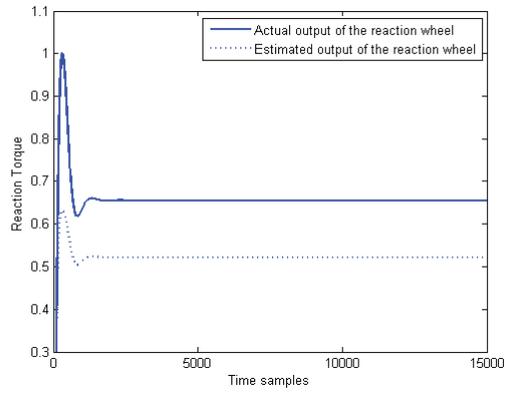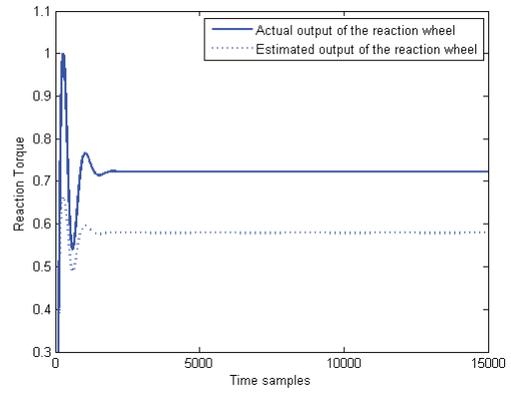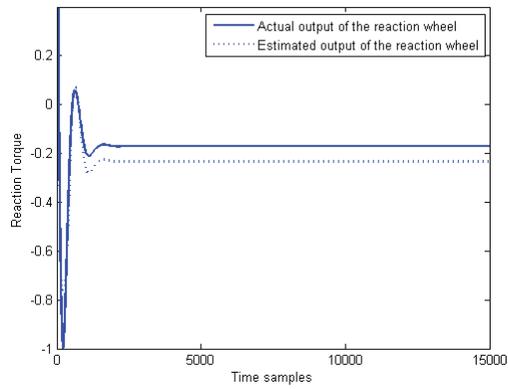
Figure 3.3: Testing curve (actual and estimated outputs) for the DNN - (a) x-axis, (b) y-axis, and (c) z-axis of the satellite #1.

[49]. In this thesis, three different bus voltage fault scenarios are considered and the fault indicator signals that are produced in residual generators are shown in Figs. 3.4- 3.6. The fault diagnosis is carried out in the steady state response of the satellite so that if the monitored output (i.e. reaction torque) exceeds the predefined threshold value it can be detected as a fault.

- First scenario: In this case, a low bus voltage (80% drop in nominal value) fault is injected in the x-axis of the satellite at the time sample of 5000. Fig. 3.4 shows the residual signal that is generated along the x-axis of the satellite. This figure clearly shows that the proposed dynamic neural network along the x-axis is capable of detecting the fault successfully.

- Second scenario: In this case, a low bus voltage (60% drop in nominal value) fault is injected in the y-axis of the satellite at the time sample of 5000. Fig. 3.5 shows the residual signal that is generated along the y-axis of the satellite. This figure shows that the proposed dynamic neural network along y-axis has the ability of detecting the fault successfully.

- Third scenario: In this case, a low bus voltage (50% drop in nominal value) fault is injected in the z-axis of the satellite at the time sample of 5000. Fig. 3.6 shows the residual signal that is generated along the z-axis of the satellite. This figure clearly shows that the proposed dynamic neural network along the z-axis of the satellite is capable of detecting the fault successfully.

- Motor current (I_m) fault. As given in equation (2.76), the motor torque in a reaction wheel is proportional to the motor current through the motor torque constant, k_t. Therefore, when a fault occurs in the motor driver gain, it influences the motor current directly and eventually its effects will be reflected in

69
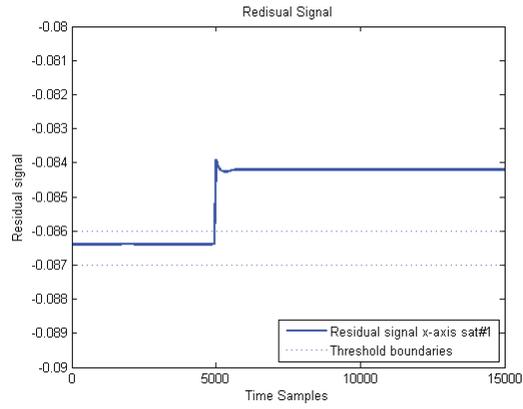
(a)
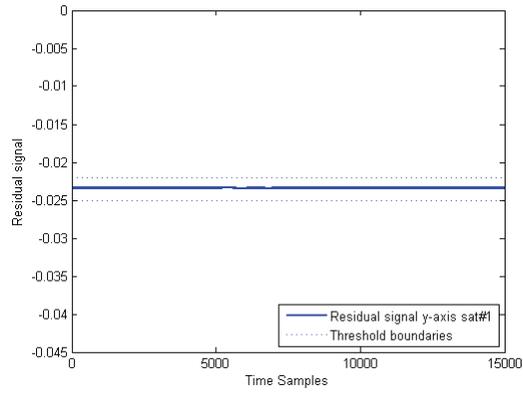
(b)
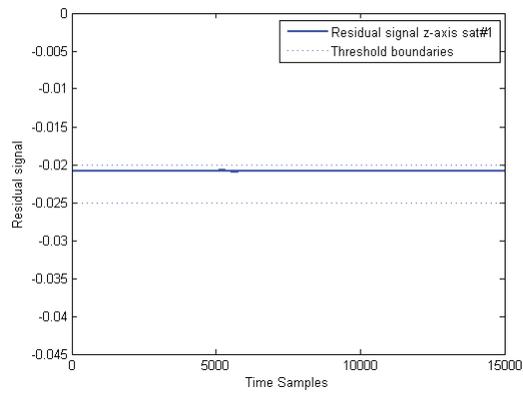
(c)

Figure 3.4: Residual error signals in case of a bus voltage fault: (a) x-axis, (b) y-axis, and (c) z-axis - Scenario 1.
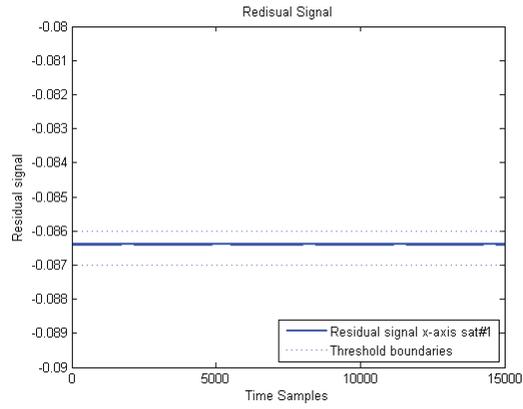
(a)
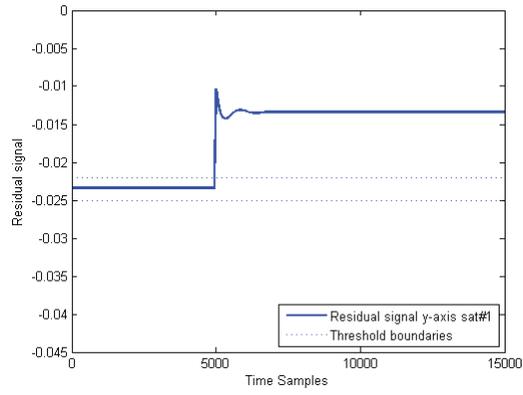
(b)
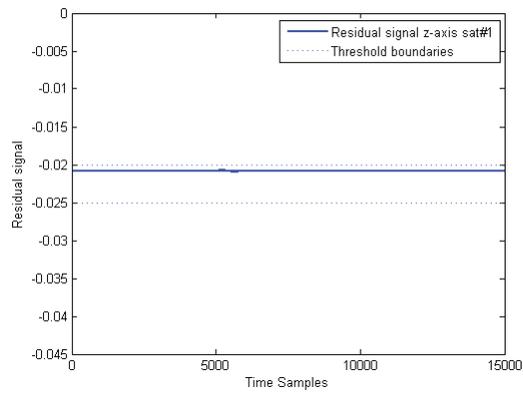
(c)

Figure 3.5: Residual error signals in case of a bus voltage fault: (a) x-axis, (b) y-axis, and (c) z-axis - Scenario 2.
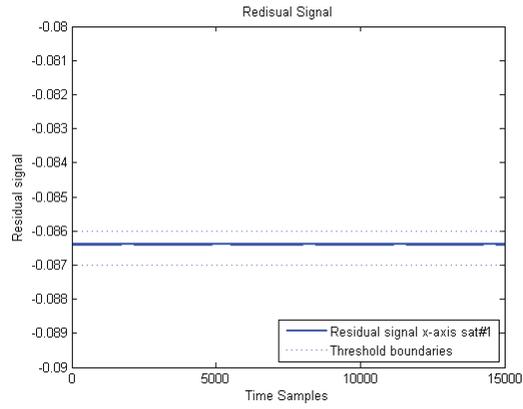
(a)
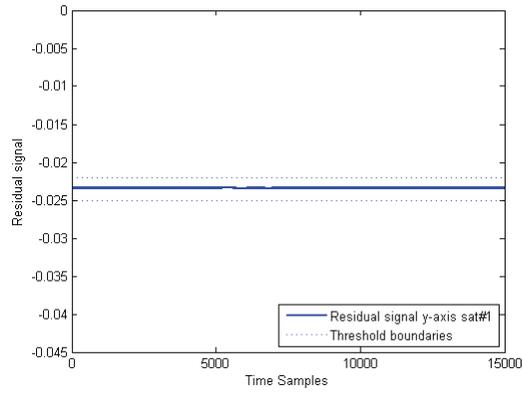
(b)
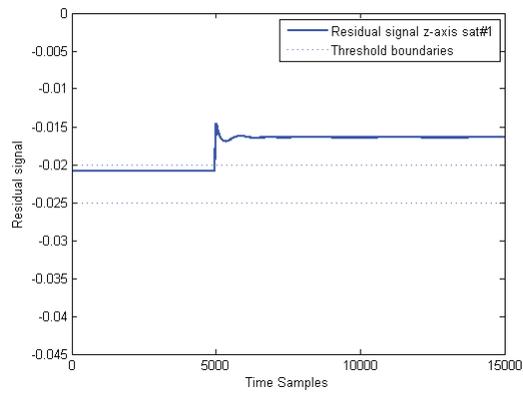
(c)

Figure 3.6: Residual error signals in case of a bus voltage fault: (a) x-axis, (b) y-axis, and (c) z-axis - Scenario 3.

72

the motor torque. In this thesis, three different motor current fault scenarios are considered and the fault indicator signals that are produced in the residual generator are shown in Figs. 3.7- 3.9.

- First scenario: In this case, a low motor current (60% drop in nominal value) fault is injected in the x-axis of the satellite at the time sample of 5000. Fig. 3.7 shows the residual signal that is generated along the x-axis of the satellite. This figure shows that the proposed dynamic neural network for the x-axis is capable of detecting the fault successfully.

- Second scenario: In this case, a 50% drop of nominal value of motor current fault is occured in the y-axis of the satellite at the time sample of 5000. Fig. 3.8 shows the residual signal that is generated in the y-axis of the satellite. This figure clearly shows that this dynamic neural network can detect the fault occurence successfully.

- Third scenario: In this scenario, a 70% drop of nominal value of motor current fault is injected in the z-axis of the satellite at the time sample of 5000. The residual signal that is generated in the z-axis of the satellite is depicted in Fig. 3.9. This figure clearly shows that the fault occurrence in the z-axis can be detected using the proposed dynamic neural network successfully.

- Viscous temperature (τ_v) fault. The friction model of the spacecraft is designed for a limited range of temperatures. Since in the friction model of the reaction wheel the bearing viscosity depends on the operating temperature, any fluctuations in the normal temperature will be reflected as fluctuation in the drag torque. In this thesis, three different temperature fault scenarios are considered and the fault indicator signals that are produced in the residual generator are
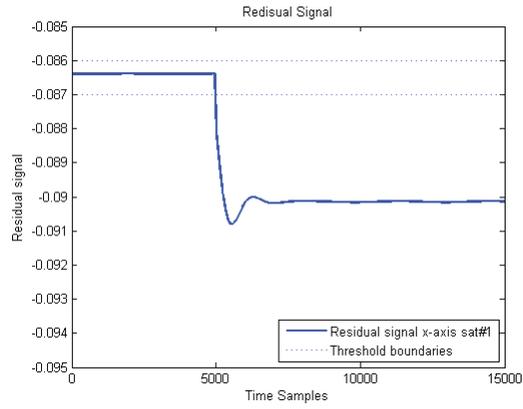
(a)
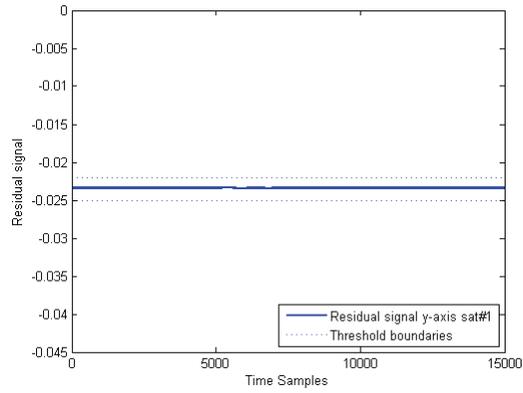
(b)
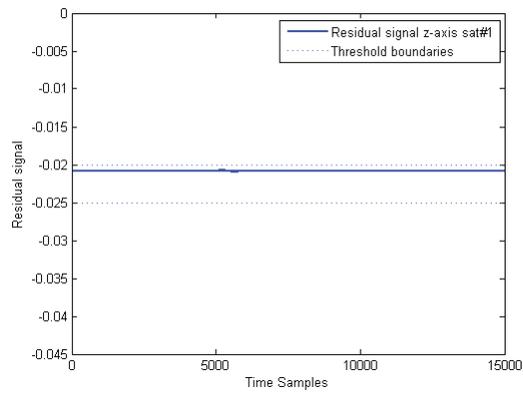
(c)

Figure 3.7: Residual error signals in case of a motor current fault: (a) x-axis, (b) y-axis, and (c) z-axis - Scenario 1.
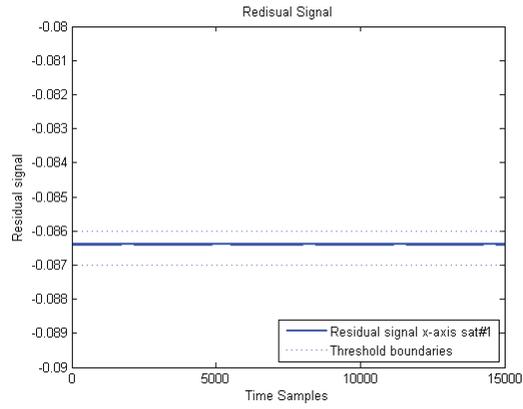
(a)
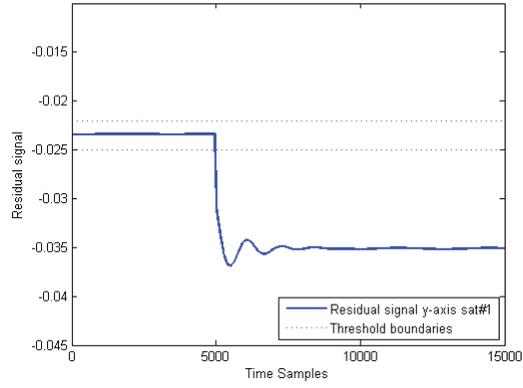
(b)
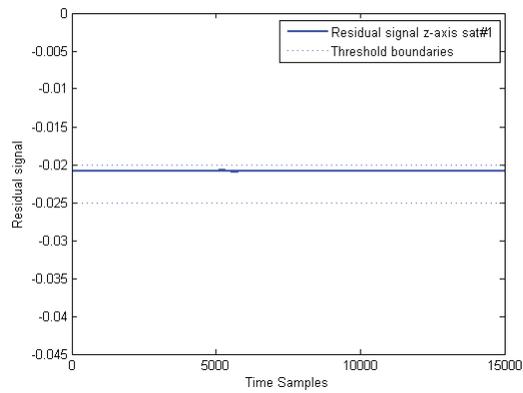
(c)

Figure 3.8: Residual error signals in case of a motor current fault: (a) x-axis, (b) y-axis, and (c) z-axis - Scenario 2.

75
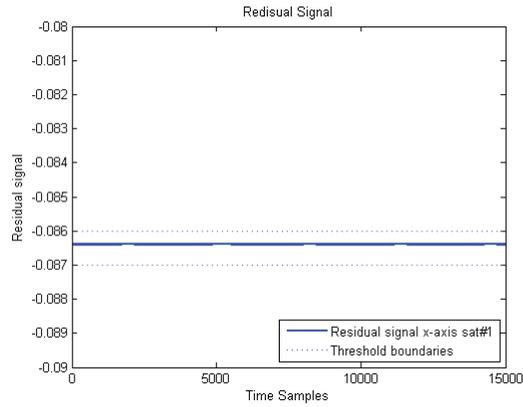
(a)
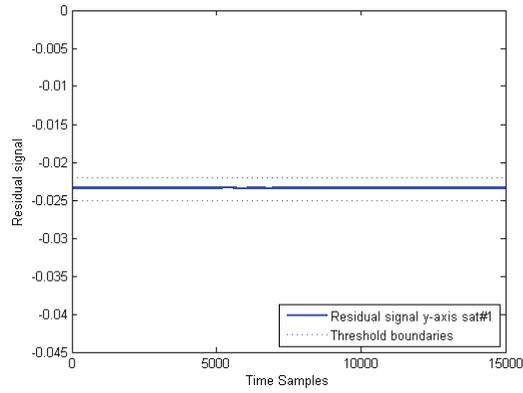
(b)
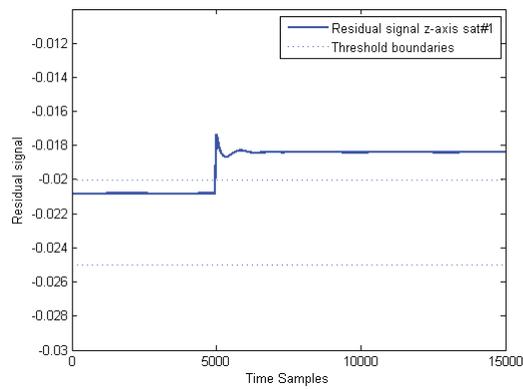
(c)

Figure 3.9: Residual error signals in case of a motor current fault: (a) x-axis, (b) y-axis, and (c) z-axis - Scenario 3.

shown in Figs. 3.10-3.12.

- First scenario: In the first scenario, a temperature fault that results in an increase of 50% in the nominal produced viscous torque is injected in the x-axis of the satellite at the time sample of 5000. Fig. 3.10 shows the residual signal that is generated in the x-axis of the satellite. This figure shows that the proposed dynamic neural network is capable of detecting the fault occurrence successfully.

- Second scenario: In the second case, a high temperature fault (60% increase in the nominal produced viscous torque) is injected in the y-axis of the satellite at the time sample of 5000. Fig. 3.11 shows the residual signal that is generated by the residual generator in the y-axis of the satellite. This figure clearly shows that using this dynamic neural network the fault occurrence can be detected successfully.

- Third scenario: In this case, a temperature fault that results in an increase of 70% in the nominal produced viscous torque is injected in the z-axis of the satellite at the time sample of 5000. The residual signal that is generated by the residual generator in the z-axis of the satellite is shown in Fig. 3.12. This figure clearly shows that the proposed dynamic neural network in z-axis is capable of detecting the fault successfully.

3.2.2 Multiple Fault Scenarios

In order to further evaluate the capabilities of a single satellite fault detection system, the following multiple fault scenarios are considered:

- First scenario: In this scenario, a motor current fault (60% drop in nominal value) has occurred in the x-axis of the satellite at the time sample of 5000
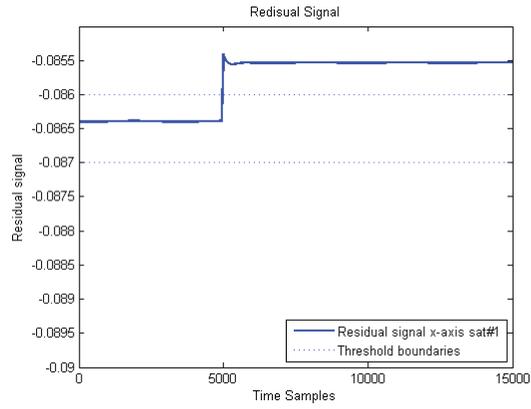
(a)
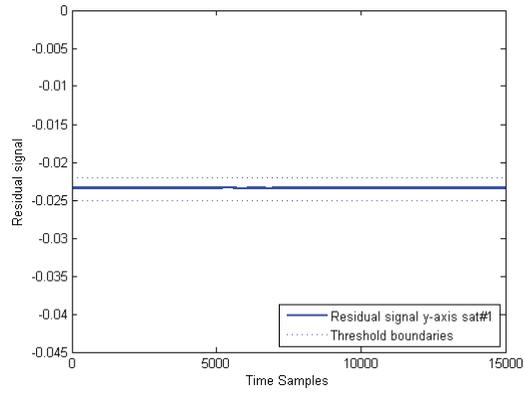
(b)
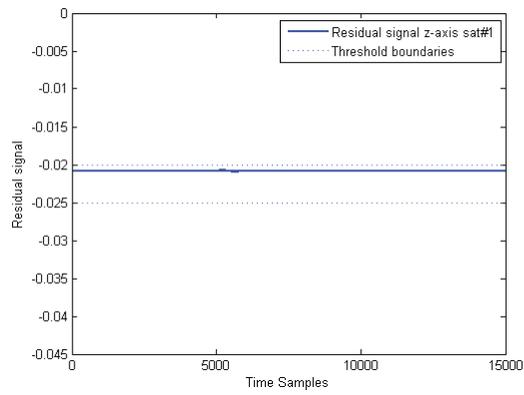
(c)

Figure 3.10: Residual error signals in case of a temperature fault: (a) x-axis, (b) y-axis, and (c) z-axis - Scenario 1.
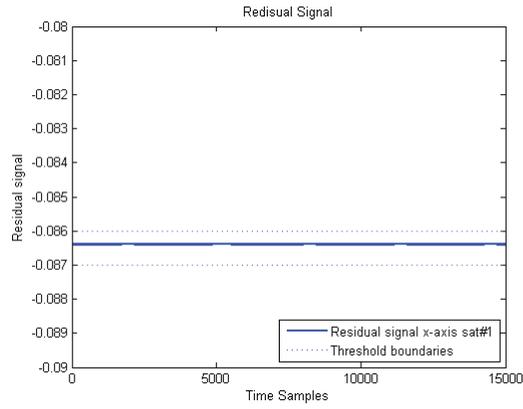
(a)
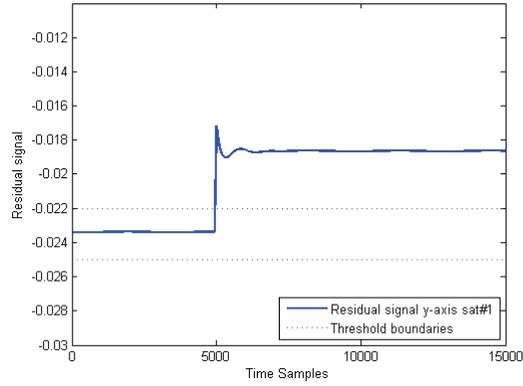
(b)
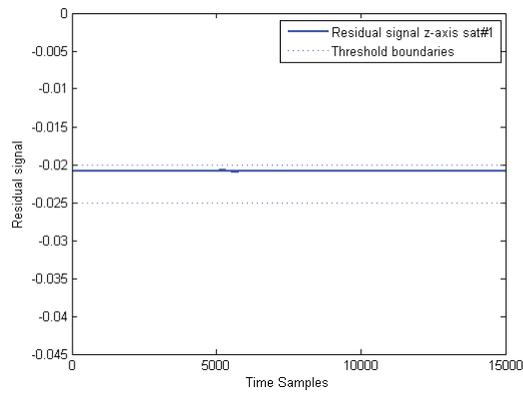
(c)

Figure 3.11: Residual error signals in case of a temperature fault: (a) x-axis, (b) y-axis, and (c) z-axis - Scenario 2.
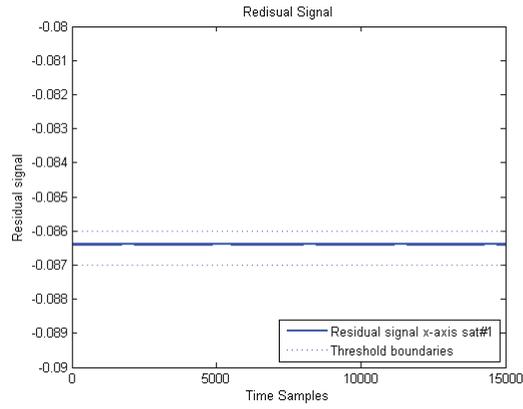
(a)
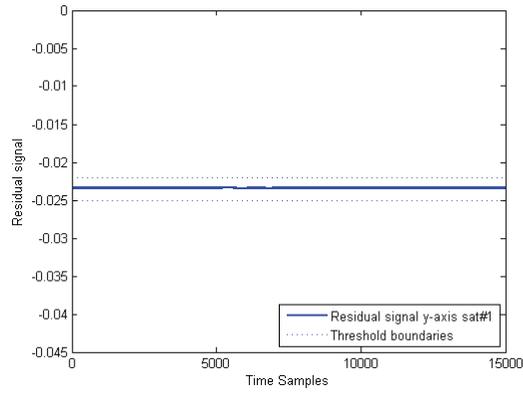
(b)
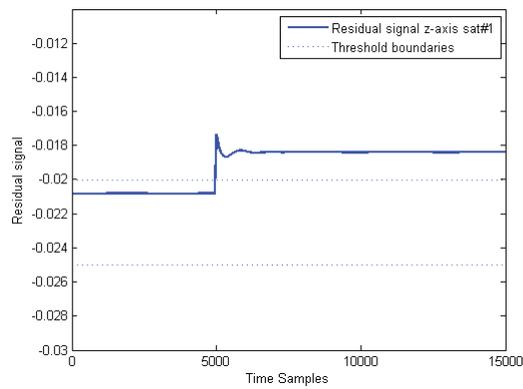
(c)

Figure 3.12: Residual error signals in case of a temperature fault: (a) x-axis, (b) y-axis, and (c) z-axis - Scenario 3.
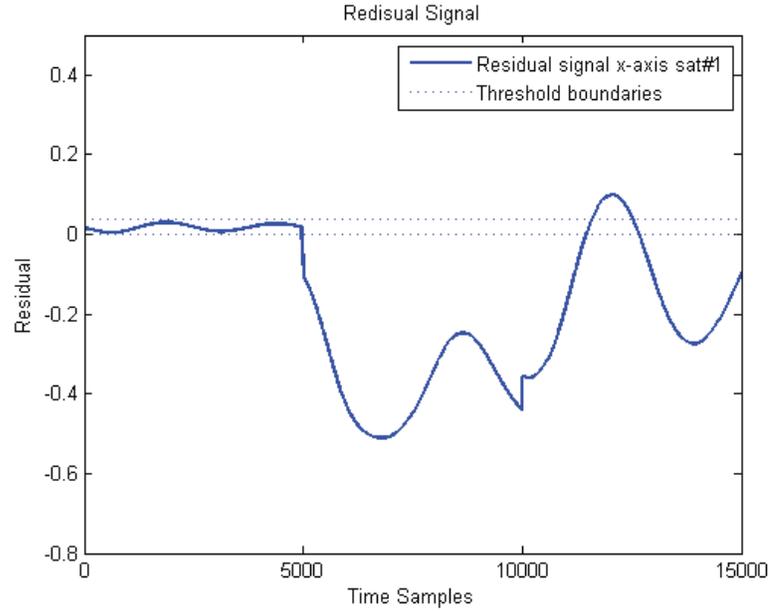
Figure 3.13: Multiple fault scenarios - scenario #1: residual error signal in the x-axis.

and then it is followed by a viscous friction fault (60% increase in nominal value) in x-axis of satellite at the time sample of 10000. Fig. 3.13 shows the residual signals generated by the DNN in the x-axis of the satellite. This figure shows that when the motor current fault occurs at the time sample of 5000, the residual signal passes the threshold and indicates a faulty situation. When the temperature fault occurs at the time sample of 10000, the residual signal still stays unhealthy, but it generates false alarms (actual faulty signal, estimated healthy) in some points.

- Second scenario: In this scenario, a motor current fault (60% drop in nominal value) has occurred in the x-axis of the satellite at the time sample of 5000 and then at the time sample of 10000, a bus voltage fault (60% drop in nominal value) has occurred in the x-axis of the satellite at the time sample of 10000. The residual signal that is generated by the DNN in the x-axis of the satellite is depicted in Fig. 3.14. This figure shows that when the motor current fault
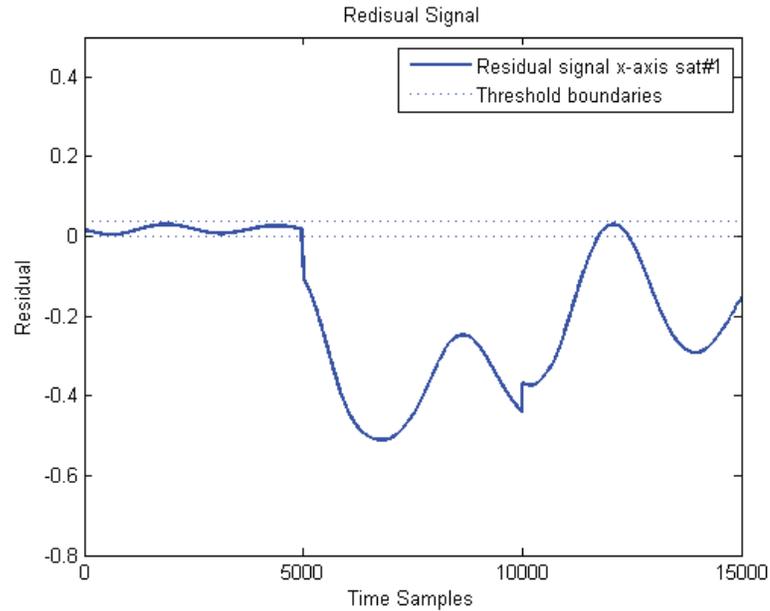
Figure 3.14: Multiple fault scenarios - scenario #2: residual error signal in the x-axis.

occurs at the time sample of 5000, the residual signal exceeds the threshold and indicates the fault occurrence. When the bus voltage fault occurs at the time sample of 10000, the residual signal still remains faulty, however some false alarms (actual faulty signal, estimated as a healthy signal) are also generated.

- Third scenario: In the third scenario, a high temperature fault (70% increase in nominal value of viscous friction) has occurred in the x-axis of the satellite at the time sample of 5000 and then it is followed by a bus voltage fault (70% drop of nominal value) in the x-axis of the satellite at the time sample of 10000. Fig. 3.15 shows the residual signal that is generated by the DNN in the x-axis of the satellite. This figure clearly shows that when the temperature fault occurs at the time sample of 5000, the residual signal passes the threshold and becomes faulty. The residual signal still remains faulty when the bus voltage fault occurs at the time sample of 10000. Some false alarms (actual faulty signals that are estimated to be healthy signals) are also generated in some points.
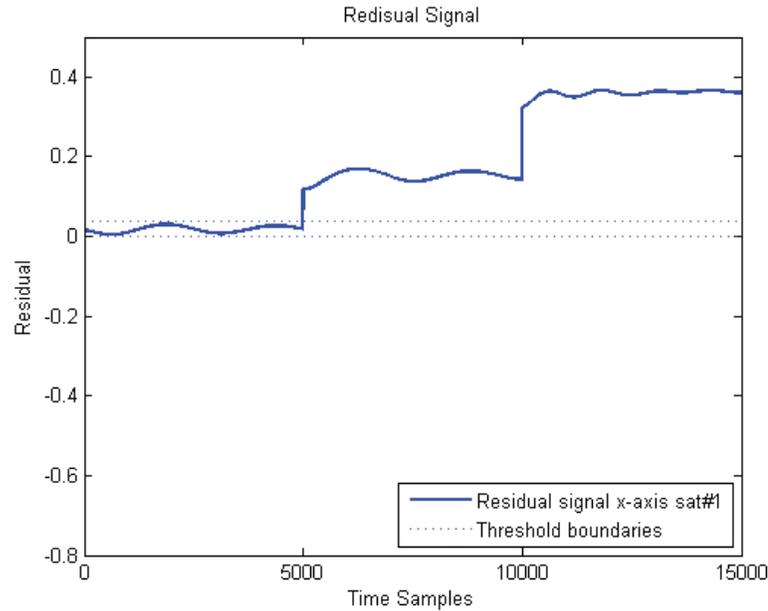
Figure 3.15: Multiple fault scenarios - scenario #3: residual error signal in the x-axis.

- Fourth scenario: In this scenario, a high temperature fault that results in 80% increase in the nominal value of the viscous friction has occurred in the x-axis of the satellite at the time sample of 5000 and then it is followed by a motor current fault (60% drop in nominal value) in the x-axis of the satellite at the time sample of 10000. The residual signal that is generated by the DNN in the x-axis of the satellite is depicted in Fig. 3.16. When the temperature fault occurs at the time sample of 5000, the residual signal passes the threshold boundaries and becomes faulty. When the bus voltage fault occurs at the time sample of 10000, the residual signal still stays out of the threshold boundaries and indicates the reaction wheel to be faulty, but in some points the DNN fails to detect the fault occurrence and the actual faulty residual signal is estimated to be fault-free which generates some false alarms.

- Fifth scenario: In this scenario, a bus voltage fault (90% drop in nominal value) has occurred in the x-axis of the satellite at the time sample of 5000 and then

83
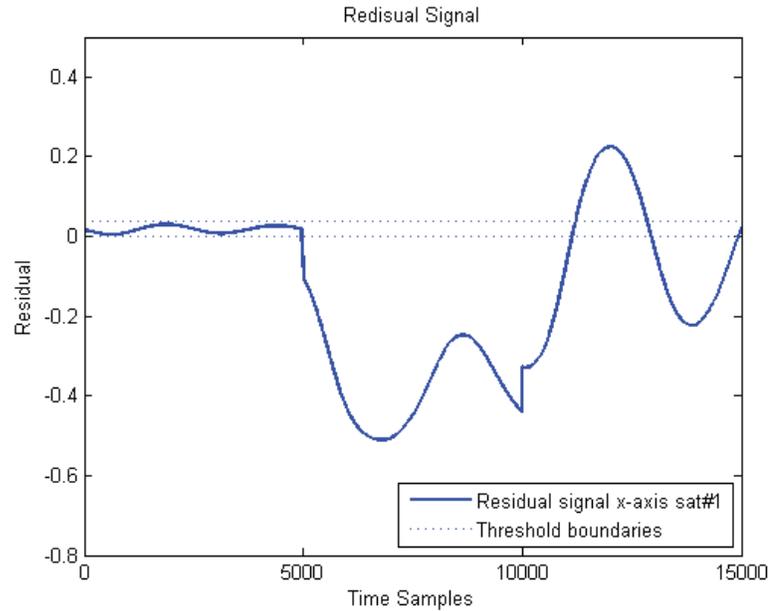
Figure 3.16: Multiple fault scenarios - scenario #4: residual error signal in x-axis.

it is followed by a temperature fault (60% increase in nominal value of viscous friction) in the x-axis of the satellite at the time sample of 10000. Fig. 3.17 shows the residual signal generated by the DNN in the x-axis of the satellite. This figure shows that when the bus voltage fault occurs at the time sample of 5000, the residual signal passes the threshold and indicates the fault occurrence. When the temperature fault occurs at the time sample of 10000, the residual signal still stays in faulty situation.

The results of fault detection for the above five fault scenarios are summarized in Table 3.1. This table shows that the fault detection system designed for a single satellite has the capability of detecting bus volltage actuator faults without a significant time delay. The proposed single satellite FD system however fails to detect bus voltage faults smaller than 50% drop in the nominal value. Table 3.2 summarizes the results of the fault detection process for a single satellite under different motor current fault
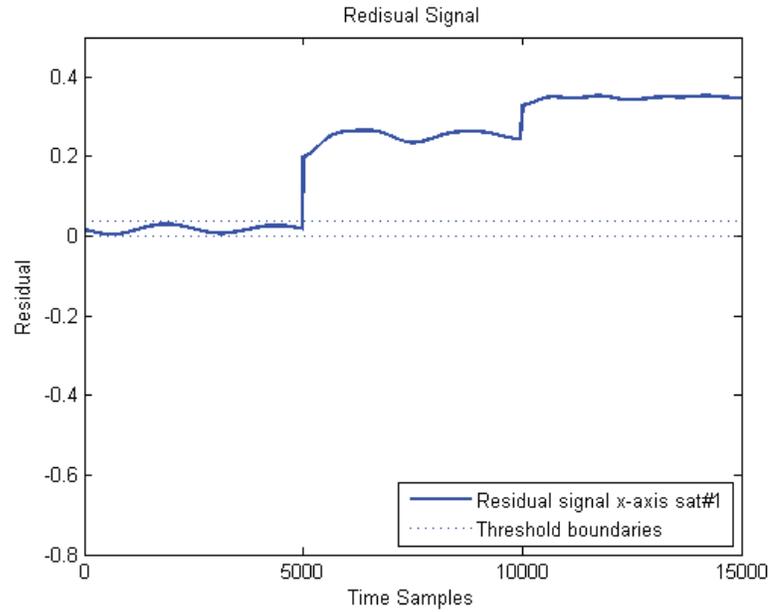
Figure 3.17: Multiple fault scenarios - scenario #5: residual error signal in x-axis.

Table 3.1: Summary of the bus voltage fault detection results for a single satellite.

Faulty Axis	Fault Type	Fault Severity	Injection Time	Detection Time		
				x	y	z
x	Bus Voltage	80%	5000	5000	-	-
y	Bus Voltage	60%	5000	-	5000	-
z	Bus Voltage	50%	5000	-	-	5000
x	Bus Voltage	40%	5000	-	-	-
y	Bus Voltage	30%	5000	-	-	-
z	Bus Voltage	20%	5000	-	-	-

Table 3.2: Summary of the motor current fault detection results for a single satellite.

Faulty Axis	Fault Type	Fault Severity	Injection Time	Detection Time		
				x	y	z
x	Motor Current	60%	5000	5000	-	-
y	Motor Current	50%	5000	-	5000	-
z	Motor Current	70%	5000	-	-	5000
x	Motor Current	40%	5000	-	-	-
y	Motor Current	30%	5000	-	-	-
z	Motor Current	20%	5000	-	-	-

Table 3.3: Summary of the temperature fault detection results for a single satellite.

Faulty Axis	Fault Type	Fault Severity	Injection Time	Detection Time		
				x	y	z
x	Viscous Temperature	50%	5000	5000	-	-
y	Viscous Temperature	60%	5000	-	5000	-
z	Viscous Temperature	70%	5000	-	-	5000
x	Viscous Temperature	40%	5000	-	-	-
y	Viscous Temperature	30%	5000	-	-	-
z	Viscous Temperature	20%	5000	-	-	-

scenarios. Once a fault occurs in one axis of a single satellite, the dynamic neural network along the faulty axis can detect the fault immediately. However, this method fails to detect motor current faults smaller than a 50% drop of the nominal values. The results of the fault detection process for temperature faults in the actuator of a single satellite are summarized in Table 3.3. This table shows that by using the fault detection system in a single satellite, the DNN located in the faulty axis of the satellite can detect the faults without a significant time delay, but the system fails to detect temperature faults smaller than a 50% drop of the nominal values.

3.3   Confusion Matrix Analysis

To evaluate the performance of the proposed FD scheme, we use the confusion matrix method [85]. The structure of this matrix is shown below. The specific evaluation terms are: Accuracy, True Healthy, False Healthy, True Faulty, False Faulty and

Precision, respectively. These are given in more detail below:

$$\begin{bmatrix} A & B \\ C & D \end{bmatrix} \tag{3.2}$$

A: Actual Faulty/Predicted Faulty

B: Actual Faulty/Predicted Healthy

C: Actual Healthy/ Predicted Faulty

D: Actual Healthy/ Predicted Healthy

$$Accuracy = \frac{A + D}{A + B + C + D} \tag{3.3}$$

$$Truehealthy = \frac{D}{C + D} \tag{3.4}$$

$$Falsehealthy = \frac{B}{A + B} \tag{3.5}$$

$$Truefaulty = \frac{A}{A + B} \tag{3.6}$$

$$Falsefaulty = \frac{C}{C + D} \tag{3.7}$$

$$Precision = \frac{D}{B + D} \tag{3.8}$$

Table 3.4: Actual and Detection results in case of the first multiple fault scenario.

DNN #	Actual Healthy	Actual Faulty	Estimated Healthy	Estimated Faulty
DNN x-1	10000 samples	10000 samples	10190 samples	9810 samples

Table 3.5: Actual and Detection results in case of the second multiple fault scenario.

DNN #	Actual Healthy	Actual Faulty	Estimated Healthy	Estimated Faulty
DNN x-1	10000 samples	10000 samples	10640 samples	9360 samples

3.3.1 Confusion Matrix Analysis for FD System of a Single Satellite

In order to investigate the capabilities of the proposed FD system in the formation flying mission, various faulty scenarios have been considered. In the first scenario, a motor current fault (60% drop of nominal value) has occurred in the x-axis of the satellite at the time sample of 5000 and then it is followed by a viscous friction fault (60% increase in nominal value) in the x-axis of the satellite at the time sample of 10000. Table. 3.4 shows the actual healthy and actual faulty output signals and the classification that is obtained by using the FD scheme. In the second scenario a motor current fault (60% drop of nominal value) has occurred in the x-axis of the satellite at the time sample of 5000 and then it is followed by a bus voltage fault (60% drop in nominal value) in the x-axis of the satellite at the time sample of 10000. The actual healthy and actual faulty output signals and the classification that is obtained by using the FD scheme are depicted in Table. 3.5. In the third scenario, a viscous friction fault (70% increase in nominal value) has occurred in the x-axis of the satellite at the time sample of 5000 and then at the time sample of 10000 a bus voltage fault (70% drop in nominal value) has occured in the x-axis of the satellite at the time sample of 10000. Table. 3.6 shows the actual healthy and actual faulty output signals and the classification results that are obtained by using the proposed FD scheme. In the fourth scenario, first a viscous friction fault (80% increase in nominal value) has

Table 3.6: Actual and Detection results in case of the third multiple fault scenario.

DNN #	Actual Healthy	Actual Faulty	Estimated Healthy	Estimated Faulty
DNN x-1	10000 samples	10000 samples	9910 samples	10090 samples

Table 3.7: Actual and Detection results in case of the fourth multiple fault scenario.

DNN #	Actual Healthy	Actual Faulty	Estimated Healthy	Estimated Faulty
DNN x-1	10000 samples	10000 samples	10300 samples	9700 samples

occurred in the x-axis of the satellite at the time sample of 5000 and then a motor current fault (60% drop in nominal value) has occured in the x-axis of the satellite at the time sample of 10000. The actual healthy and actual faulty output signals and the classification results that are obtained by using the proposed DNNs is provided in Table. 3.7. In the fifth scenario, first a bus voltage fault (90% drop in nominal value) has occurred in the x-axis of the satellite at the time sample of 5000 and then at the time sample of 10000 a temperature fault that results in a 60% increase in the nominal value of the viscous friction has occured in the x-axis of the satellite. Table. 3.8 shows the actual healthy and actual faulty output signals and the fault detection results that are obtained by using the proposed DNNs.

According to Tables. 3.4 to 3.8 the confusion matrix parameters depicted in Table 3.9 are obtained for a single satellite. The results obtained from the confusion matrix is depicted in Table 3.10. According to Table 3.10 dynamic neural network located in faulty axis of the faulty spacecraft can classify 99% of healthy signals and 98% of faulty signals successfully. The accuracy level (98%) and the precision level (97%) of this method are highly acceptable.

Using the dynamic neural network that is developed for a single satellite, bus

Table 3.8: Actual and Detection results in case of the fifth multiple fault scenario.

DNN #	Actual Healthy	Actual Faulty	Estimated Healthy	Estimated Faulty
DNN x-1	10000 samples	10000 samples	9920 samples	10080 samples

Table 3.9: Confusion matrix parameters for a single satellite.

DNN #	A	B	C	D
DNN x-1	48870 samples	1130 samples	170 samples	50000 samples

Table 3.10: Confusion matrix results for a faulty satellite.

Accuracy	98%
True healthy	99%
False healthy	2%
True faulty	98%
False faulty	1%
Precision	97%

voltage faults greater than 50% drop of nominal values, motor current faults greater than 50% drop of nominal values and temperature faults greater than 60% drop of nominal values can be detected in a single satellite. The proposed fault detection system may fail to detect the presence of low severity faults. In an individual operating satellite these low severity faults may not cause any serious difficulties with the specifications of the overall mission, however they can cause significant impact on the satellite's attitude or rates in a given precision formation flight of a network of satellites. Consequently, in order to detect these low severity faults a novel fault detection system is required to be designed and developed for a formation of spacecraft. The development and design of such a computationally intelligent-based scheme and strategy are the main contributions of this thesis.

3.4 Problem Definition and Motivation for a Formation of Satellites

In the previous section the capabilities of a dynamic neural network-based fault detection method for a single satellite that is proposed in [43] is investigated through

various single and multiple fault scenarios. It is shown that the proposed single satellite fault detection method has the capability of detecting major actuator faults in a single satellite, but it fails to detect low severity faults in the actuators of a satellites. These low severity faults usually do not cause any serious problem in a single satellite space missions, but in a formation flying mission, they may affect the attitude of a satellite and even result in serious damage in the formation.

On the other hand, in single satellite fault diagnosis methods in the literature, each satellite can only detect the actuator faults of itself, therefore, if the local fault diagnosis system fails, there is no way to detect the fault. In order to increase the reliability of the fault diagnosis system in a formation flying of satellites it is important to propose a decentralized fault diagnosis system, by which a fault in one satellite can be also detected by its neighboring satellites.

One of the main contributions of this thesis is to propose a decentralized fault detection methodology that can detect both high severity and low severity faults in a formation flying of satellites. In this thesis, two fault detection schemes are studied. In the first scheme, the data exchange and communication links are assumed to be unidirectional, implying that the DNNs in the fault diagnosis system in each satellite use the relative attitude measurements of that satellite with respect to its adjacent satellites. In the second scheme, the data exchange and communication links are bidirectional, implying that the DNNs in the fault diagnosis system in each satellite uses the relative attitude of that satellite with respect to its two adjacent neighbors.

The capabilities of these two schemes are studied in this chapter and it is shown that although the second scheme requires more data exchange, but it has the ability to detect faults with shorter time delays and it can improve the precision and the accuracy performance merits.

3.5 Fault Detection System for Formation of Satellites - First Scheme

The schematic representation of the proposed fault detection (FD) system based on the formation flying relative attitudes is depicted in Fig. 3.19. In this scheme, one dynamic neural network is located in each axis of a spacecraft. A three level system is shown in this figure, namely: attitude control subsystem (ACS) of the i-th satellite, attitude control subsystem (ACS) of the $(i+1)$-th satellite, and the FD scheme for the x-axis of of the i-th satellite. In this chapter, a four spacecraft formation flying mission is studied and in the first scheme it is assumed that each satellite receives attitude information from its adjacent neighbor, i.e. the $(i+1)$-th satellite. The data communication flow among the satellites in this mission are depicted in Fig. 3.18 where $\mathbf{q} = [q_1^i, q_2^i, q_3^i, q_4^i]^T$ represents the attitude vector of the i-th satellite. Each dynamic neural network is trained based on set of input/output data that are collected from the relative attitude determination sensors of the 3-axis attitude control subsystem of satellites. In this scheme, $u = [q_1^{i+1/i}, q_2^{i+1/i}, q_3^{i+1/i}, V_{command}^i]$ is used as an input vector for the training the dynamic neural network and $y = [\tau_{reaction}^i]$ is used as the output vector for training phase in which $q_1^{i+1/i}$, $q_2^{i+1/i}$, and $q_3^{i+1/i}$ are relative attitude of the i-th satellite with respect to the $(i+1)$-th satellite and $V_{command}^i$ denotes the commanded voltage of the i-th satellite and $\tau_{reaction}^i$ denotes the reaction torque of the i-th satellite.

3.6 Training Phase

The training phase is carried out by using an extended dynamic back-propagation method for about 50000 time samples for each axis and each time sample is equal to 0.01 seconds. All the input and output vectors are normalized in the range [-1
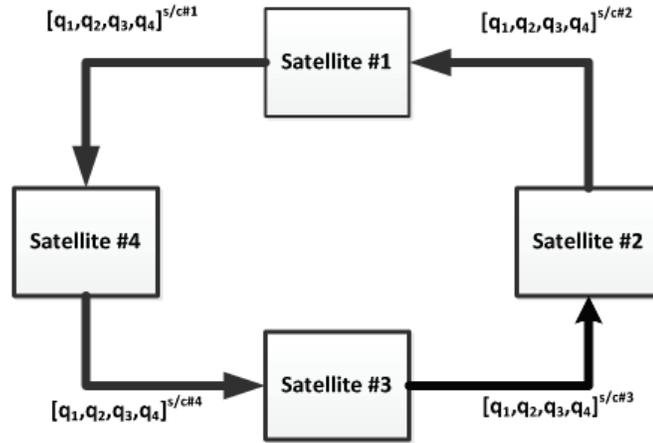
Figure 3.18: Communication links among the four spacecraft in the formation - first scheme.
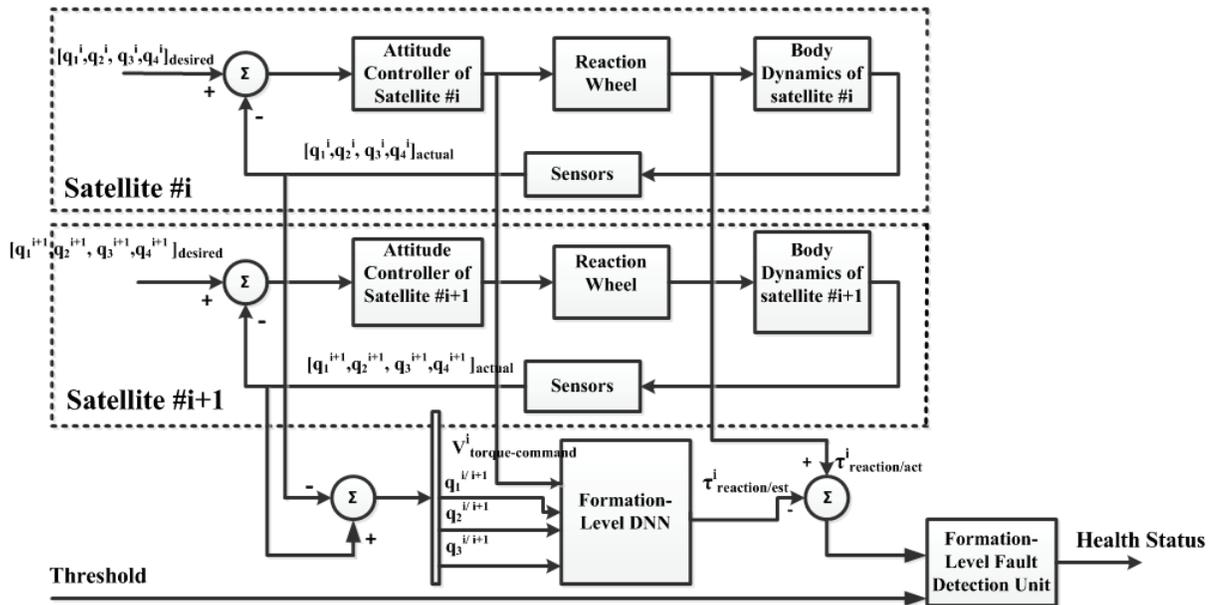
Figure 3.19: Structure of the fault detection (FD) system in a formation flying of satellites - first scheme.

+1]. Table 3.11 shows the dynamic neural network parameters for the FD system in each spacecraft of the formation where n is the number of hidden layers, N_1 is the number of neurons in the first hidden layer and η is the learning rate. The dynamic neural networks are trained until a termination criterion is satisfied. In this section, the termination criterion that is used is the mean squared error (mse) criterion. Adaption laws are based on the steepest descent gradient method and conventional back-propagation learning law. The parameters are updated so that the norm of the identification error is minimized. Generally, an identification error can be defined as:

$$E(t) = \frac{1}{2} \sum_{k=1}^{K} (y_k(t) - y_k^{desired}(t))^2 \tag{3.9}$$

The training process is accomplished by using the Monte Carlo simulations under different noisy conditions for 50000 samples and each sample is 0.001 seconds. The network is trained for 100 different pairs of input/output data in presence of a normally distributed noise with zero mean and standard deviation of 0.01 differences between the maximum and the minimum values in the input/output data intervals. The performance of the network during the training phase along the x-axis of the four satellite in the formation is shown in Fig. 3.20. The mean square error (mse) for the other axes of other satellites are obtained in a similar way. The average value of the mean square error in 100 training simulations is 0.058 and its standard deviation is 0.0008, which is quite acceptable.

3.7   Testing Phase

The representation capability of the trained networks is evaluated through generalizing them with other healthy data sets. Fig. 3.21 shows the actual output of the
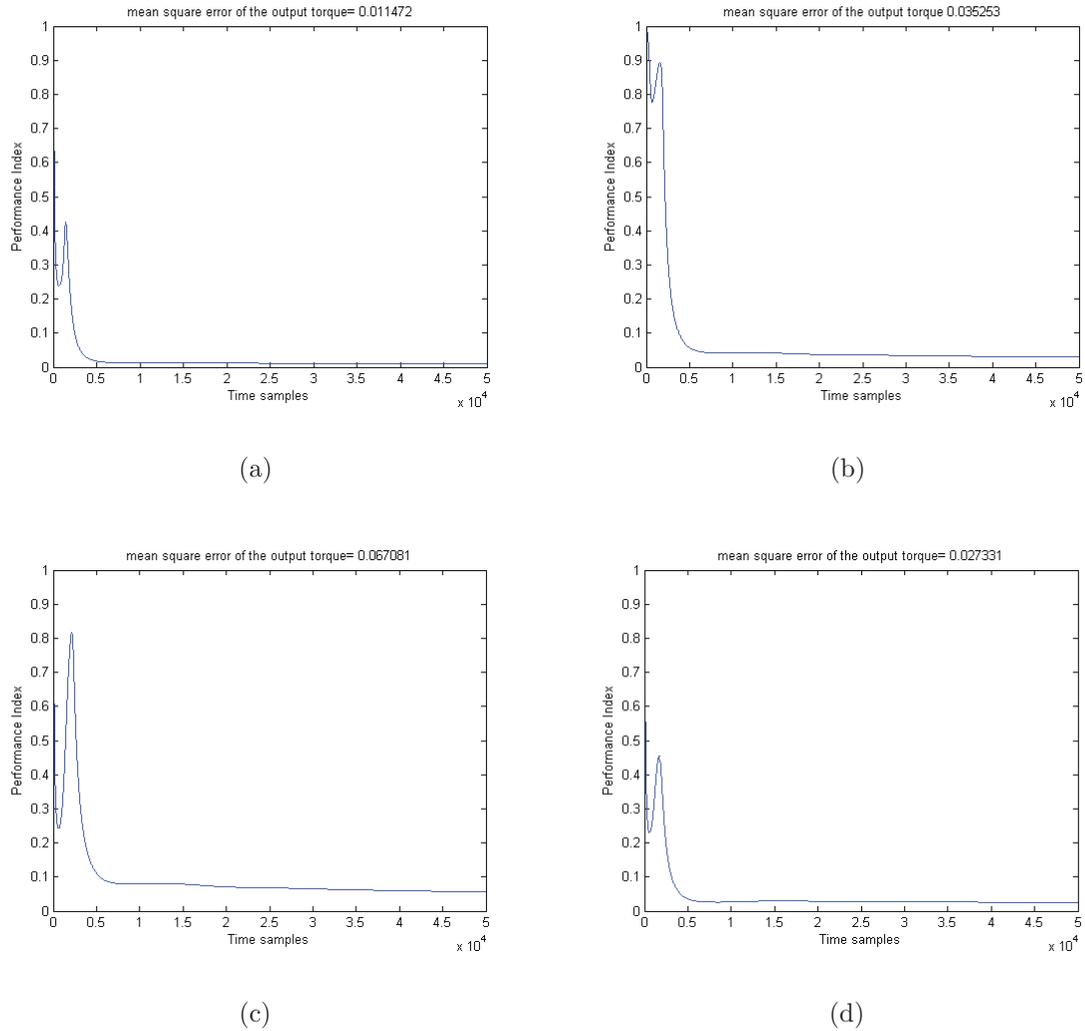
Figure 3.20: The performance index (mean squared error of the output reaction torque) curve for the dynamic neural network- x-axis of (a) satellite #1, (b) satellite #2 (c) satellite #3 (d) satellite #4.

Table 3.11: DNN characteristics in the learning phase.

Spacecraft #	Network Size	Number of Iterations	Performance Index	Learning Rate
1	N_{1-10-1}	50000	0.011	0.05
2	N_{1-8-1}	50000	0.035	0.01
3	N_{1-8-1}	50000	0.067	0.01
4	N_{1-6-1}	50000	0.0273	0.03

reaction wheel and the neural network output in the testing phase for the three axes of the satellites #1 in the formation. This figure shows that the output of the trained dynamic neural network follows the actual output of the system quite closely; therefore it has the capability of detecting faults and deviations in the input signal.

The testing phase is accomplished for 100 different pairs of input/output data in presence of a normally distributed noise with zero mean and standard deviation of 0.01 differences between the maximum and the minimum values in the input/output data intervals. The average value of the mean square error in 100 testing samples is 0.08 and its standard deviation is 0.001, which is quite acceptable. The testing curves for other axes of each satellite can be obtained similarly.

3.8   Fault Detection Threshold Determination

After training and testing the dynamic neural networks by using healthy input/output data set, this network can now be used for generating residual signals. In this step, the output of the neural network is compared with the actual output of the reaction wheel and their differences are considered as the residual signals. The residual signal has to be compared with a predefined threshold value to determine the health status of the system. If the residual signal exceeds the threshold value, this implies that a fault has happened in the corresponding axis of the satellite. The residual signals that are collected during various fault free formation flying missions can be used to determine the thresholds. The mean values of generated residual signals $(\bar{X})$ and their standard deviation (σ) are calculated, and the threshold values can be calculated by using the following formula:

$$t.h = \bar{X} \pm 3\sigma \tag{3.10}$$
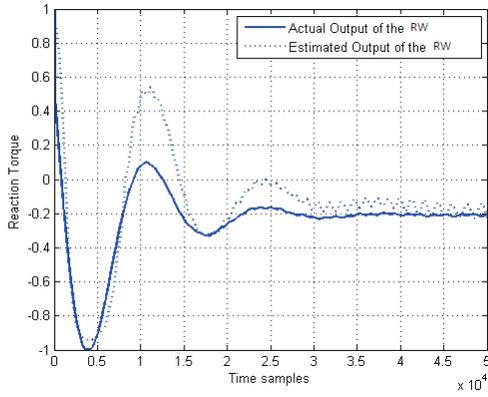
(a)
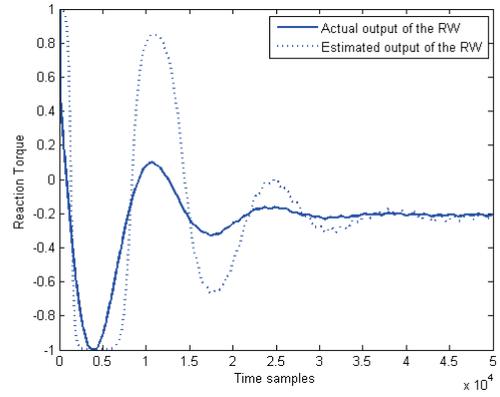
(b)
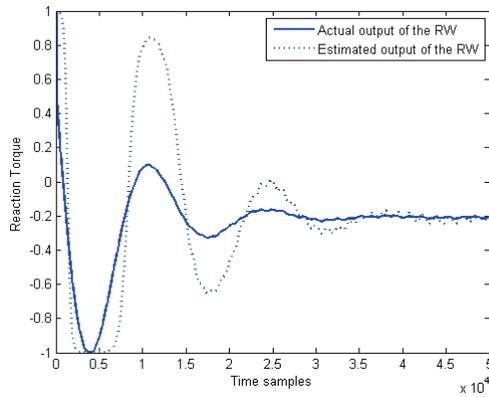
(c)

Figure 3.21: Testing curve (actual and estimated outputs) for the DNN - (a) x-axis, (b) y-axis, and (c) z-axis of the satellite #1.

3.9 Actuator Fault Scenarios

In this chapter, the following formation flight mission is simulated. Four satellites having bi-directional ring topology are controlled by using consensus-based virtual structure controller that is proposed in [16] are considered. These four satellites are located on a plane and distributed equally along a circle with diameter of 0.7 kilometer. It is assumed that the four spacecraft formation evolves as a rigid body and the formation shape is preserved, and in the healthy situation each satellite preserves a fixed relative orientation within the formation throughout the maneuvers. Different types of faulty scenarios under worst case noisy conditions are considered and have been injected to the closed-loop attitude controlled system in each satellite's axis. The process of fault detection can be accomplished by using the simple threshold technique described in previous section. Any deviation from the threshold ranges will be considered as a fault. The thresholds are selected after performing different simulations under different operating conditions to make sure that the proposed fault detection technique will work successfully with minimum false alarms. the types of actuator faults considered are as follows:

- Bus voltage (V_{BUS}) fault

  In order to investigate the capabilities of the proposed DNNs in formation flying of satellites missions, the following bus voltage fault scenarios are considered:

  – First scenario: In this case, a low bus voltage (70% drop from the nominal value) fault is injected in the x-axis of the satellite #2 at the time sample of 5000. Fig. 3.22 shows the residual signal that is generated in the x-axis of the satellite #2 and the satellite #1 (its neighbor). This figure clearly shows that the proposed dynamic neural network along the x-axis of the satellite #2 and the DNN along the x-axis of the satellite #1 can detect

the fault successfully.

– Second scenario: In this scenario, a low bus voltage (45% drop from the nominal value) fault has occured in the z-axis of the satellite #2 at the time sample of 10000. The residual signals that are generated along z-axis of the satellite #2 and the satellite #1 (its neighbor) are shown in Fig. 3.23. This figure clearly shows that the proposed dynamic neural network along z-axis of satellite #2 and the DNN along x-axis of satellite #1 are capable of detecting the fault successfully.

- Motor current (I_m) fault

In order to evaluate the capabilities of the trained DNNs in formation flying of satellites, the following motor current fault scenarios are considered:

– First scenario: In this case, a low motor current (50% drop of nominal value) fault is injected in the x-axis of satellite #3 at the time sample of 10000. Fig. 3.24 shows the residual signals that are generated along the x-axis of the satellite #3 and the satellite #2 (its neighbor). This figure clearly shows that the proposed dynamic neural network along the x-axis of the satellite #3 and the DNN along the x-axis of the satellite #2 can detect the fault successfully.

– Second scenario: In the second scenario, a 80% drop from the nominal value of motor current fault has occured in the x-axis of the satellite #4 at the time sample of 10000. The output of DNN-based residual generators is shown in Fig. 3.25 for the x-axis of the satellite #4 and the satellite #3 (its neighbor). This figure shows that the fault occurrence can be detected by using the proposed dynamic neural network along the x-axis of the satellite #4 and the DNN along the x-axis of the satellite #3 successfully.
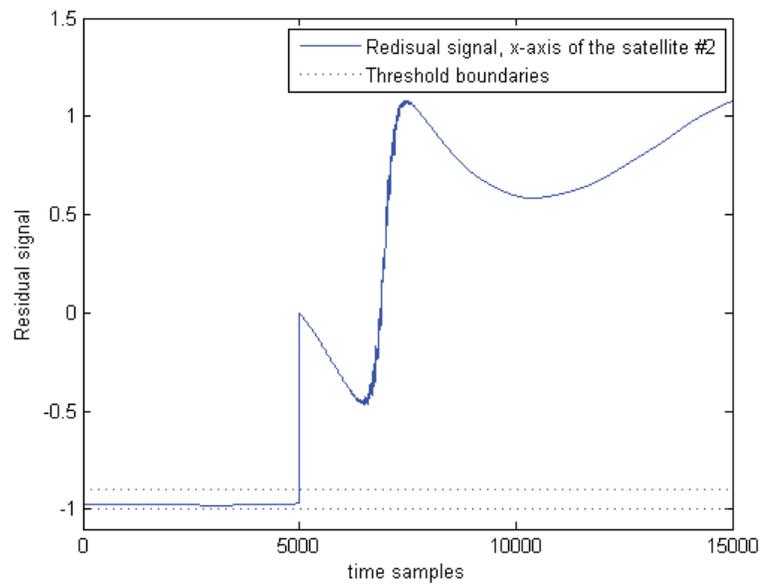
(a)
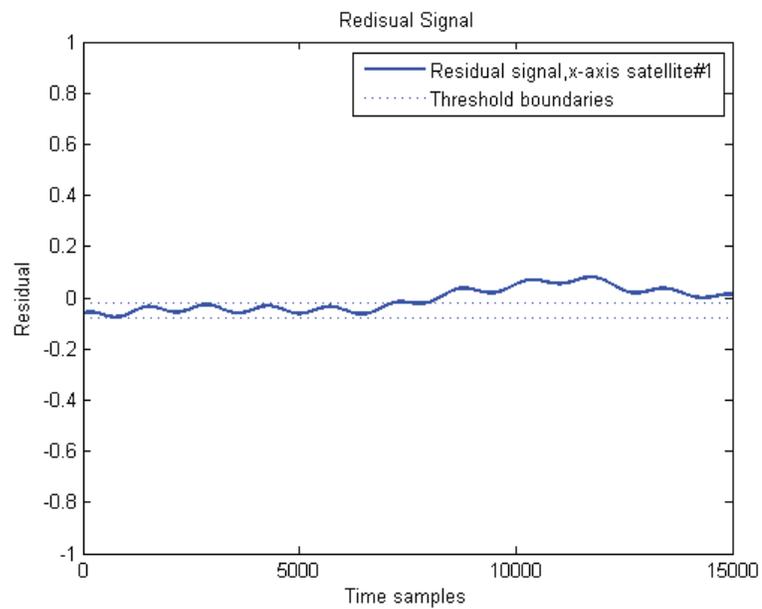
(b)

Figure 3.22: Residual signals corresponding to bus voltage fault - scenario 1: (a) x-axis satellite #2, (b) x-axis satellite #1.
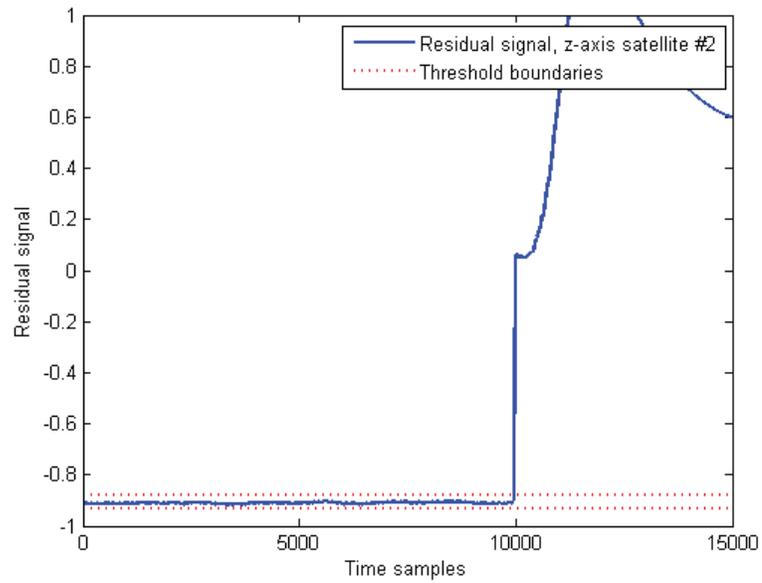
(a)
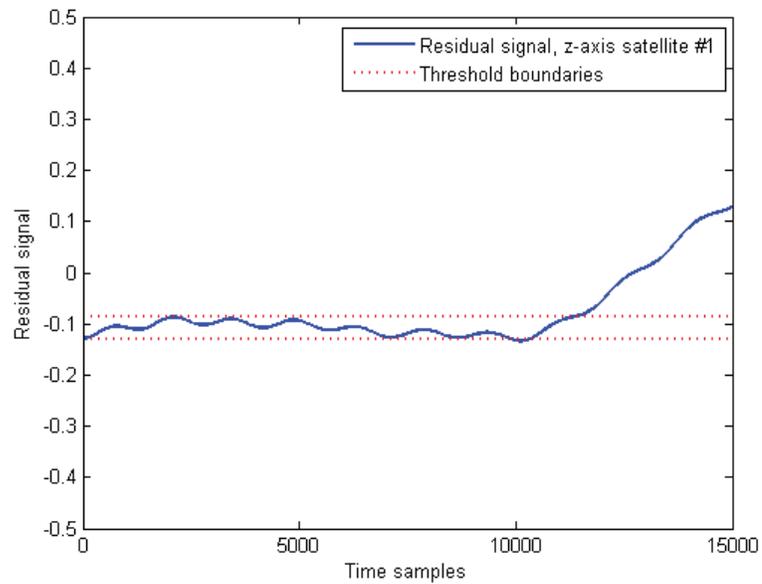
(b)

Figure 3.23: Residual signals corresponding to bus voltage fault - scenario 2: (a) z-axis satellite #2, (b) z-axis satellite #1.
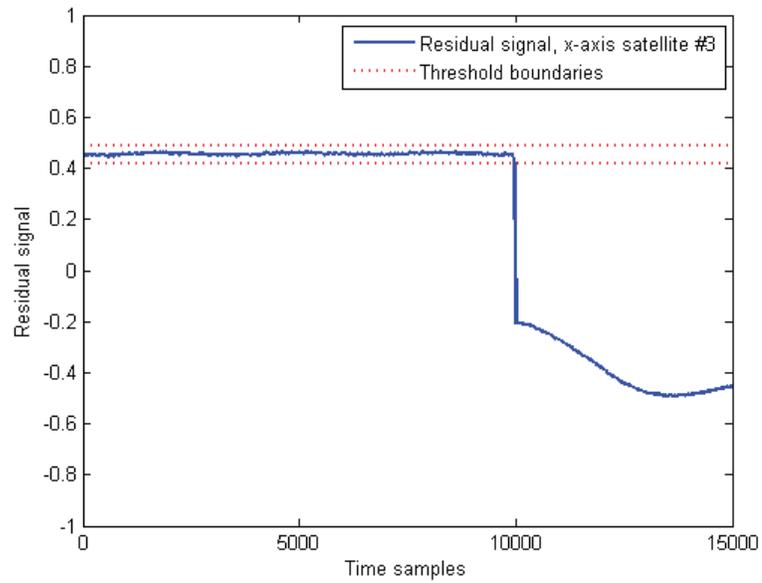
(a)
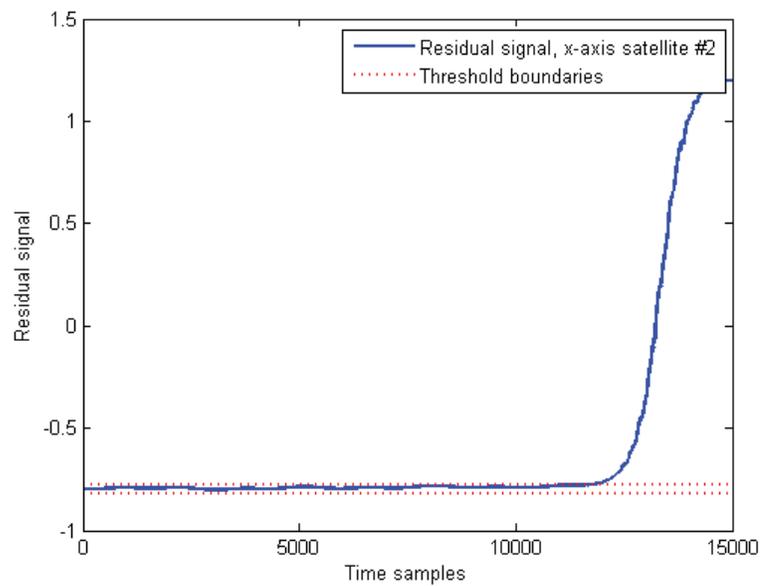
(b)

Figure 3.24: Residual signals corresponding to motor current fault - scenario 1: (a) x-axis satellite #3, (b) x-axis satellite #2.

- Viscous temperature (τ_v) fault

  The capabilities of the trained DNNs in detecting actuator faults in the formation flying of satellites is investigated through the following viscous temperature fault scenarios:

  - First scenario: In this case, a temperature fault that results in a 50% increase in the nominal value of the viscous friction is injected in the x-axis of the satellite #2 at the time sample of 5000. Fig. 3.26 shows the residual signals that are generated along x-axis of the satellite #2 and satellite #1 (its neighbor). This figure clearly shows that by using the proposed dynamic neural network along the x-axis of the satellite #2 and the DNN along x-axis of satellite #1 are capable of detecting the fault successfully.

  - Second scenario: In this case, a 50% increase in nominal value of viscous friction fault has occured in the x-axis of the satellite #1 at the time sample of 10000. The residual signal that is generated along x-axis of the satellite #1 and the satellite #4 (its neighbor) is shown in Fig. 3.27. This figure clearly shows that by using the proposed fault detection scheme, the DNNs located along x-axis of satellite #1 and the x-axis of the satellite #4 can see the effect of fault clearly.

The ability of the proposed method for detecting faults is evaluated in different fault scenarios. Once a fault occurs in the i-th satellite, the fault detection system in satellite #i can detect it immediately and the FD system in satellite #$(i-1)$ can detect the fault with a time delay. Therefore, the first advantage of the proposed formation flying FD scheme is that when a fault occurs in a satellite, it can be
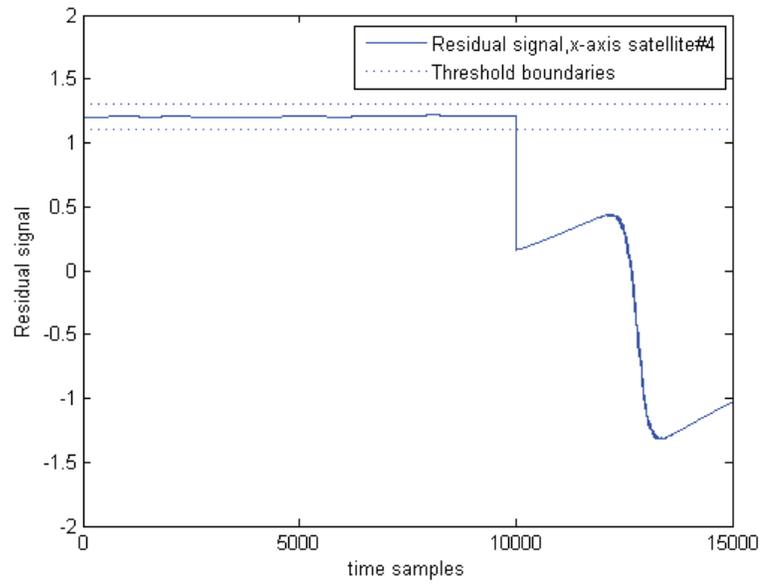
(a)
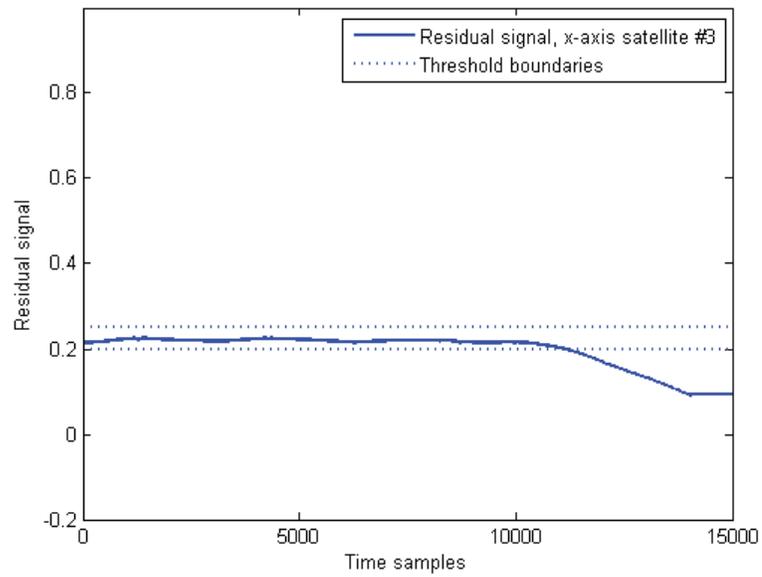
(b)

Figure 3.25: Residual signals corresponding to motor current fault - scenario 2: (a) x-axis satellite #4, (b) x-axis satellite #3.
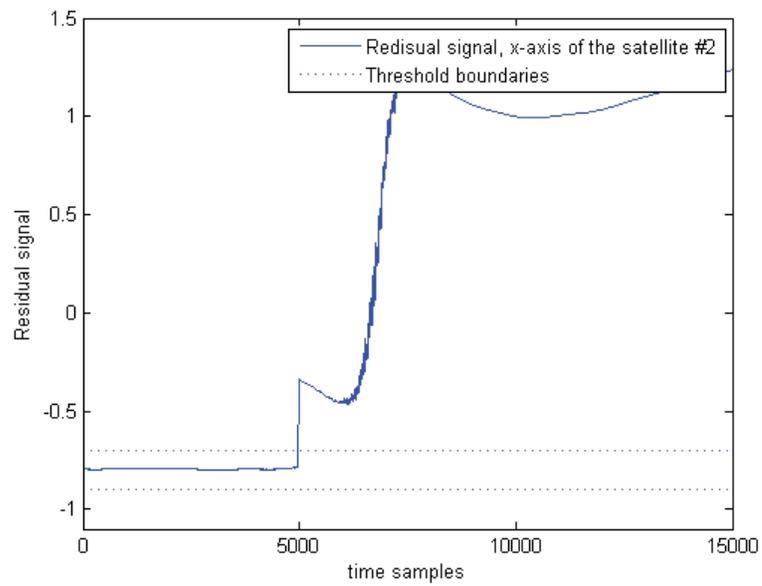
(a)
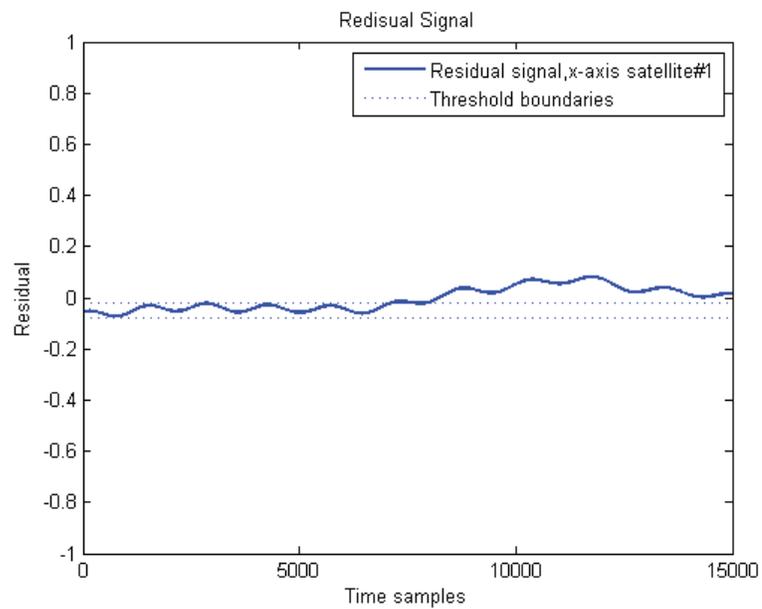
(b)

Figure 3.26: Residual signals corresponding to temperature fault - scenario 1: (a) x-axis satellite #2, (b) x-axis satellite #1.
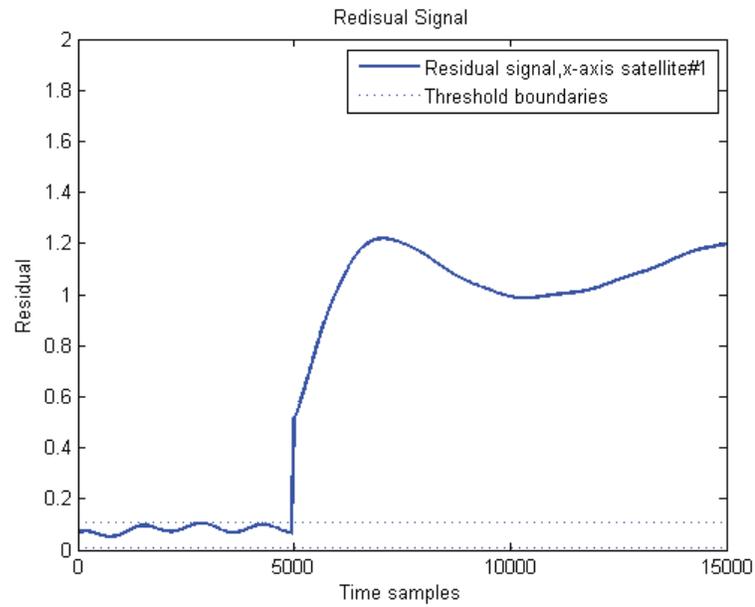
(a)
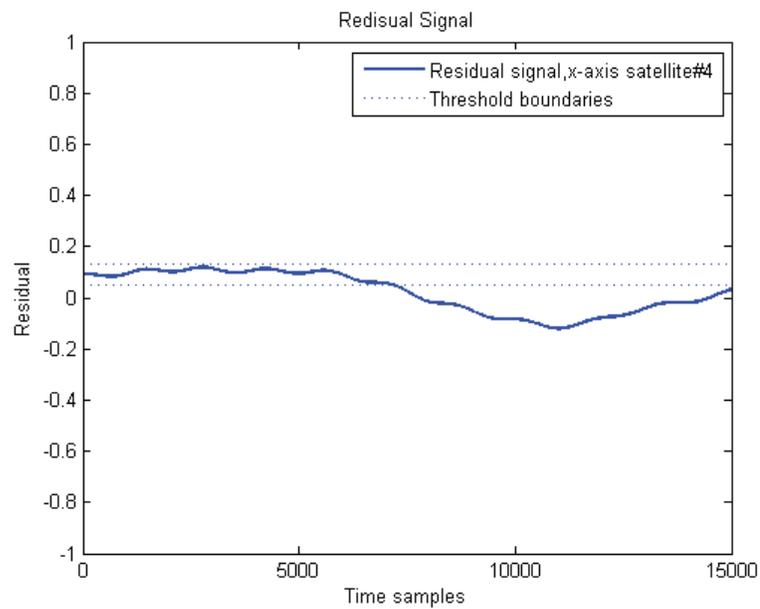
(b)

Figure 3.27: Residual signals corresponding to temperature fault - scenario 2: (a) x-axis satellite #1, (b) x-axis satellite #4.

detected by using local diagnoser immediately and then, after a time delay, the fault can be detected by using DNNs that are embedded in the nearest neighbor of the faulty satellite. When the severity of fault increases, even the next neighbor (satellite $\#(i-2)$) can detect the fault after longer time delay too. Tables 3.12-3.15 show the capabilities of the formation flying FD system in detecting faults under different faulty conditions.

In Table 3.12 a 60% drop of nominal value of the bus voltage fault along the x-axis of the satellite $\#1$ is considered. According to this table, once this fault occurs along the x-axis of satellite $\#1$, the DNN embedded along the x-axis of the satellite $\#1$ can detect the fault immediately, and the DNNs embedded along other axes of satellite $\#1$ can detect the fault after a short time delay (approximately 5 seconds). The attitude information of satellite $\#1$ is transmitted to its adjacent neighbor (i.e. satellite $\#4$). Once a fault occurs in satellite $\#1$ it affects the attitude of satellite $\#4$ and satellite $\#3$. Since the DNNs embedded in satellite $\#4$ are trained based on the relative attitude of satellite $\#4$ with respect to satellite $\#1$, the DNNs embedded in satellite $\#4$ and satellite $\#3$ can detect the fault after a time delay. Since satellite $\#4$ is the closest satellite to satellite $\#1$ in the formation (as far as communication delay), the DNNs in satellite $\#4$ detect the fault in a shorter time delay and since satellite $\#2$ is the farthest satellite from satellite $\#1$ in the formation (as far as communication delay), the DNNs in satellite $\#2$ cannot detect the fault that has occured in satellite $\#1$.

Fault detection time delays in a faulty scenario in which 50% drop of nominal value of the motor current along the x-axis of satellite $\#2$ faulty is happened is depicted in Table 3.13. Once the fault happens along the x-axis of satellite $\#2$, the DNN along the x-axis of satellite $\#2$ can detect the fault immediately and the DNNs along the y and z-axes of satellite $\#2$ can detect the fault after a short time delay.

107

Table 3.12: Fault detection time delays in case of 60% drop of nominal value in the bus voltage of x-axis satellite #1.

Dynamic Neural Network #	Fault Detected	Detection Time Delay
DNN x-1	YES	0 sec
DNN y-1	YES	5 sec
DNN z-1	YES	5 sec
DNN x-2	NO	-
DNN y-2	NO	-
DNN z-2	NO	-
DNN x-3	YES	15 sec
DNN y-3	YES	17 sec
DNN z-3	YES	15 sec
DNN x-4	YES	11 sec
DNN y-4	YES	7 sec
DNN z-4	YES	8 sec

Table 3.13: Fault detection time delays in case of 50% drop of nominal values in the motor current of x-axis satellite #2.

Dynamic Neural Network #	Fault Detected	Detection Time Delay
DNN x-1	YES	13 sec
DNN y-1	YES	10 sec
DNN z-1	YES	10 sec
DNN x-2	YES	0 sec
DNN y-2	YES	6 sec
DNN z-2	YES	2 sec
DNN x-3	NO	-
DNN y-3	NO	-
DNN z-3	NO	-
DNN x-4	YES	15 sec
DNN y-4	YES	20 sec
DNN z-4	YES	15 sec

Table 3.14: Fault detection time delays in case of 10% increase in nominal values of the viscous friction of y-axis satellite #3.

Dynamic Neural Network #	Fault Detected	Detection Time Delay
DNN x-1	NO	-
DNN y-1	NO	-
DNN z-1	NO	-
DNN x-2	YES	14 sec
DNN y-2	YES	16 sec
DNN z-2	YES	14 sec
DNN x-3	YES	7 sec
DNN y-3	YES	0 sec
DNN z-3	YES	8 sec
DNN x-4	NO	-
DNN y-4	NO	-
DNN z-4	NO	-

DNNs in satellite #1 and satellite #4 can also detect the effects of this fault after longer time delays. Since satellite #3 is the farthest satellite from satellite #2 in the formation, the attitude deviations in the satellite #1 cannot affect the attitude of satellite #3, and the DNNs in satellite #3 fail to detect the fault.

A low severity viscous friction fault (10% increase from the nominal value along the y-axis of satellite #3) detection results are shown in Table 3.14. According to this table, once a fault is injected along the y-axis of satellite #3, the DNN embedded along y-axis of satellite #3 can detect the fault immediately, and then the fault is detected by DNNs along the x and z-axes of satellite #3. The closest agent to the satellite #3 in the formation is satellite #2. Therefore, the attitude deviations in satellite #3 will affect the orientation of satellite #2 as well, hence the DNNs embedded in satellite #2 can detect the fault after a time delay. In this case the severity of temperature fault is very low (10% increase from the nominal value), therefore, this fault affects the attitude of satellite#3 (and satellite #2 consequently) slightly. However it has no effect on orientation of satellite #1 in the formation. Therefore only DNNs in satellite #3 and satellite #2 can detect the fault. In Table 3.15, the severity of the

Table 3.15: Fault detection time delays in case of 50% increase in nominal value of the viscous friction of y-axis satellite #3.

Dynamic Neural Network #	Fault Detected	Detection Time Delay
DNN x-1	YES	20 sec
DNN y-1	YES	14 sec
DNN z-1	YES	20 sec
DNN x-2	YES	10 sec
DNN y-2	YES	10 sec
DNN z-2	YES	10 sec
DNN x-3	YES	5 sec
DNN y-3	YES	0 sec
DNN z-3	YES	5 sec
DNN x-4	NO	-
DNN y-4	NO	-
DNN z-4	NO	-

fault is increased (50% increase from the nominal value of viscous temperature along the y-axis of satellite #3), and therefore it affects the attitude of satellite #1 as well, so that the DNNs embedded in satellite #1 can also detect the fault.

3.10 Actuator Multiple Fault Scenarios

In this section in order to evaluate the capability of the proposed FD scheme in detecting multiple faults in a formation flying of spacecraft, different faulty scenarios are considered.

- Multiple faults in different axes of a spacecraft

    - First scenario: In this scenario, a 20% increase in nominal viscous friction (τ_v) fault occurs in the x-axis of satellite #2 at the time sample of 5000, and a low motor current (I_m) fault (10% drop from the nominal value) is injected in the y-axis of satellite #2 at the time sample of 10000. Fig. 3.28 shows the residual signals that are generated along (a) x-axis of the satellite #2 and (b) y-axis of satellite #2 by using the proposed FD system

for formation flying. This figure clearly shows that the proposed formation flying dynamic neural network along the x-axis of satellite #2 can detect the viscous friction fault immediately at the time sample of 5000, and when the motor current fault occurs at the time sample of 10000, the output signal still remains above the threshold value. The DNN along the y-axis of satellite detects the temperature fault in the x-axis after a short time delay, and when the current fault occurs in the y-axis another jump happens in the residual signal curve at the time sample of 10000.

– Second scenario: In this scenario, a bus voltage (V_{BUS}) fault (50% drop from the nominal value) has occured along the z-axis in satellite #3 at the time sample of 5000, and it is followed by a low motor current (I_m) fault (50% drop from the nominal value) in the y-axis of satellite #3 at the time sample of 10000. Fig. 3.29 shows the residual signals that are generated along (a) z-axis of the satellite #3 and (b) y-axis of satellite #3 using the proposed formation flying FD system. This figure clearly shows that when a bus voltage fault occurs in z-axis of satellite #3, the residual signal generated in corresponding axis detects the fault immediately at time samples 5000. Also, the dynamic neural network along y-axis of satellite #3 can see the effect of fault in z-axis after a short time delay. When a motor current fault occurs in y-axis of satellite #3, another jump happens in output signal of satellite #3 at time samples 10000, and it still remains in faulty zone.

– Third scenario: In this scenario, first a low motor current (I_m) fault (10% drop of nominal value) is injected in the x-axis of the satellite #1 at the time sample of 5000, and then a 10% increase of nominal viscous friction (τ_v) fault has occured in the y-axis of satellite #1 at the time sample of

111
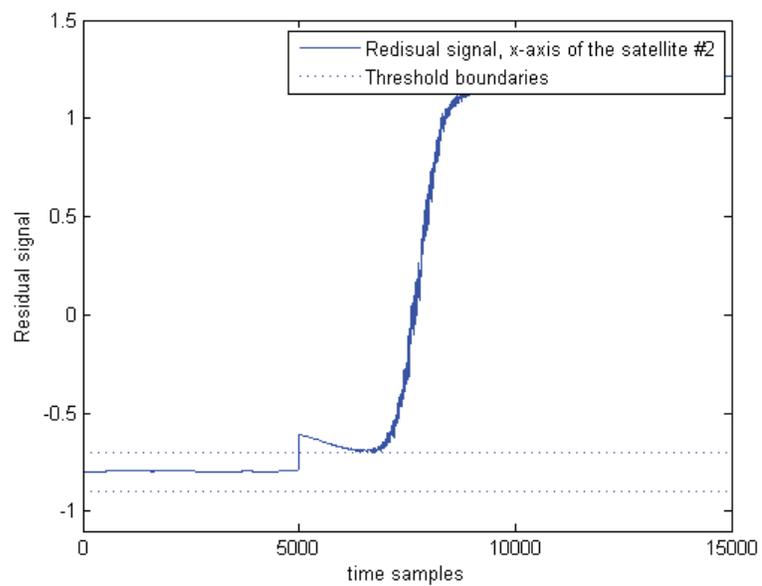
(a)
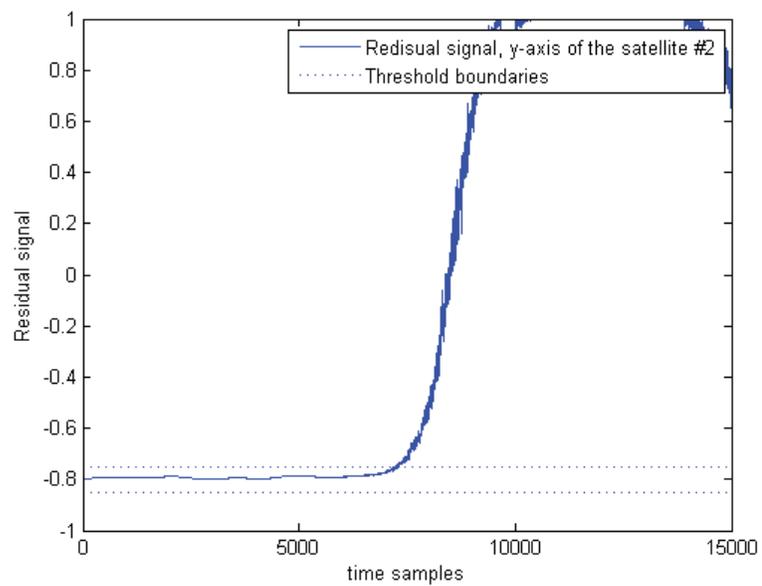
(b)

Figure 3.28: Residual signals corresponding to multiple fault scenario 1: (a) along the x-axis of satellite #2 (b) along the y-axis of satellite #2.
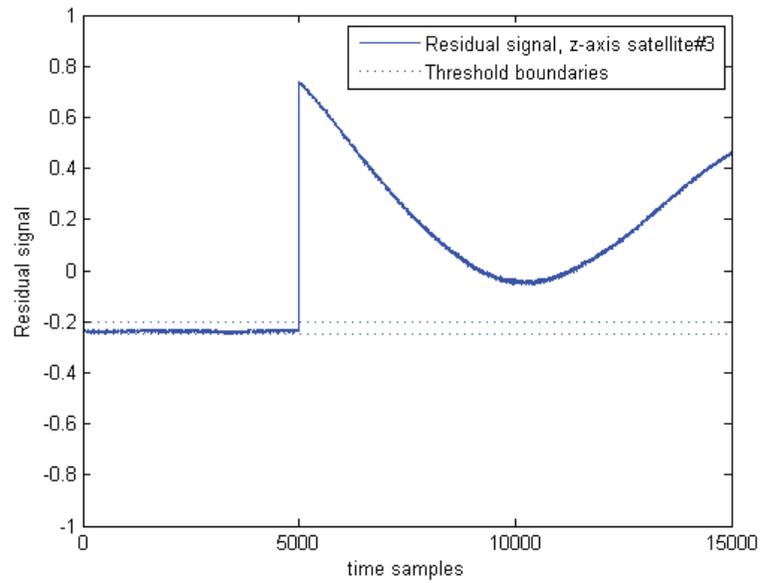
(a)
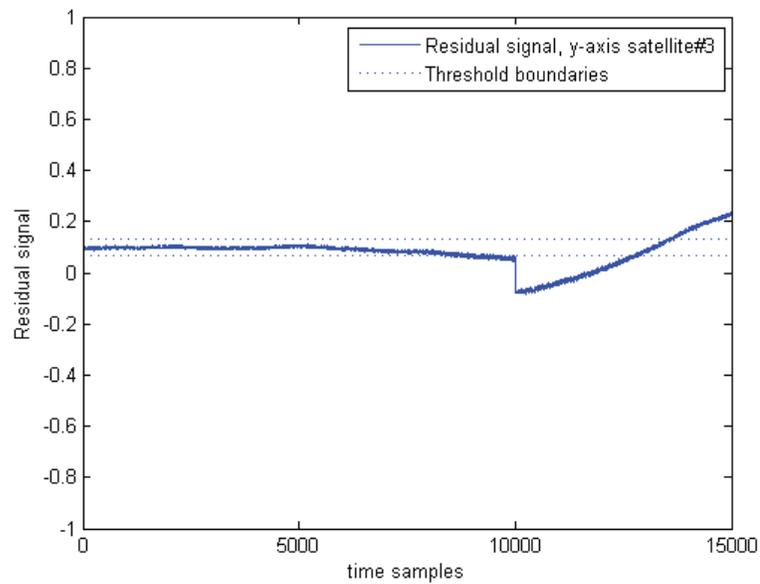
(b)

Figure 3.29: Residual signals corresponding to multiple fault scenario 2: (a) along the z-axis of satellite #3 (b) along the y-axis of satellite #3.

10000. The residual signals that are generated along (a) x-axis of the satellite #1 and (b) y-axis of satellite #1 using the proposed formation flying FD system are shown in Fig. 3.30. This figure shows that when the motor current fault occurs along the x-axis of satellite #1 it can be detected immediately using the corresponding DNN at time samples 5000. The DNN that is embedded along y-axis of satellite #1 can detect the motor current fault after a considerable time delay and when the temperature fault occurs in y-axis of satellite #1 at the time sample of 10000, a jump occurs in the residual error signal and the fault can be detected immediately.

- Multiple faults in two separate spacecraft

- Fourth scenario: In this scenario, a low motor current (I_m) fault (50% drop of nominal value) is injected in the y-axis of satellite #2 at the time sample of 5000, and it is followed by another low motor current (I_m) fault (50% drop of nominal value) that is injected in the z-axis of satellite #4 at the time sample of 10000. Fig. 3.31 shows the residual signals that are generated along (a) the y-axis of the satellite #2 and (b) the z-axis of satellite #4 using the proposed formation flying FD system. This figure shows that the fault occurrence along y-axis of satellite #2 can be detected without a significant time delay using the corresponding DNN at the time sample of 5000. The DNN along the z-axis of satellite #4 can detect the motor current fault after a time delay and when the next motor current fault occurs in the z-axis of satellite #4 at the time sample of 10000, a jump occurs in the residual error signal and the fault is detected immediately.

- Fifth scenario: In this scenario, a low bus voltage (V_{BUS}) fault (50% drop of nominal value) occurs in the y-axis of satellite #1 at the time sample of 5000,
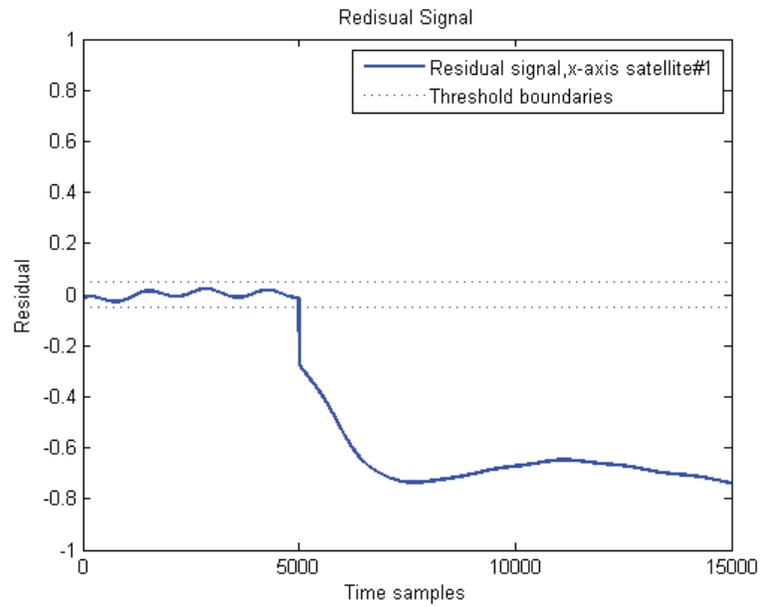
(a)
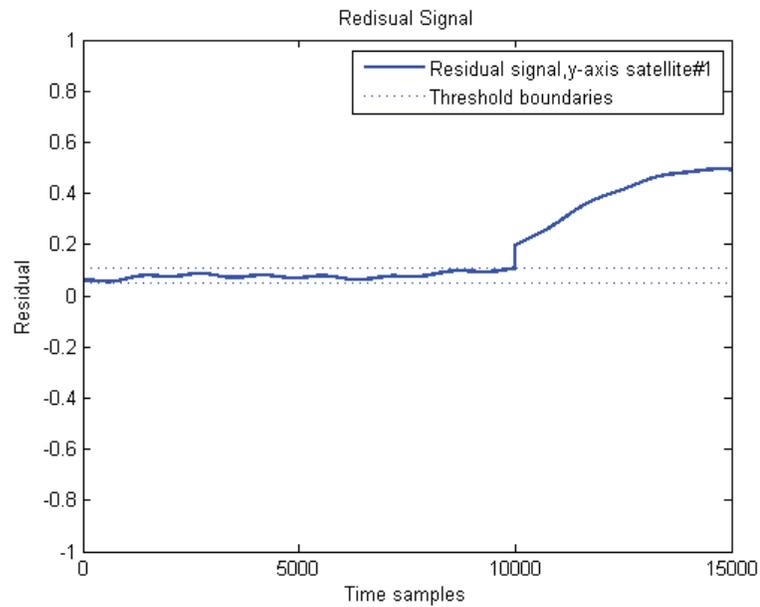
(b)

Figure 3.30: Residual signals corresponding to multiple fault scenario 3: (a) along the x-axis of satellite #1 (b) along the y-axis of satellite #1.
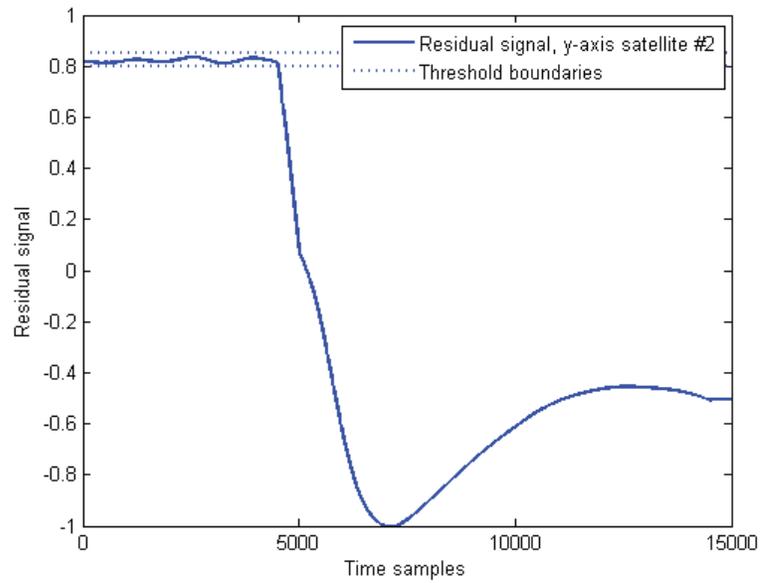
(a)
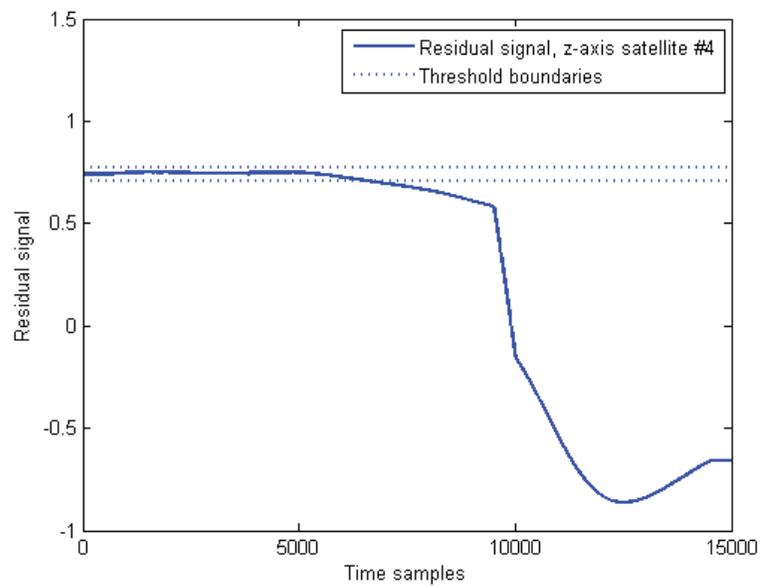
(b)

Figure 3.31: Residual signals corresponding to multiple fault scenario 4: (a) along the y-axis of satellite #2 (b) along the z-axis of satellite #4.

and then at the time sample of 10000 a low motor current (I_m) fault (50% drop from the nominal value) has occured in the z-axis of satellite #3. The residual signals that are generated using the proposed formation flying FD system along (a) the y-axis of the satellite #1 and (b) the z-axis of satellite #3 are shown in Fig. 3.32. This figure shows that when a bus voltage fault happens in the y-axis of satellite #1, the corresponding DNN along the y-axis of satellite #1 can detect the fault immediately at the time sample of 5000. When the motor current fault occurs in the z-axis of satellite #3, the residual signal in the y-axis of satellite #1 still remains faulty. The DNN in the z-axis of satellite #3 detects the bus voltage fault in satellite #1 after a time delay and when the second fault happens in the z-axis of satellite #3 at time samples 10000, a jump happens in the residual error signal and the error signal still remains in the faulty zone.

- Sixth scenario: In this case, a low bus voltage (V_{BUS}) fault (45% drop of nominal value) is injected in the y-axis of satellite #4 at the time sample of 5000, and then it is followed by another bus voltage (V_{BUS}) fault (50% drop of nominal value) in the z-axis of satellite #2 at the time sample of 10000. Fig. 3.33 shows the residual signals that are generated along (a) the y-axis of the satellite #4 and (b) the z-axis of satellite #2 using the proposed formation flying fault detection system. Using the proposed method, a bus voltage fault in the y-axis of the satellite #4, can be detected by using the corresponding DNN along the y-axis of satellite #4 at time samples 5000 (without time delay). When the next bus voltage fault occurs in the z-axis of satellite #2, the residual signal in the y-axis of satellite #4 still remains faulty. The DNN in the z-axis of satellite #2 detects the bus voltage fault in satellite #4 after a time delay and when the second fault happens in the z-axis of satellite #2 at the time sample of 10000, a jump occurs in the residual error signal and this signal still exceeds

117
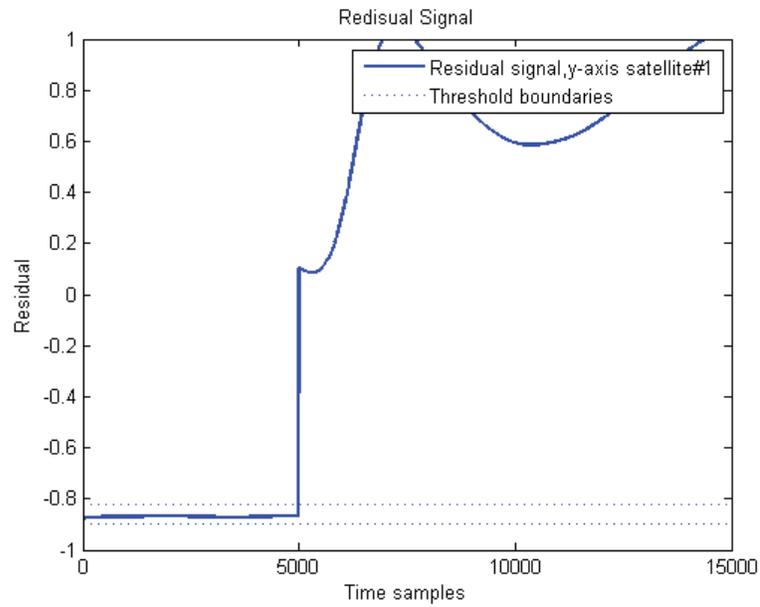
(a)
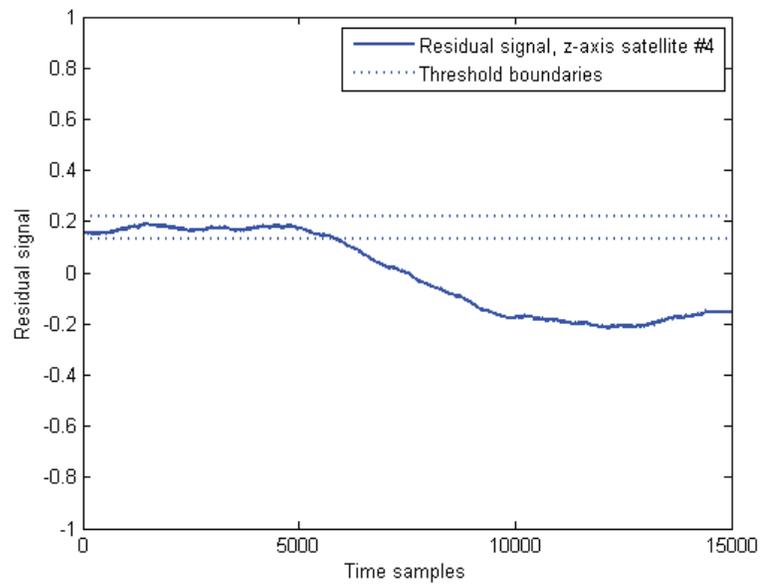
(b)

Figure 3.32: Residual signals corresponding to multiple fault scenario 5: (a) along the y-axis of satellite #1 (b) along the z-axis of satellite #4.

the threshold boundaries and indicates the faulty situation.

3.11 Fault Detection in Case of Low Severity Faults

Another motivation for developing the formation flying FD system is that it has the capability of detecting low severity faults when the local FD systems can not accomplish this goal. In order to evaluate capability of the proposed formation flying DNN-based scheme in detecting low severity faults, various faulty scenarios are considered and the capability of the formation flying FD system in detecting low severity faults is compared with the single satellite FD system that is previously developed in [43].

- First scenario: In this case, a bus voltage fault (45% drop from the nominal value) is injected in the z-axis of satellite #2 at the time sample of 10000. Fig. 3.34 shows the residual signals that are generated along the z-axis of satellite #2 using (a) formation flying FD system, and (b) single satellite FD system. This figure clearly shows that the proposed formation flying dynamic neural network along the z-axis of satellite #2 can detect the fault immediately, while the single satellite DNN along the z-axis of satellite #2 fails to detect the fault.

- Second scenario: In this case, a low motor current (5% drop from the nominal value) fault has occured in the y-axis of satellite #3 at the time sample of 10000. The residual signals that are generated along the y-axis of satellite #3 using (a) formation flying FD system, and (b) single satellite FD system are shown in Fig. 3.35. This figure clearly shows that by using the proposed DNN-based fault detection scheme,the fault occurrence along the y-axis of satellite

119
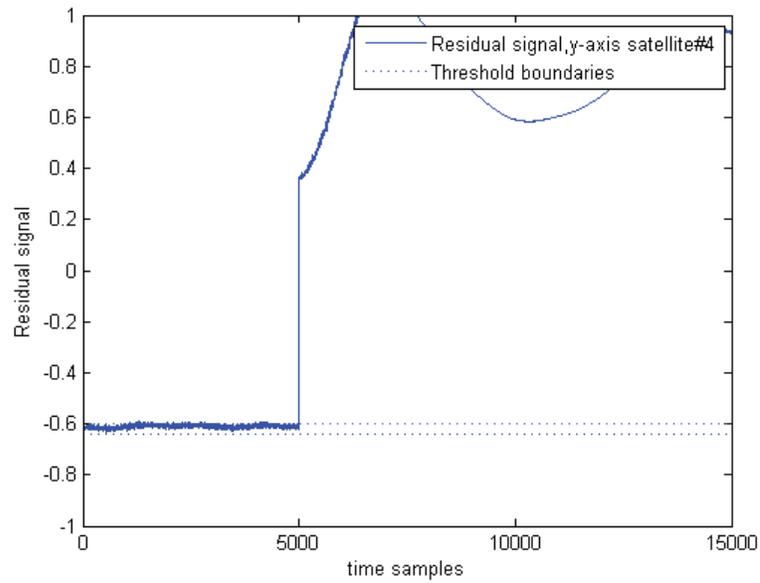
(a)
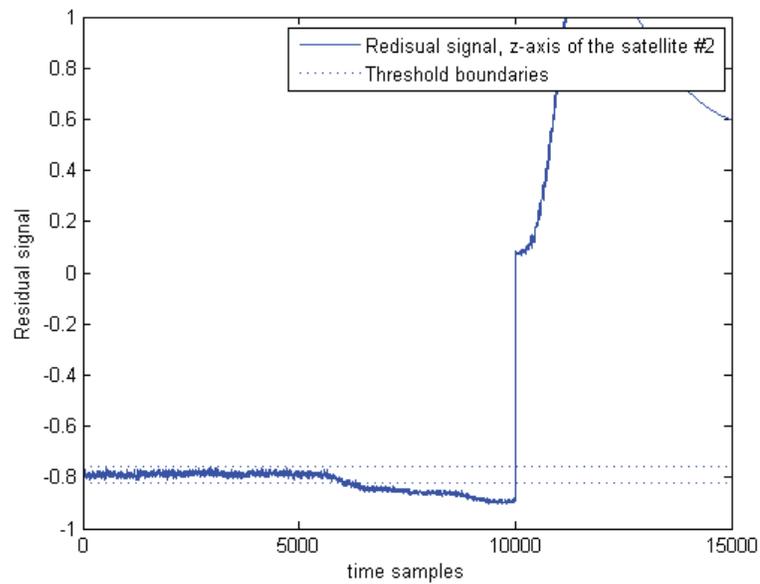
(b)

Figure 3.33: Residual signals corresponding to multiple fault scenario 6: (a) along the y-axis of satellite #4 (b) along the z-axis of satellite #2.
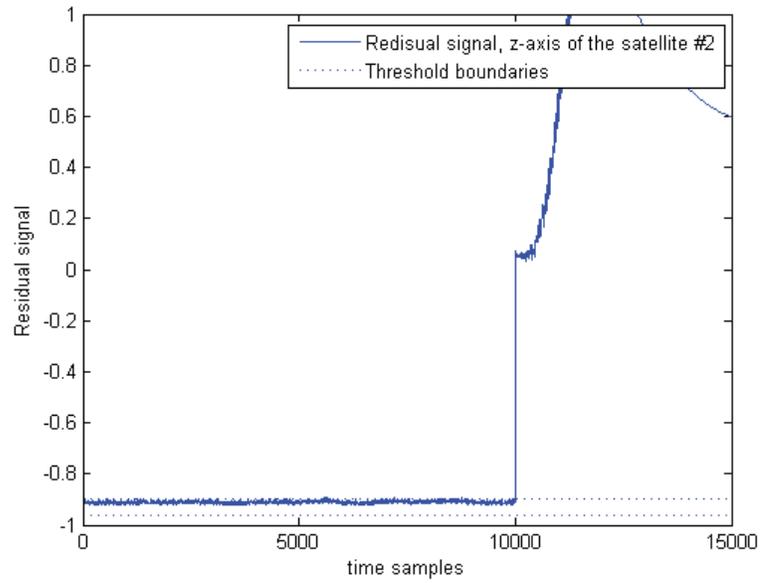
(a)
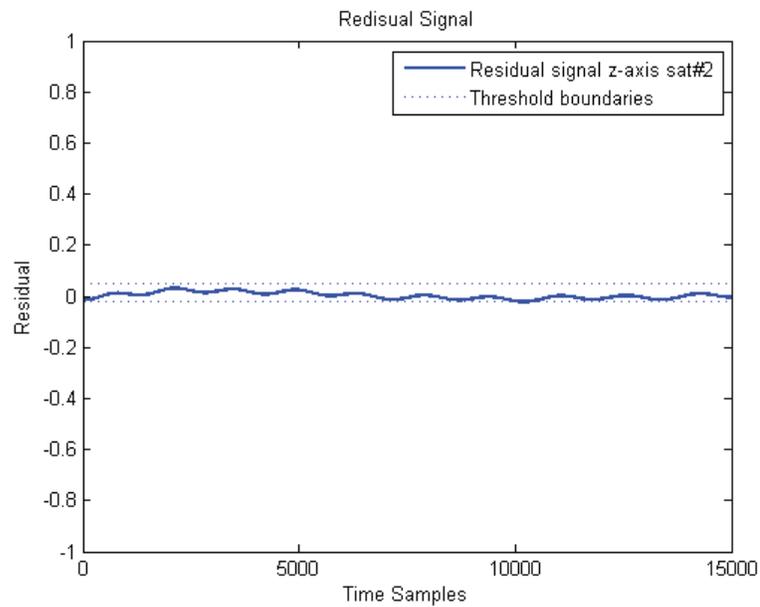
(b)

Figure 3.34: Residual error signals corresponding to low severity faults along the z-axis of satellite #2, scenario 1: (a) formation flying (b) single satellite.

Table 3.16: Comparison between single satellite and formation flying FD systems.

	Single satellite FD system	Formation flying FD system
Bus Voltage Fault	$\geq 50\%$ drop from the nominal value	$\geq 45\%$ drop from the nominal value
Motor Current Fault	$\geq 50\%$ drop from the nominal value	$\geq 5\%$ drop from the nominal value
Viscous Friction Fault	$\geq 50\%$ drop from the nominal value	$\geq 5\%$ drop from the nominal value

#3 can be detected immediately, while the local DNN in the y-axis of satellite #3 cannot detect the fault.

- Third scenario: In this scenario, a temperature fault that results in a 5% increase in viscous friction of the reaction wheel is injected in the x-axis of satellite #1 at the time sample of 10000. Fig. 3.36 shows the residual signals that are generated along the y-axis of satellite #3 using (a) formation flying FD system, and (b) single satellite FD system. This figure clearly shows that the proposed formation flying dynamic neural network along the y-axis of satellite #3 can detect the fault without a significant time delay, while the single satellite DNN along the y-axis of satellite #3 fails to detect the fault occurence.

The second advantage of the formation flying FD system that is proposed in this thesis, compared to the single satellite FD system approach that is proposed in [43] is its ability to detect low severity faults. Using this scheme, bus voltage faults greater than 45% drop from the nominal values and temperature and motor current faults greater than 5% drop from the nominal values can be detected. A qualitative comparison between the single satellite and the formation flying DNN-based fault detection systems is provided in Table 3.16.
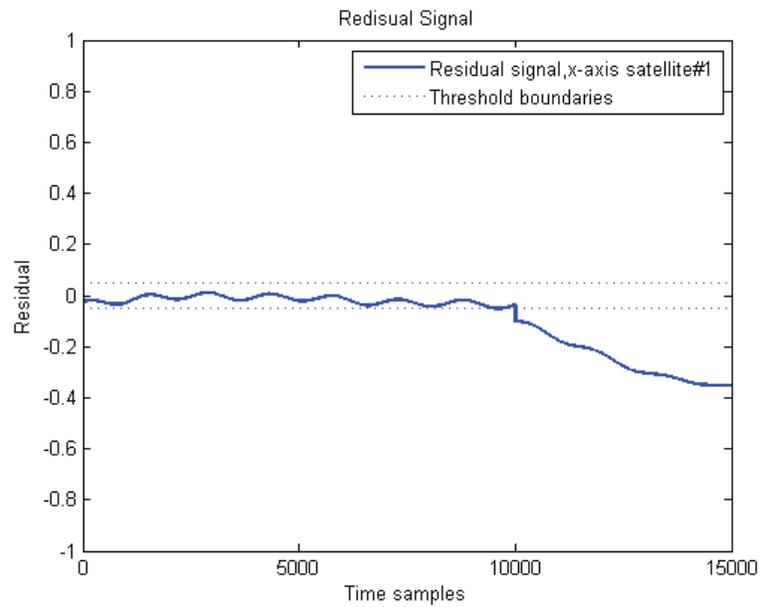
(a)
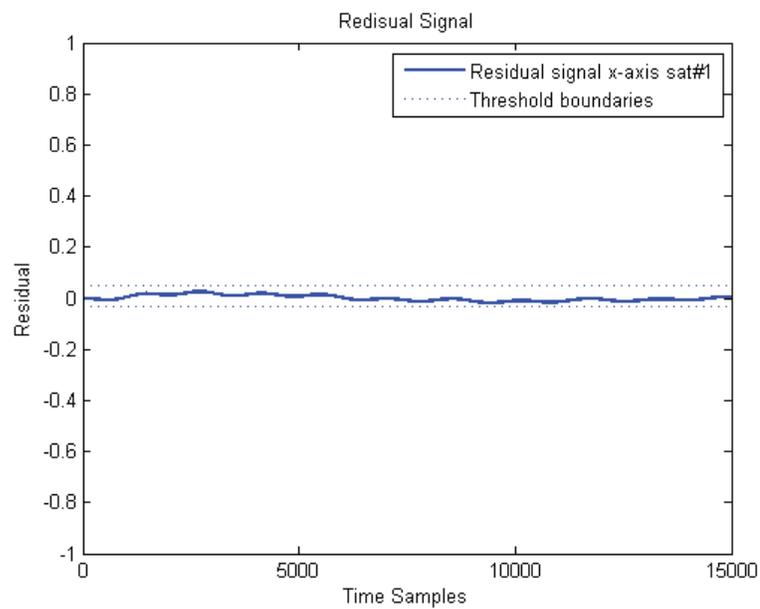
(b)

Figure 3.35: Residual error signals corresponding to low severity faults along the y-axis of satellite #3, scenario 2: (a) formation flying (b) single satellite.
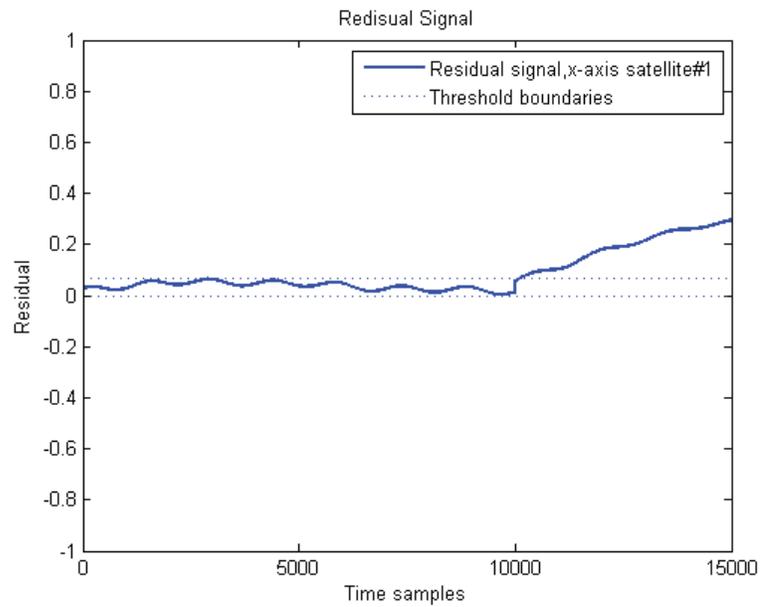
(a)
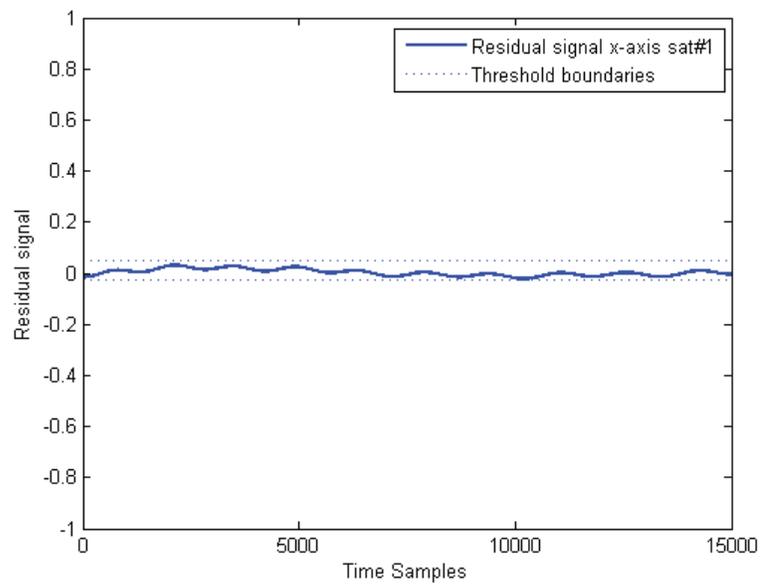
(b)

Figure 3.36: Residual error signals corresponding to low severity faults along the x-axis of satellite #1, scenario 3: (a) formation flying (b) single satellite.

3.12 FD System for a Formation of Satellites - Second Scheme

In the second scheme, a consensus-based virtual structure controlled formation flight having bi-directional ring topology is considered. In this architecture each satellite receives information from its two adjacent neighbors. The formation flying dynamic neural network-based FD system is trained based on sets of input/output data that are collected from the relative attitude determination sensors of the 3-axis attitude control subsystem of the satellites. In this scheme, $u = [q_1^{i+1/i}, q_2^{i+1/i}, q_3^{i+1/i}, q_1^{i/i-1}, q_2^{i/i-1}, q_3^{i/i-1},$ $V_{command}^i]^T$ is used as input vector for training the dynamic neural network and $y = [\tau_{reaction}^i]$ is used as the output vector for the training phase in which $q_1^{i+1/i}, q_2^{i+1/i},$and $q_3^{i+1/i}$ denote the relative attitude of satellite #i with respect to the satellite #$(i+1)$ and $q_1^{i/i-1}, q_2^{i/i-1},$and $q_3^{i/i-1}$ are the relative attitude of satellite #i with respect to satellite #$(i-1)$ and $V_{command}^i$ denotes the commanded voltage of satellite #i and $\tau_{reaction}^i$ denotes the reaction torque of satellite #i.

Fig. 3.37 shows the bi-directional connection links among four satellites in the formation flight scenario and Fig. 3.38 shows the proposed formation flying FD scheme.

3.13 Training Phase

Similar to the previous scheme, the DNNs in this scheme are trained by using an extended dynamic back-propagation method. The training phase is carried out for 50000 time samples and each time sample is equal to 0.01 sec. The input/output data set is normalized into the range of [-1,+1]. Table 3.17 shows the network parameters for which the best network performance is obtained. In this table n is the number of hidden layers, N_1 is the number of neurons in the first hidden layer and η is the
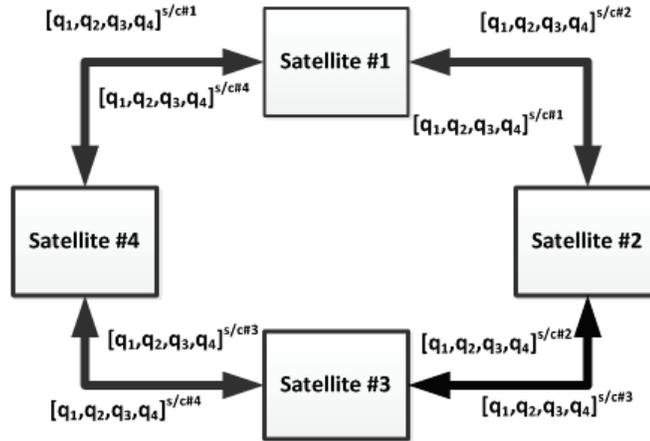
Figure 3.37: Communication links among the spacecraft in the formation - second scheme.

learning rate. The dynamic neural networks are trained until a termination criterion is satisfied. In this section, the termination criterion is the mean squared error (mse) criterion. Similar to the first scheme, in this approach, the adaption laws are based on the steepest descent gradient method and extended back-propagation learning law. The network parameters are updated so that the norm of the identification error is minimized where the identification error is defined as:

$$E(t) = \frac{1}{2} \sum_{k=1}^{K} (y_k(t) - y_k^{desired}(t))^2 \tag{3.11}$$

The training process is accomplished by using the Monte Carlo simulations under different noisy situations for 50000 time samples and each time sample is 0.001 sec. The network is trained for 100 different pairs of input/output data in presence of a normally distributed noise with zero mean and standard deviation of 0.01 differences between the maximum and the minimum values in the input/output data intervals. The performance of network during the training phase along the x-axis of the four satellites is shown in Fig. 3.39. The average value of the mean square error in 100 training simulations is 0.046 and its standard deviation is 0.0006, which is quite

126
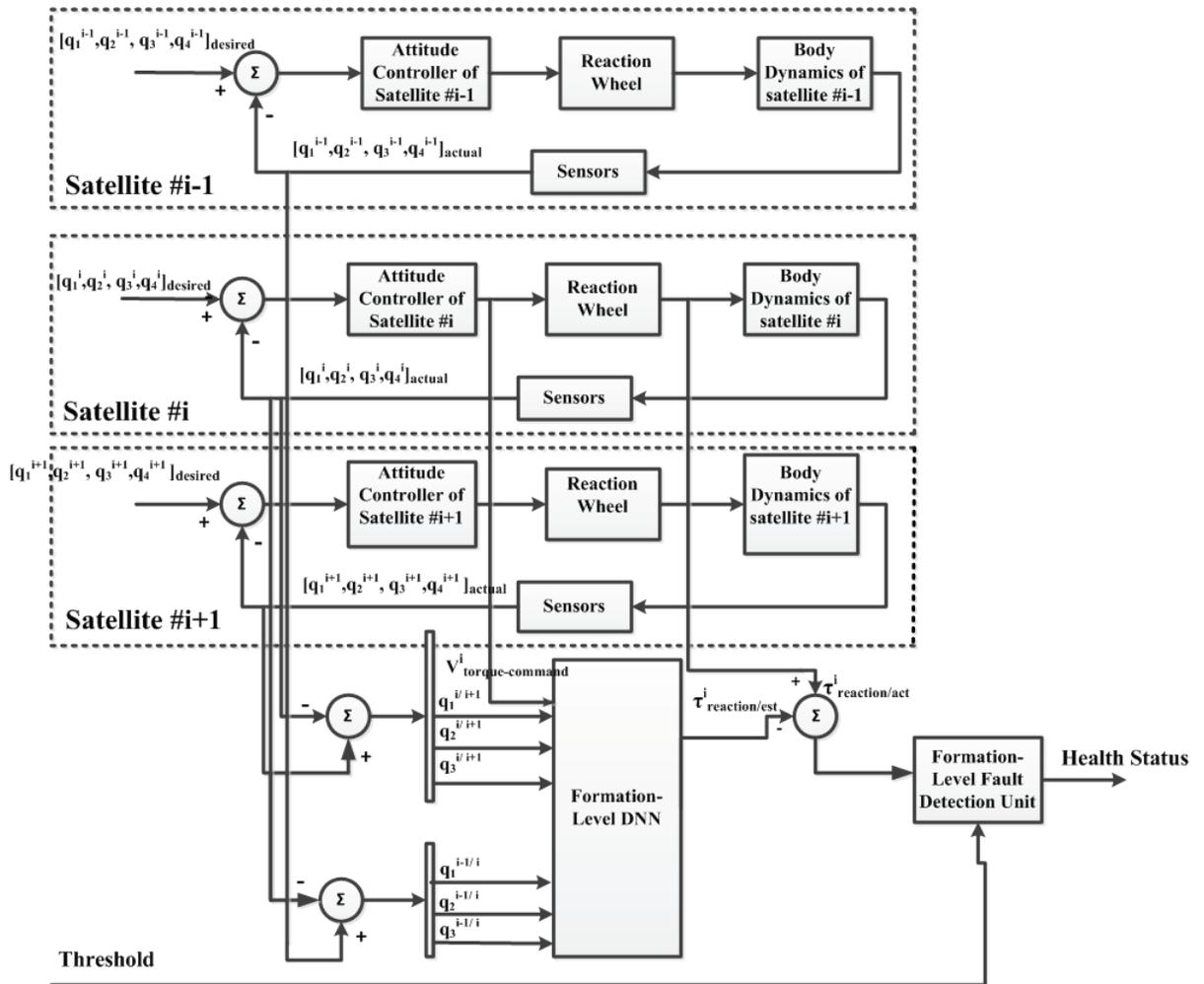
Figure 3.38: Structure of the FD system in a formation flying of satellites - second scheme.

Table 3.17: DNN characteristics in the learning phase.

Spacecraft #	Network Size	Number of Iterations	Performance Index	Learning Rate Rate
1	N_{1-5-1}	50000	0.047	0.01
2	N_{1-5-1}	50000	0.062	0.02
3	N_{1-6-1}	50000	0.0547	0.01
4	N_{1-6-1}	50000	0.0483	0.01

acceptable. The mean square error (mse) for other axes of other satellites can be obtained in a similar way.

3.14 Testing Phase

In order to evaluate the capability of the trained DNNs in representing dynamic model of the reaction wheels of a spacecraft, the output of the neural network is obtained for another healthy input data set and it is compared with the actual output of the system. Fig. 3.40 shows the estimated output and the actual output of the system in the testing phase for the three axes of the satellite #1 in the formation. This figure shows that the output of the trained dynamic neural network can follow the actual output of the system. The testing step is accomplished for 100 different pairs of input/output data in presence of a normally distributed noise with zero mean and standard deviation of 0.01 differences between the maximum and the minimum values in the input/output data intervals. The average value of mean square error in 100 testing samples is 0.078 and its standard deviation is 0.0009, which is quite acceptable.
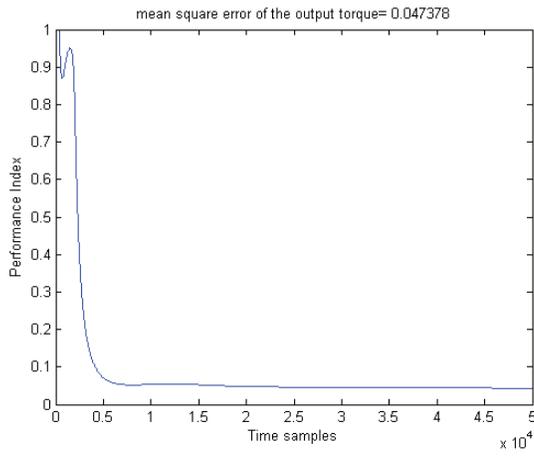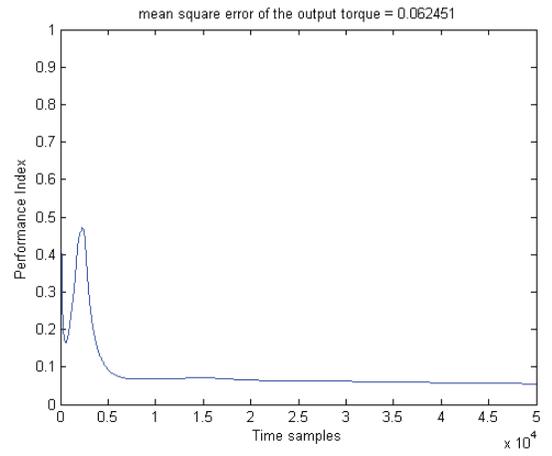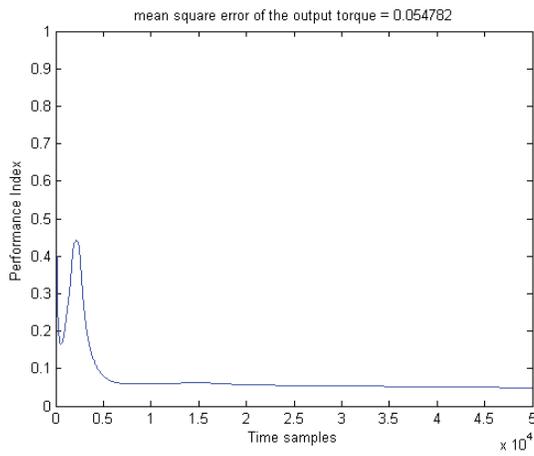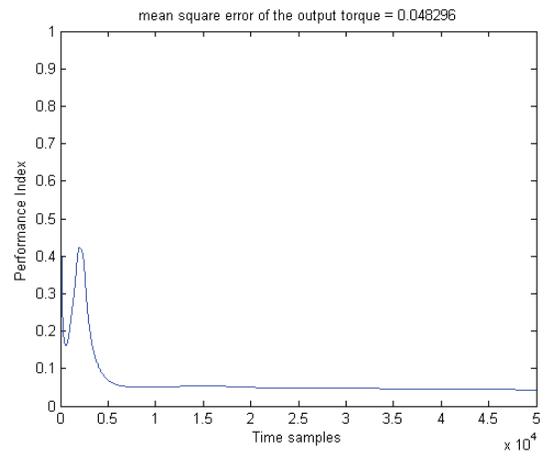
Figure 3.39: The performance index (mean squared error of the output reaction torque) curve for the dynamic neural network- x-axis of (a) satellite #1, (b) satellite #2 (c) satellite #3 (d) satellite #4.
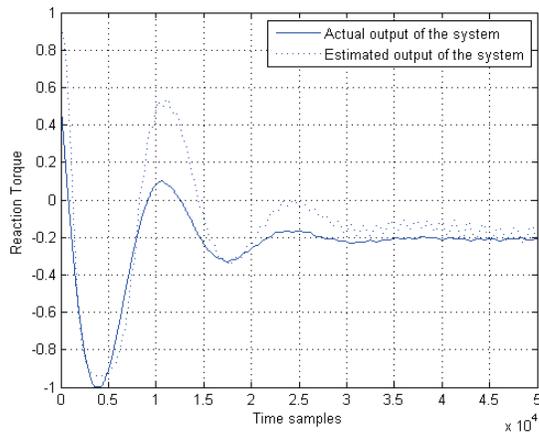
(a)
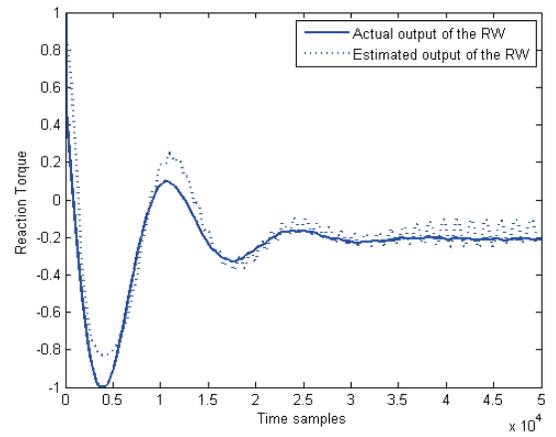
(b)
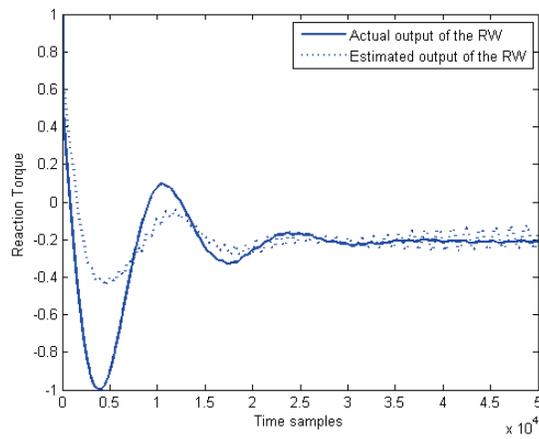
(c)

Figure 3.40: Testing curve (actual and estimated outputs) for the DNN (second approach) - (a) x-axis, (b) y-axis, (c) z-axis of satellite #1.

3.15   Actuator Fault Scenarios

In order to evaluate the representation characteristics of the proposed DNN-based method FD scheme, several fault scenarios are considered as described below.

- Bus voltage (V_{BUS}) fault

  - First scenario: In this scenario, a low bus voltage (60% drop from the nominal value) fault is injected in the x-axis of satellite #4 at the time sample of 5000. Fig. 3.41 shows the residual signal generated in local fault diagnosis DNN and in the corresponding DNNs in its two adjacent neighbors.

  - Second scenario: In the second scenario, a low bus voltage (45% drop from the nominal value) fault has occurred in the z-axis of satellite #2 at the time sample of 10000. The residual error signals generated in the z-axis of satellite #2 and the corresponding axes of its two adjacent satellites are shown in Fig. 3.42.

- Motor Current (I_m) Fault

  - Third scenario: In this case, a low motor current (15% drop of nominal value) fault is injected at the y-axis of satellite #3 at the time sample of 10000. The residual error signals on the y-axis network of satellites #3, #2 and #4 are shown in Fig. 3.43.

  - Forth scenario: In this scenario, a low motor current (60% drop from the nominal value) fault is injected in the x-axis of satellite #1 at the time sample of 5000. Fig. 3.44 shows the residual error signals that are generated in the x-axis of satellite #1, #2 and #4. In this case, when the current fault occurs at the time sample of 5000, the residual error
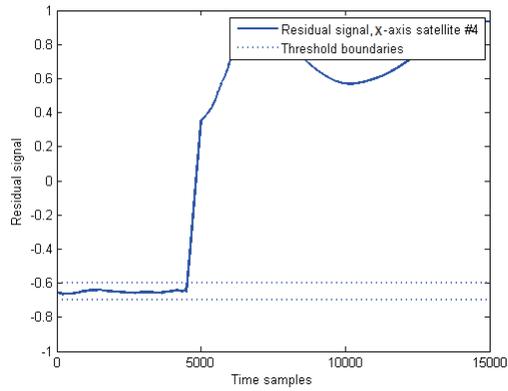
(a)
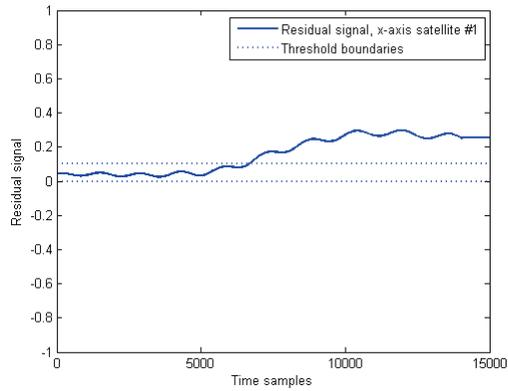
(b)
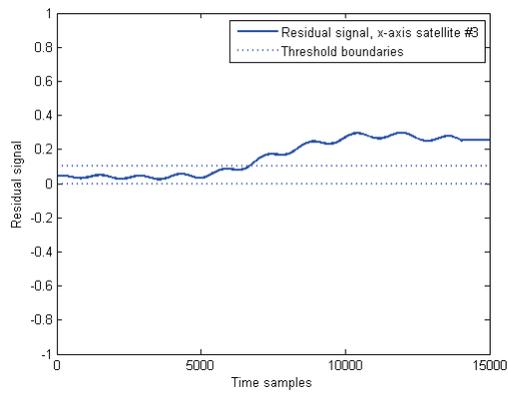
(c)

Figure 3.41: Residual signals corresponding to bus voltage fault - scenario 1: (a) x-axis of satellite #4, (b) x-axis of satellite #1, (c) x-axis of satellite #3.
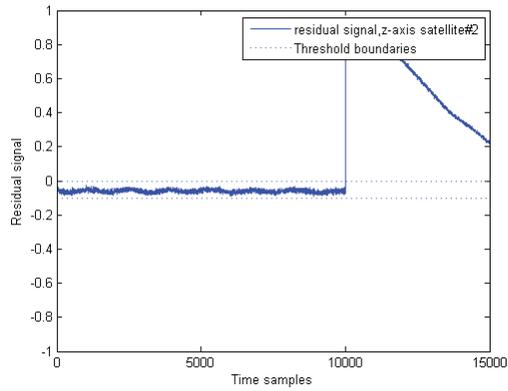
(a)
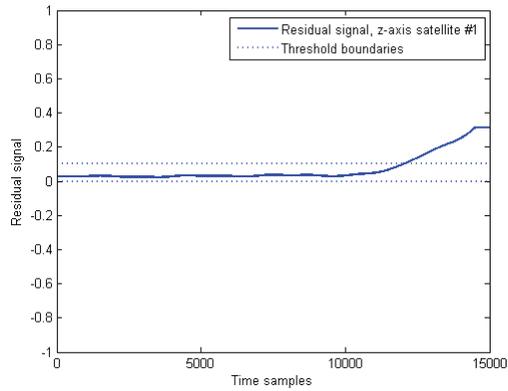
(b)
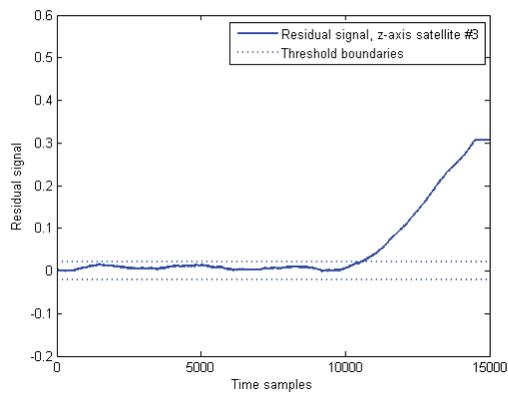
(c)

Figure 3.42: Residual signals corresponding to bus voltage fault - scenario 2: (a) z-axis of satellite #2, (b) z-axis of satellite #1, (c) z-axis of satellite #3.
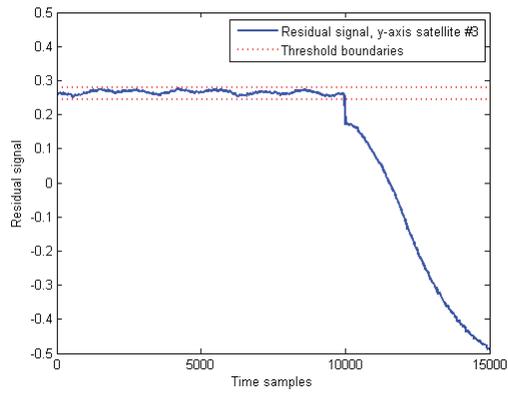
(a)
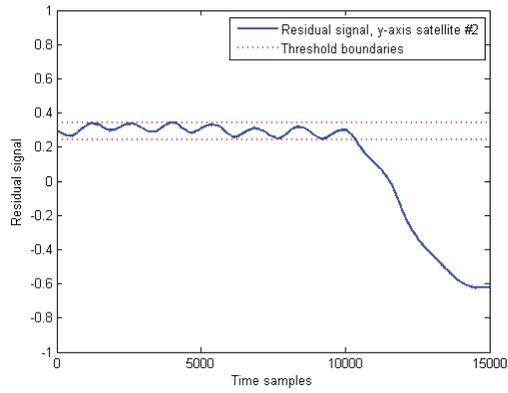
(b)
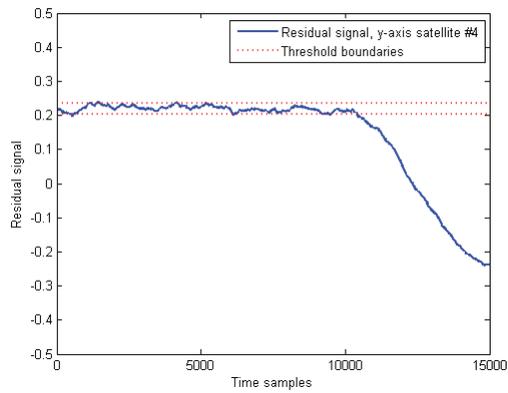
(c)

Figure 3.43: Residual signals corresponding to motor current fault - scenario 3: (a) y-axis of satellite #3, (b) y-axis of satellite #2, (c) y-axis of satellite #4.

signal generated in the x-axis of satellite #1 detects the fault immediately and the residual error signal exceeds the threshold at the time sample of 5000. In this case a misclassification has occured at the time sample of 9000. Although the system is still faulty, the residual error crosses the healthy zone at the time sample of 9000 for a short period of time. In Section 3.16 these residual error are classified as "Actual faulty/Predicted Healthy" signals.

- Viscous Temperature (τ_v) Fault

  – Fifth scenario: In this case, a high viscous temperature (50% increase from the nominal value) fault is injected at the x-axis of satellite #2 at the time sample of 5000. The residual error signals on the x-axis dynamic neural network of satellite #2, #3 and #1 are shown in Fig. 3.45.

  – Sixth scenario: In this case a high temperature fault that results in a 10% increase from the nominal value of viscous friction has occured at the x-axis of satellite #1 at the time sample of 10000. The residual error signals on the x-axis networks of satellites #1, #2 and #4 are shown in Fig. 3.46. In this case a misclassification has occured at the time sample of 11500. Although the system is still faulty, the residual error signal crosses the healthy zone at the time sample of 11500 for a short period of time. In Section 3.16 these residual error signals are classified as "Actual faulty/Predicted Healthy" signals.

Figs. 3.41 to 3.46 show that once a fault occurs in a reaction wheel of one of the satellites in the formation, it can be detected by using local DNN immediately. DNNs in the corresponding axes of the two adjacent neighbors of the faulty spacecraft can also detect the fault after a short time delay.
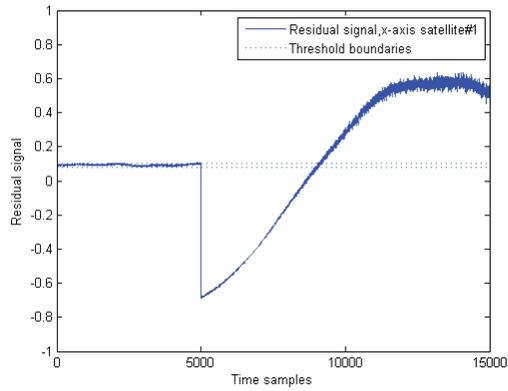
(a)
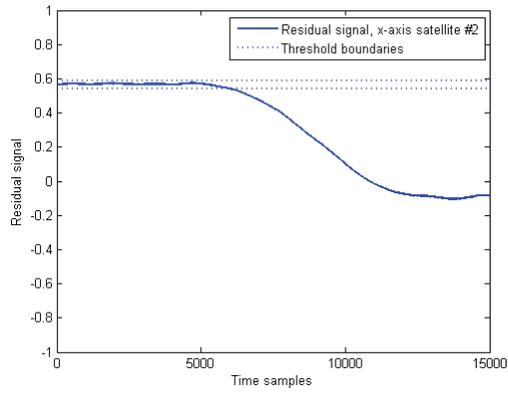
(b)
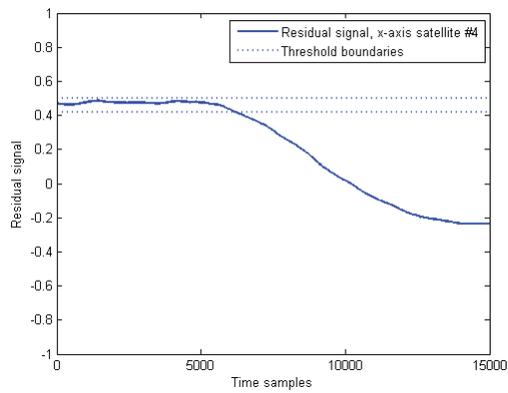
(c)

Figure 3.44: Residual signals corresponding to motor current fault - scenario 4: (a) x-axis of satellite #1, (b) x-axis of satellite #2, (c) x-axis of satellite #4.

(a)

(b)
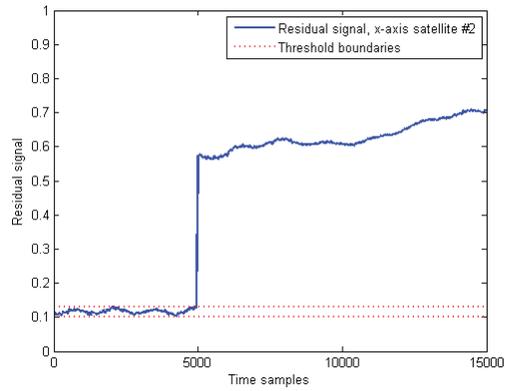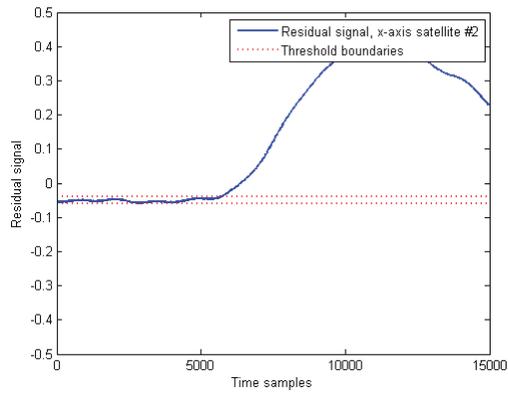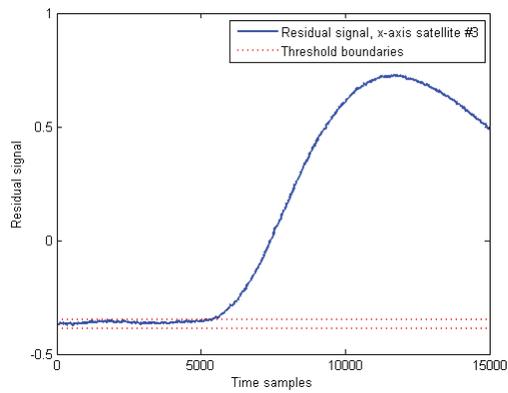
Figure 3.45: Residual signals corresponding to temperature fault - scenario 5: (a) x-axis of satellite #2, (b) x-axis of satellite #1, (c) x-axis of satellite #3.
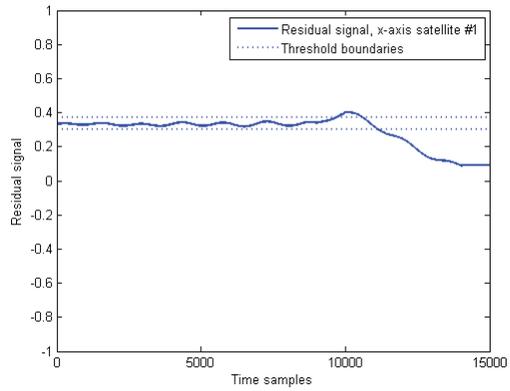
(a)
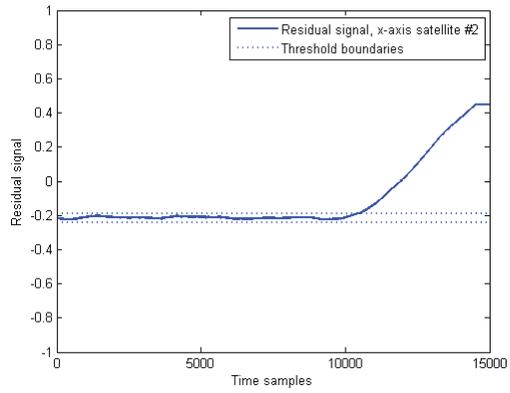
(b)
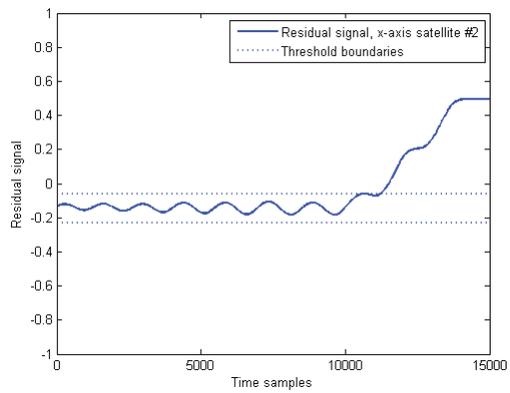
(c)

Figure 3.46: Residual signals corresponding to temperature fault - scenario 6: (a) x-axis of satellite #1, (b) x-axis of satellite #4, (c) x-axis of satellite #2.

In this scheme, once a fault occurs in satellite $\#i$, it can be detected by local diagnoser immediately. However, since there are communication links between each satellite and its two nearest neighbors, the DNN based FD systems that are embedded in two adjacent nearest neighbors of satellite $\#i$ (i.e. satellite $\#(i-1)$ and satellite $\#(i+1)$) can detect the fault occurrence after a short time delay too. However, depending on the fault severity, the second nearest neighbors of satellite $\#i$ might be able to detect the fault after longer time delays. Similar to the first scheme, in this scheme the bus voltage faults greater than 45% drop from the nominal value, motor current faults greater than 5% drop from the nominal value and viscous temperature faults greater than 5% drop from the nominal value can be detected successfully.

In order to provide a quantitative study on fault detection time delays, different fault scenarios are considered. Table 3.18 shows the fault detection times for the DNNs employed in the formation in case of a low bus voltage fault (60% drop from the nominal value) along the x-axis of satellite $\#1$. This table shows that the local diagnoser (DNN x-1) can detect the fault immediately, while the DNNs in adjacent neighbors can detect the fault after a short time delay.

In the second case, a low motor current fault (50% drop from the nominal value) is injected in the reaction wheel of the x-axis of satellite $\#2$. Table 3.19 shows the fault detection times for the DNNs embedded in different axes of spacecraft in the formation. In this case fault is injected in the x-axis of satellite $\#2$, so the corresponding DNN in the x-axis of satellite $\#2$ can detect the fault immediately, and the DNNs in adjacent satellites can detect the fault after a time delay. Table 3.20 shows the fault detection times for a 10% increase in the nominal value of viscous friction fault in the y-axis of satellite $\#3$. In this case the DNN along the y-axis of satellite $\#3$ detects the fault without a significant time delay and the other DNNs detect the fault after a time delay. In the fourth scenario, a high temperature fault

Table 3.18: Fault detection time delays in case of 60% drop of nominal value in the bus voltage of x-axis satellite #1.

Dynamic Neural Network #	Fault Detected	Detection Time Delay
DNN x-1	YES	0 sec
DNN y-1	YES	2 sec
DNN z-1	YES	1 sec
DNN x-2	YES	5 sec
DNN y-2	YES	5 sec
DNN z-2	YES	5 sec
DNN x-3	YES	1 sec
DNN y-3	YES	1 sec
DNN z-3	YES	1 sec
DNN x-4	YES	8 sec
DNN y-4	YES	6 sec
DNN z-4	YES	5 sec

Table 3.19: Fault detection time delays in case of 50% drop of nominal value in the bus voltage of x-axis satellite #2.

Dynamic Neural Network #	Fault Detected	Detection Time Delay
DNN x-1	YES	2 sec
DNN y-1	YES	4 sec
DNN z-1	YES	5 sec
DNN x-2	YES	0 sec
DNN y-2	YES	8 sec
DNN z-2	YES	5 sec
DNN x-3	YES	5 sec
DNN y-3	YES	5 sec
DNN z-3	YES	6 sec
DNN x-4	YES	15 sec
DNN y-4	YES	14 sec
DNN z-4	YES	15 sec

Table 3.20: Fault detection time delays in case of 10% increase in nominal value of the viscous friction of y-axis satellite #3.

Dynamic Neural Network #	Fault Detected	Detection Time Delay
DNN x-1	YES	20 sec
DNN y-1	YES	15 sec
DNN z-1	YES	18 sec
DNN x-2	YES	11 sec
DNN y-2	YES	8 sec
DNN z-2	YES	10 sec
DNN x-3	YES	5 sec
DNN y-3	YES	0 sec
DNN z-3	YES	5 sec
DNN x-4	YES	12 sec
DNN y-4	YES	14 sec
DNN z-4	YES	12 sec

that results in a 50% increase from the nominal value of viscous friction is injected in the reaction wheel of the y-axis of satellite #3. Table 3.21 shows the fault detection times in the DNNs that are embedded in different axes of spacecraft in the formation. In this case fault is injected in the y-axis of satellite #3, so the corresponding DNN in the y-axis of satellite #3 can detect the fault immediately, and the DNNs in the neighboring satellites can detect the fault after a time delay.

A comparative study of Tables 3.12- 3.15 (i.e. fault detection times using the first fault detection scheme) and Tables 3.18- 3.21 (i.e. fault detection times using the second fault detection scheme) shows that in the second fault detection scheme, the neighboring spacecraft can detect the fault earlier than the neighboring satellite in the first scheme. That is due to the fact that the DNNs in the second scheme are trained based on the attitude information obtained from two adjacent neighbors of the faulty spacecraft and they can provide better estimate of the output of the system.

Table 3.21: Fault detection time delays in case of 50% increase in nominal value of the viscous friction of y-axis satellite #3.

Dynamic Neural Network #	Fault Detected	Detection Time Delay
DNN x-1	YES	10 sec
DNN y-1	YES	9 sec
DNN z-1	YES	9 sec
DNN x-2	YES	6 sec
DNN y-2	YES	5 sec
DNN z-2	YES	6 sec
DNN x-3	YES	5 sec
DNN y-3	YES	0 sec
DNN z-3	YES	5 sec
DNN x-4	YES	10 sec
DNN y-4	YES	8 sec
DNN z-4	YES	10 sec

Table 3.22: Actual and detection results in case of 45% drop from the nominal value of the bus voltage (V_{BUS}) along the z-axis of satellite #2 by using 10000 time samples.

DNN #	Actual Healthy	Actual Faulty	Estimated Healthy	Estimated Faulty
DNN z-2	5000 samples	5000 samples	4590 samples	5410 samples
DNN z-1	5000 samples	5000 samples	6400 samples	3600 samples

3.16 Confusion Matrix Analysis for Formation Flying FD Method

3.16.1 Confusion Matrix - Formation Flying FD - First Scheme

In order to investigate the capability of the fault detection (FD) system in formation flying various faulty scenarios have been considered. In the first scenario, a 45% drop from the nominal value of bus voltage (V_{BUS}) along the z-axis of the satellite #2 is considered. Table 3.22 shows the actual healthy and the actual faulty output signals and the classification that is obtained by using the FD scheme. In this case, the reaction wheel is operating under a healthy area of operation for 5000 steps and then a bus voltage fault occurs and reaction wheel operates in the faulty area of operation

Table 3.23: Actual and detection results in case of 50% drop from the nominal value of the motor current(I_m)) along the x-axis of satellite #3 by using 10000 time samples.

DNN #	Actual Healthy	Actual Faulty	Estimated Healthy	Estimated Faulty
DNN x-3	5000 samples	5000 samples	4820 samples	5180 samples
DNN x-2	5000 samples	5000 samples	5700 samples	4300 samples

Table 3.24: Actual and detection results in case of 50% drop from the nominal value of the viscous friction (τ_v) along the x-axis of satellite #1 by using 10000 time samples.

DNN #	Actual Healthy	Actual Faulty	Estimated Healthy	Estimated Faulty
DNN x-1	5000 samples	5000 samples	4630 samples	5370 samples
DNN x-4	5000 samples	5000 samples	6900 samples	3100 samples

for 5000 steps.

Using the proposed FD scheme, the DNN embedded along the z-axis of the satellite #2 estimates that the reaction wheel is working fault-free for 4590 steps and it works faulty for 5410 steps. The DNN embedded along the z-axis of the satellite #1 can also detect the effects of the fault. Using this dynamic neural network it is estimated that the satellite operates healthy for 6400 steps and it operates faulty for 3600 steps.

In the second faulty scenario, satellite works fault-free for 5000 time samples and then a motor current fault (50% drop from the nominal value of the motor current (I_m) along the x-axis of satellite #3) occurs and satellite works faulty for 5000 steps. Table 3.23 shows that by using the proposed formation flying FD scheme for the x-axis of satellite #3, it is estimated that the satellite works healthy for 4820 steps and it then operates under a faulty situation for 5180 steps. The dynamic neural network embedded along the x-axis of satellite #2 can detect the effects of the fault after a time delay. This DNN estimates that the satellite is in the healthy status for 5700 steps and it is in the faulty status for 4300 steps.

In the third scenario, the satellite operates in its fault-free operating zone for 5000 time samples and then a temperature fault (50% increase from the nominal

Table 3.25: Actual and detection results in case of 10% drop from the nominal value of the viscous friction (τ_v) along the y-axis of satellite #3 by using 10000 time samples.

DNN #	Actual Healthy	Actual Faulty	Estimated Healthy	Estimated Faulty
DNN y-3	5000 samples	5000 samples	4950 samples	5050 samples
DNN y-2	5000 samples	5000 samples	5830 samples	4170 samples

Table 3.26: Actual and detection results in case of 15% drop from the nominal value of the motor current(I_m) along the y-axis of satellite #3 by using 10000 time samples.

DNN #	Actual Healthy	Actual Faulty	Estimated Healthy	Estimated Faulty
DNN y-3	5000 samples	5000 samples	4940 samples	5060 samples
DNN y-2	5000 samples	5000 samples	6100 samples	4900 samples

value of viscous temperature (τ_v) along the x-axis of the satellite #1) occurs and the satellite starts operating in the faulty zone for 5000 steps. Table 3.24 shows that by using the proposed formation flying FD scheme in the x-axis of the satellite #1, it is estimated that the satellite is operating healthy for 4630 time samples and is working in the faulty zone for 5370 steps. The DNN embedded in the x-axis of the satellite #4 can detect the fault after a time delay as well. According to Table 3.24 this DNN estimates that the reaction wheel is healthy for 6900 steps and is then faulty for 3100 steps.

In the fourth scenario, the spacecraft is working in the healthy status for 5000 steps and then a 10% increase in nominal value of the viscous friction (τ_v) fault occurs along the y-axis of the satellite #3 and spacecraft works in this faulty situation for 5000 steps. The proposed formation flying FD system for the y-axis of the satellite #3 estimates that the spacecraft is healthy for 4950 steps and operates in the faulty zone for 5050 steps. The DNN embedded along the y-axis of satellite #2 is also capable of detecting the fault after a time delay. This DNN estimates that the satellite is operating healthy for 5830 steps and is operating faulty for 4170 steps. The analytical results for the fourth scenario are depicted in Table 3.25.

A 15% drop from the nominal value of motor current (I_m) fault along the y-axis

144

Table 3.27: Actual and detection results in case of 70% drop from the nominal value of the bus voltage (V_{BUS}) along the x-axis of satellite #2 by using 10000 time samples.

DNN #	Actual Healthy	Actual Faulty	Estimated Healthy	Estimated Faulty
DNN x-2	5000 samples	5000 samples	5000 samples	5000 samples
DNN x-1	5000 samples	5000 samples	6950 samples	3050 samples

of satellite #3 is considered in the fifth scenario. In this case, satellite operates in its healthy status for 5000 steps and then a fault occurs and satellite operates faulty for 5000 steps. Using the DNN in the y-axis of satellite #3 in the proposed FD scheme for the formation flying of spacecraft, it is estimated that the satellite is healthy for 4940 steps and it operates faulty for 5060 steps. The DNN embedded along the y-axis of satellite #2 can detect the fault after a short time delay as well. According to Table 3.26 this DNN estimates that the satellite is healthy for 6100 steps and it is operating faulty for 4900 steps.

In the sixth scenario, it is assumed that the spacecraft is working under the healthy status for 5000 steps and then a 70% drop from the nominal value of the bus voltage (V_{BUS}) fault is injected along the x-axis of the satellite #2 and spacecraft works in this faulty situation for 5000 steps. The proposed formation flying FD system along the x-axis of the satellite #2 estimates that the spacecraft is fault-free for 5000 steps and operates in the faulty zone for 5000 steps. The DNN embedded along the x-axis of the satellite #1 is also capable of detecting the fault after a time delay. This DNN estimates that the satellite is operating under the healthy zone for 6950 steps and is operating faulty for 3050 steps. The analytical results for the sixth scenario are depicted in Table 3.27.

Considering the above six faulty scenarios for the satellite #i the following values in Table 3.28 for the confusion matrix are obtained.

According to Table 3.29 the dynamic neural network embedded along the faulty

Table 3.28: Confusion matrix parameters for faulty satellite($\#i$) and its nearest neighbor($\#(i-1)$).

DNN #	A	B	C	D
DNN of satellite $\#i$	30000 samples	0 samples	1070 samples	28930 samples
DNN of satellite $\#(i-1)$	23000 samples	7000 samples	420 samples	29580 samples

Table 3.29: Confusion matrix results for faulty satellite($\#i$) and its nearest neighbor($\#(i-1)$).

	DNN of satellite $\#i$	DNN of satellite $\#(i-1)$
Accuracy	98%	87%
True healthy	96%	98%
False healthy	0%	23%
True faulthy	100%	76%
False faulty	4%	2%
Precision	100%	82%

axis of the satellite $\#i$ can classify 96% of healthy signals and 100% of faulty signals successfully; however 4% of healthy signals are misclassified as faulty using this method. The accuracy level (98%) and the precision level (100%) of this method are highly acceptable. The dynamic neural network embedded along the corresponding axis of satellite $\#(i-1)$ which is the nearest neighbor to satellite $\#i$ can classify 98% of the healthy signals and 76% of faulty signals correctly. The accuracy level (87%) and the precision (82%) are acceptable.

3.16.2 Confusion Matrix - Formation Flying FD - Second Scheme

In order to investigate the fault detection capabilities of the proposed FD system in formation flying, various faulty scenarios have been considered. In the first scenario, a bus voltage fault (45% drop from the nominal value) along the z-axis of the satellite #2 at the time sample of 5000 is considered. Table 3.30 shows the actual healthy and

Table 3.30: Actual and detection results in case of 45% drop from the nominal value of the bus voltage (V_{BUS}) along the z-axis of satellite #2 by using 10000 time samples.

DNN #	Actual Healthy	Actual Faulty	Estimated Healthy	Estimated Faulty
DNN z-2	5000 samples	5000 samples	5000 samples	5000 samples
DNN z-1	5000 samples	5000 samples	5570 samples	4430 samples
DNN z-3	5000 samples	5000 samples	3550 samples	3450 samples

Table 3.31: Actual and detection results in case of 50% drop from the nominal value of the motor current (I_m) along the x-axis of satellite #3 by using 10000 time samples.

DNN #	Actual Healthy	Actual Faulty	Estimated Healthy	Estimated Faulty
DNN x-3	5000 samples	5000 samples	5100 samples	4900 samples
DNN x-2	5000 samples	5000 samples	6100 samples	3900 samples
DNN x-4	5000 samples	5000 samples	5200 samples	4800 samples

the actual faulty output signals and the detection results that are obtained by using the proposed FD scheme. In the second faulty case, a 50% drop from the nominal value of the motor current fault is injected in the x-axis of the satellite #3 at the time sample of 5000. Table 3.31 shows the actual healthy and the actual faulty output signals and the fault detection results that are obtained by using the proposed FD scheme. In the third scenario a high viscous temperature fault (50% increase from the nominal value of the viscous friction) is injected in the x-axis of the satellite #1 at the time sample of 5000. The actual healthy and the actual faulty output signals and the classification results that are obtained by using the proposed FD scheme are shown in Table 3.32. In the fourth scenario a high temperature fault that results in a 10% increase in the nominal value of the viscous friction is injected in the y-axis of the satellite #3 at the time sample of 5000. Table 3.33 shows the actual healthy

Table 3.32: Actual and detection results in case of 50% drop from the nominal value of the motor current (I_m) along the x-axis of satellite #1 by using 10000 time samples.

DNN #	Actual Healthy	Actual Faulty	Estimated Healthy	Estimated Faulty
DNN x-1	5000 samples	5000 samples	5050 samples	4950 samples
DNN x-4	5000 samples	5000 samples	5850 samples	4150 samples
DNN x-2	5000 samples	5000 samples	6050 samples	3950 samples

Table 3.33: Actual and detection results in case of 10% drop from the nominal value of the motor current (I_m) along the y-axis of satellite #3 by using 10000 time samples.

DNN #	Actual Healthy	Actual Faulty	Estimated Healthy	Estimated Faulty
DNN y-3	5000 samples	5000 samples	5000 samples	5000 samples
DNN y-2	5000 samples	5000 samples	6500 samples	3500 samples
DNN y-4	5000 samples	5000 samples	6200 samples	3800 samples

Table 3.34: Actual and detection results in case of 15% drop from the nominal value of the motor current (I_m) along the y-axis of satellite #3 by using 10000 time samples.

DNN #	Actual Healthy	Actual Faulty	Estimated Healthy	Estimated Faulty
DNN y-3	5000 samples	5000 samples	5000 samples	5000 samples
DNN y-2	5000 samples	5000 samples	6400 samples	3600 samples
DNN y-4	5000 samples	5000 samples	5900 samples	4100 samples

and the actual faulty output signals and the classification results that are obtained by using the proposed formation flying FD scheme. A low motor current fault (15% drop of nominal value) is injected in the y-axis of the satellite #3 at the time sample of 5000 and the satellite remains faulty for 5000 steps in the fifth scenario. Table 3.34 shows the actual healthy and the actual faulty output signals and the classification results that are obtained by using the proposed FD scheme. A low bus voltage fault (70% drop of nominal value) has occured in the x-axis of the satellite #2 at the time sample of 5000 and it lasts for 5000 steps in the last scenario. Table 3.35 shows the actual healthy and the actual faulty output signals and the fault detection results that are obtained by using the proposed FD scheme.

Considering the above six faulty scenarios for the satellite #i the following values in Table 3.36 are obtained for the confusion matrix.

Table 3.35: Actual and detection results in case of 70% drop from the nominal value of the bus voltage (V_{BUS}) along the x-axis of satellite #2 by using 10000 time samples.

DNN #	Actual Healthy	Actual Faulty	Estimated Healthy	Estimated Faulty
DNN x-2	5000 samples	5000 samples	5000 samples	5000 samples
DNN x-1	5000 samples	5000 samples	5300 samples	4700 samples
DNN x-3	5000 samples	5000 samples	5700 samples	4300 samples

148

Table 3.36: Confusion matrix parameters for the faulty satellite ($\#i$) and its two nearest neighbors ($\#(i-1)$ and $\#(i+1)$).

DNN #	A	B	C	D
DNN of satellite $\#i$	29850 samples	150 samples	0 samples	30000 samples
DNN of satellite $\#(i-1)$	25980 samples	4020 samples	300 samples	29700 samples
DNN of satellite $\#(i+1)$	26050 samples	3950 samples	450 samples	29550 samples

Table 3.37: Confusion matrix results for the faulty satellite ($\#i$) and its two nearest neighbors ($\#(i-1)$ and $\#(i+1)$).

	DNN of satellite $\#i$	DNN of satellite $\#(i-1)$	DNN of satellite $\#(i+1)$
Accuracy	99%	92%	92%
True healthy	100%	99%	98.5%
False healthy	0%	13%	13%
True faulty	100%	87%	87%
False faulty	0%	1%	1.5%
Precision	100%	88%	88%

According to Table 3.37 the dynamic neural network embedded along the faulty axis of the faulty spacecraft (i.e. satellite $\#i$) can classify 100% of healthy signals and 100% of faulty signals successfully. The accuracy level (99%) and the precision level (100%) of this method are highly acceptable. The dynamic neural network embedded along the corresponding axis of satellite $\#(i-1)$ and satellite $\#(i+1)$ which are the nearest neighbors to satellite $\#i$ can classify 99% of healthy signals and 87% of faulty signals correctly. In comparison to the first scheme, in this method both faulty and healthy signals are classified more precisely. The accuracy level (92%) and the precision (88%) are acceptable as well.

3.17 Conclusions

In this chapter a fault detection system methodology that is developed in [43] for a single satellite is presented and its capabilities and shortcomings in detecting faults are evaluated under different faulty and fault free situations. A fault detection (FD)

scheme for detecting actuator faults in a consensus-based controlled formation of satellites is then proposed. In the single satellite FD system, when a fault occurs in satellite #i, only the FD system embedded in the satellite #i can detect the fault. On the other hand, in case of low severity faults, these local FD systems may fail to detect faults.

For the formation flying system two different FD schemes are investigated in this chapter and the capabilities of the proposed methods for detecting faults are evaluated under different fault scenarios. In the first scheme, once a fault occurs in satellite #i, the fault detection system in satellite #i can detect it immediately and the FD system in satellite #$(i-1)$ can detect the fault with a time delay. So, the first advantage of proposed FD scheme is that when a fault happens in a satellite it can be detected by using local diagnosers immediately and then, after a time delay the fault can be detected by using DNNs that are embedded in the nearest neighbor of the faulty satellite. When the severity of fault increases, even the next neighbor (satellite #$(i-2)$) can detect the fault after longer time delay.

In the second scheme, once a fault occurs in satellite #i, it can be detected by local diagnose immediately. However, since there are communication links between each satellite and its two nearest neighbors, the DNN based FD systems that are embedded in the two adjacent nearest neighbors of satellite #i (satellite #$(i-1)$ and satellite #$(i+1)$) can detect the fault occurrence after a short time delay. However, depending on the fault severity, the next nearest neighbors of satellite #i might be able to detect the fault after longer time delays.

The second advantage of the proposed methods (in both first and second schemes) is their ability to detect low severity faults. Using these schemes, bus voltage faults greater than 45% drop from the nominal value and temperature and motor current faults greater than 5% drop/increase from the nominal values can be detected. Using

the second scheme (bi-directional communication method) the fault can be detected in shorter time delay and the healthy and faulty signals are classified better (in the first scheme only 76% of faulty signals are classified correctly, but using the second scheme almost 87% of faulty signals are classified correctly). The accuracy and precision levels are almost the same in both schemes.

The only disadvantage of the second scheme is that this scheme requires more communication links as compared to the first scheme, especially when a large number of spacecraft are involved in the mission. The communication requirements for each spacecraft during the formation are estimated as follows: In the decentralized control approach, each spacecraft transmits its instantiation of r, v, q and ω of the virtual structure to its two adjacent neighbors (in this thesis we have ignored the group expansion/contraction and we only consider the group translation and the group rotation). We know that r, v and ω each has 3 components and q has 4 components. Thus the coordination vector has 13 components. Assume that each component is encoded as B bits and the sampling rate of the system is $L\ Hz$. By communicating with its two adjacent neighbors, each satellite requires a bandwidth of 26 BL/Hz. In the single satellite FD system, each satellite only uses its own measurements of the command voltage and the reaction torque in order to detect local faults. Thus, the single satellite FD system does not require any additional communication links.

In the formation flying FD system, in the first scheme each satellite only sends its attitude information to its previous neighbor (satellite $\#i$ send its attitude to satellite $\#(i-1)$), and this requires 4 BL/Hz more bandwidth for each spacecraft. In the second scheme, each satellite sends its attitude information to its two nearest neighbors. Thus, this requires $8BL/Hz$ more bandwidth for each spacecraft in the maneuver. Compared to the centralized method, there is no single point of failure

in this proposed method. Also, compared to the centralized approach, fewer communication links are required in this method. The decentralized method provides more flexibility and reliability when compared to the centralized approaches.

Chapter 4

Fault Isolation, Fault Type Determination and Fault Severity Estimation Scheme for a Formation Flight of Satellites

In Chapter 3, we have developed a decentralized fault detection scheme for a formation flying of spacecraft. In order to evaluate the capabilities of the proposed scheme, we have injected various fault scenarios in the attitude control subsystem of the spacecraft and it was shown that when a fault occurs in an actuator of one of the satellites in the formation, the fault diagnosis system embedded in the faulty spacecraft can detect the fault immediately, and the dynamic neural network embedded in its adjacent spacecraft can detect the fault after a short time delay. The next step in an FDI process of a system is fault isolation. Fault isolation is the practice of determining the faulty actuator in the formation and isolating it from other actuators in the system. Limiting the scope of the problem decreases the possibility of serious damage

153

in the entire formation system.

4.1 Fault Isolation Logic

In general, three reaction wheels are embedded in a spacecraft system, and each of them is located along one of the three axes of the spacecraft. In our proposed formation flying fault diagnosis system, a dynamic neural network is embedded along each axis of each satellite in the formation. When a high severity fault occurs in one of the reaction wheels in the i-th spacecraft in the formation, the dynamic neural network that is embedded along the corresponding axis of the i-th spacecraft can detect the fault immediately (without time delay). In this way, one not only can detect a fault, but also can isolate the faulty actuator in the formation.

4.1.1 Fault Isolation Results for a Formation Flying of Satellites

In Chapter 3, a fault detection scheme is proposed for the reaction wheels of the satellites in a formation flight mission. The proposed methodology has the capability of detecting and isolating actuator faults simultaneously. The fault isolation logic is based on the fault detection time delays in the formation flying system. This capability has been investigated under various fault scenarios:

- First scenario: In this case, a 60% drop from nominal value of the bus voltage fault along the x-axis of the satellite #1 has occurred. The fault detection time delay results are depicted in Table 4.1. According to Table 4.1 once this fault occurs along the x-axis of satellite #1, the corresponding DNN along the x-axis of the satellite #1 can detect the fault immediately, and the DNNs embedded along the other axes of satellite #1 can detect the fault after a short time delay

154

Table 4.1: Fault detection time delays in case of 60% drop from nominal value in the bus voltage of x-axis of satellite #1.

Dynamic Neural Network #	Fault Detected	Detection Time Delay	Faulty Axis
DNN x-1	YES	0 sec	×
DNN y-1	YES	5 sec	
DNN z-1	YES	5 sec	
DNN x-2	NO	-	
DNN y-2	NO	-	
DNN z-2	NO	-	
DNN x-3	YES	15 sec	
DNN y-3	YES	17 sec	
DNN z-3	YES	15 sec	
DNN x-4	YES	11 sec	
DNN y-4	YES	7 sec	
DNN z-4	YES	8 sec	

(approximately 5 seconds). In our proposed fault detection scheme, the attitude information of satellite #1 is transmitted to its adjacent neighbor (i.e. satellite #4) according to Fig. 3.18. Once a fault occurs in satellite #1 it affects the attitude of satellite #4 and satellite #3. Since the DNNs embedded in satellite #4 are trained based on the relative attitude of satellite #4 with respect to satellite #1, the DNNs embedded in satellite #4 and satellite #3 can detect the fault after a time delay. Since satellite #4 is the closest satellite to satellite #1 in the formation (as far as communication delay is considered), the DNNs in satellite #4 detect the fault within a shorter time delay and since satellite #2 is the farthest satellite from satellite #1 in the formation (as far as communication delay is considered), the DNNs in satellite #2 cannot detect the fault that has occurred in satellite #1. Table 4.1 shows that the DNN in the z-axis of the satellite #1 is the first DNN in the formation-level FD system that can detect the fault occurrence. This reveals that the reaction wheel along the x-axis of the satellite #1 is faulty.

- Second scenario: In this case a motor current fault (50% drop from the nominal

Table 4.2: Fault detection time delays in case of 50% drop of nominal values in the motor current of x-axis of satellite #2.

Dynamic Neural Network #	Fault Detected	Detection Time Delay	Faulty Axis
DNN x-1	YES	13 sec	
DNN y-1	YES	10 sec	
DNN z-1	YES	10 sec	
DNN x-2	YES	0 sec	×
DNN y-2	YES	6 sec	
DNN z-2	YES	2 sec	
DNN x-3	NO	-	
DNN y-3	NO	-	
DNN z-3	NO	-	
DNN x-4	YES	15 sec	
DNN y-4	YES	20 sec	
DNN z-4	YES	15 sec	

value) has occurred in the x-axis of the satellite #2 in a formation flight mission. When this fault occurs in the x-axis of the satellite #2, the DNN in the x-axis of the satellite #2 can detect the fault immediately and since in our proposed formation level fault detection system, the attitude information of satellite #2 is transmitted to satellite #1 (the adjacent spacecraft in the ring topology), therefore, the DNNs in the satellite #1 can detect the fault occurrence after a short time delay. In the ring topology, the attitude information of the satellite #2 is then transmitted to the satellite #4, therefor the DNNs in the satellite #4 can detect the fault within a longer time delay. The fault detection time delays in the DNNs of the satellites in the formation flight mission are depicted in Table 4.2.

- Third scenario: In this case a low severity viscous friction fault (10% increase from the nominal value) has occurred along the y-axis of the satellite #3. The time delays in the fault detection are shown in Table 4.3. According to this table, once a fault is occurred along the y-axis of satellite #3, the DNN embedded along the faulty axis of the faulty spacecraft (satellite #3) can detect the fault

Table 4.3: Fault detection time delays in case of 10% increase in nominal values of the viscous friction of y-axis of satellite #3.

Dynamic Neural Network #	Fault Detected	Detection Time Delay	Faulty Axis
DNN x-1	NO	-	
DNN y-1	NO	-	
DNN z-1	NO	-	
DNN x-2	YES	14 sec	
DNN y-2	YES	16 sec	
DNN z-2	YES	14 sec	
DNN x-3	YES	7 sec	
DNN y-3	YES	0 sec	$\times$
DNN z-3	YES	8 sec	
DNN x-4	NO	-	
DNN y-4	NO	-	
DNN z-4	NO	-	

immediately (0 second time delay), and then the fault is detected by DNNs along the x-axis and z-axes of satellite #3. The closest agent to the satellite #3 in the formation is satellite #2. Therefore, the attitude deviations in satellite #3 will affect the orientation of satellite #2 within a short time delay. Therefore the DNNs embedded in satellite #2 can detect the fault after a time delay. Due to the low severity of the temperature fault that is occurred in this scenario (10% increase from the nominal value) the fault occurrence in satellite #3 does not affect the second nearest neighbor of satellite #3 in the ring topology. Therefore only DNNs in the satellite #3 (the faulty satellite) and satellite #2 (the nearest neghbor of the faulty satellite) can detect the fault, and since according to Table 4.3 the DNN in the y-axis of the satellite #3 can detect fault in the first place, this reveals that the fault is occured in the y-axis of the satellite #3.

4.2 A Dynamic Neural Network-Based Methodology for Fault Type Classification and Fault Severity Estimation

In this section a multi dynamic neural network-based method is proposed for fault type classification and fault severity estimation in actuators of the satellites in the formation flying mission. In this approach, in the first level, a dynamic neural network is employed for classifying the actuator faults into one of the three actuator fault type categories, namely, bus voltage fault, motor current fault and temperature fault. In the second level, this DNN-based fault type classifier is followed by another dynamic neural network to estimate the fault severity in the faulty actuator.

4.2.1 Fault Type Classification Using Dynamic Neural Classifier

In general three types of faults may occur in the reaction wheels of a spacecraft, namely, a bus voltage fault, a motor current fault and a viscous friction fault as shown in Table 4.4. These three types of faults have been described in Section 2.8. In this methodology, after detecting fault occurrence in the formation flying system and isolating the faulty actuator (determining the location of the faulty reaction wheel in the formation flying system) in order to determine the type of the fault that has occurred in the faulty actuator, a dynamic neural network-based method is proposed. The structure of the proposed scheme is depicted in Fig. 4.1. In this scheme, the residual signals that are generated in the formation-level fault detection system are processed such that the magnitudes of the residual signal before and right after the fault occurrence is applied as the two input to the DNN-based classifier. The output of
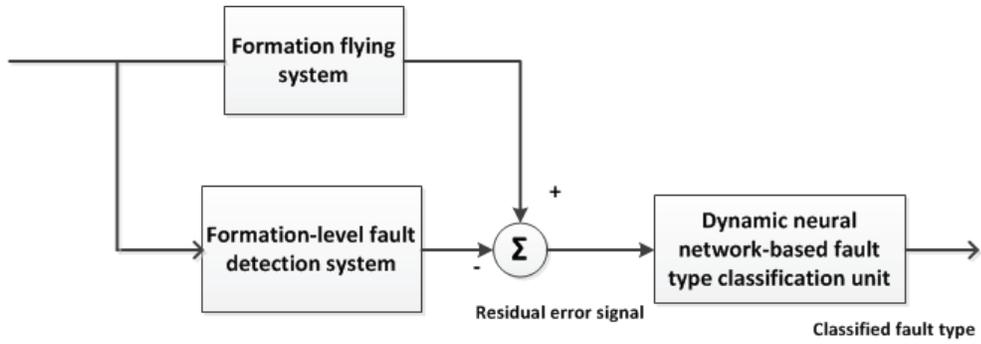
Figure 4.1: Dynamic neural network-based scheme for fault type determination.

Table 4.4: Reaction wheel fault types assignments.

Reaction Wheel Fault Type	Assigned Fault Type Class
Motor current fault	+1
Bus voltage fault	-1
Temperature fault	0

the neural classifier determines the fault type that has occurred in the faulty actuator.

4.2.2 Training Phase

In this section, the residual signals which are generated by using the formation level dynamic neural network-based fault detection scheme are processed as the input data to train the dynamic neural classifiers. In order to train the DNN-based fault type classifiers, the residual signals that are collected under various faulty operating condition of the spacecraft and are used for training purposes. The magnitudes of the residual signal before and right after the fault occurrence are applied as the two inputs to the dynamic neural classifier. Preprocessing steps are performed on the input/output data pairs so that all the data used for DNN training are normalized in the range of [-1, +1]. The training process is then carried out based on an extended dynamic back-propagation algorithm for each axis.

The network parameters are initialized with small random values and the IIR filter's denominator coefficients are initialized to zeros. The structure of the dynamic neural network contains one hidden layer of hyperbolic tangent activation functions and one output layer of linear activation functions. The neurons embedded in the structure of the dynamic neural network have second order IIR filters. The training process is started from a relatively small network structure and the optimum structure is obtained by incrementally increasing the number of hidden neurons until required performance specifications are met. The training phase is conducted for each DNN that is employed along each axis of the satellite. The best results are obtained using a N_{2-5-1} structure, which implies that there is two neuron in the input layer (the first input of the network is the magnitude of the residual signal generated in the formation level fault detection system before fault occurrence and the second input of the neural classifier is the magnitude of the residual signal after the fault occurrence), 8 neurons in the hidden layer and one neuron in the output layer (the output of the neural classifier is the corresponding fault type class). The learning rate parameter is set to 0.001. The training process is accomplished by using Monte Carlo's simulations under different noisy conditions for 20000 fault scenarios (including 5000 motor current fault scenarios, 5000 bus voltage fault scenarios and 5000 temperature fault scenarios and 5000 fault free scenarios). The performance indices (i.e. mean square error) of the neural classifiers during the training phase for 3 axis of satellite #1 are depicted in Fig. 4.2.

4.2.3 Testing Phase

The classification capability of the trained DNN-based classifier is evaluated in the testing phase. In the testing phase another input/output data set is used to evaluate the capabilities of the trained DNNs to classify the fault types. The testing step is

160
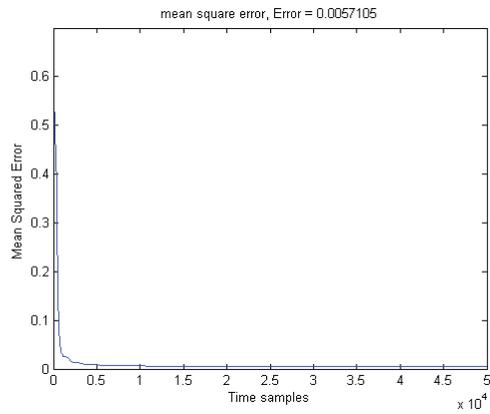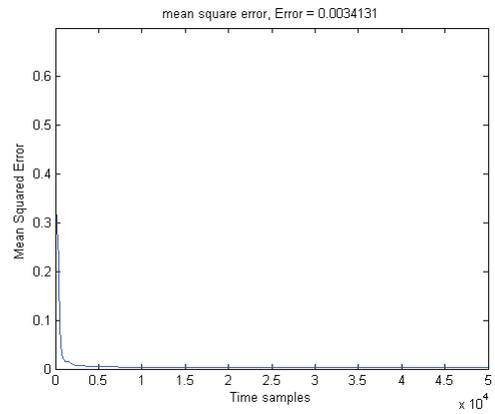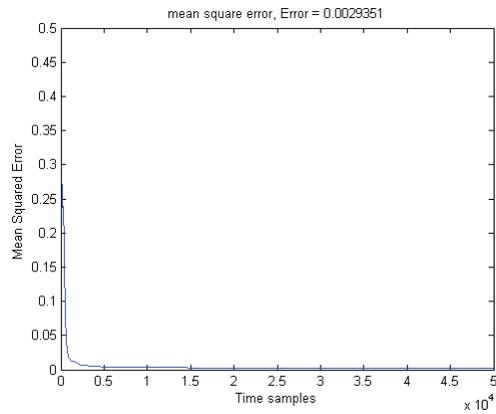
Figure 4.2: The performance index (mean squared error of the fault classes) curve for the dynamic neural network classifier- satellite #1 (a) x-axis, (b) y-axis (c) z-axis.

accomplished for 20000 different pairs of input residual signal data that is generated under 15000 different faulty scenarios (including 5000 bus voltage fault scenarios, 5000 temperature fault scenarios, 5000 motor current fault scenarios and 5000 fault free scenarios) are applied to the trained neural classifiers to investigate the classification capabilities of the trained networks. These residual signals are generated by using the formation-level fault detection systems of the satellites in presence of normally distributed noise with zero mean and standard deviation of 0.01 differences between the maximum and the minimum values in the input/output data intervals. Fig. 4.3 shows the actual fault type class and the output of the neural classifier in the testing phase in the three axes of the satellite #1. The results indicate that the trained DNNs have the ability to classify the faults of the reaction wheels correctly. The testing phase for the other satellites can be accomplished in a similar way.

4.2.4 Fault Type Classification Results

In order to investigate the classification capabilities of the proposed neural classifiers, these classifiers are applied following the formation level fault detection system in the formation flying mission. The following three different fault scenarios are considered in this section:

- First scenario: In this scenario a bus voltage fault (45% drop from the nominal value) has occurred in the z-axis of the satellite #2 in the formation flying. The residual signal that is generated in the formation level fault detection scheme is applied to the neural classifier and Fig. 4.4 shows that the proposed neural classifier can detect the fault type correctly and assign the actuator fault to the correct fault class.

- Second scenario: In this scenario a motor current fault (50% drop from the nominal value) has occurred in the x-axis of the satellite #3 in the formation
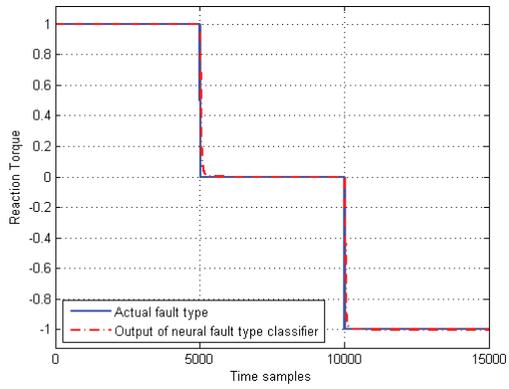
(a)
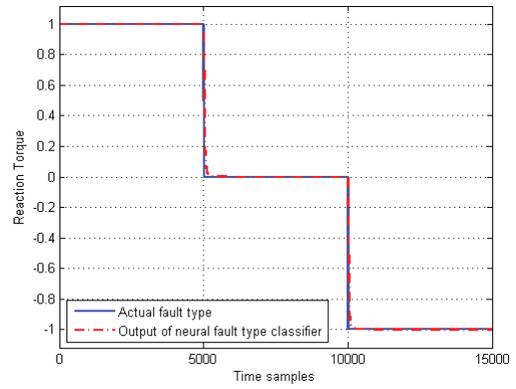
(b)
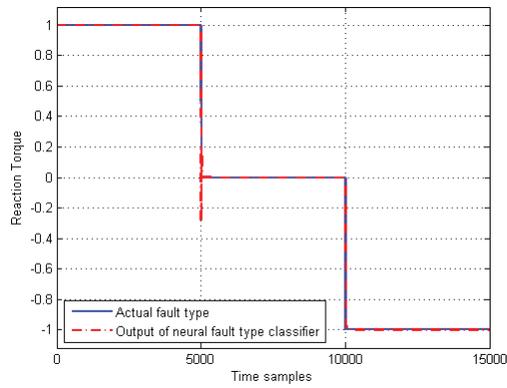
(c)

Figure 4.3: Testing curve (actual and estimated fault classes) for the DNN - (a) x-axis, (b) y-axis, and (c) z-axis of the satellite #1.
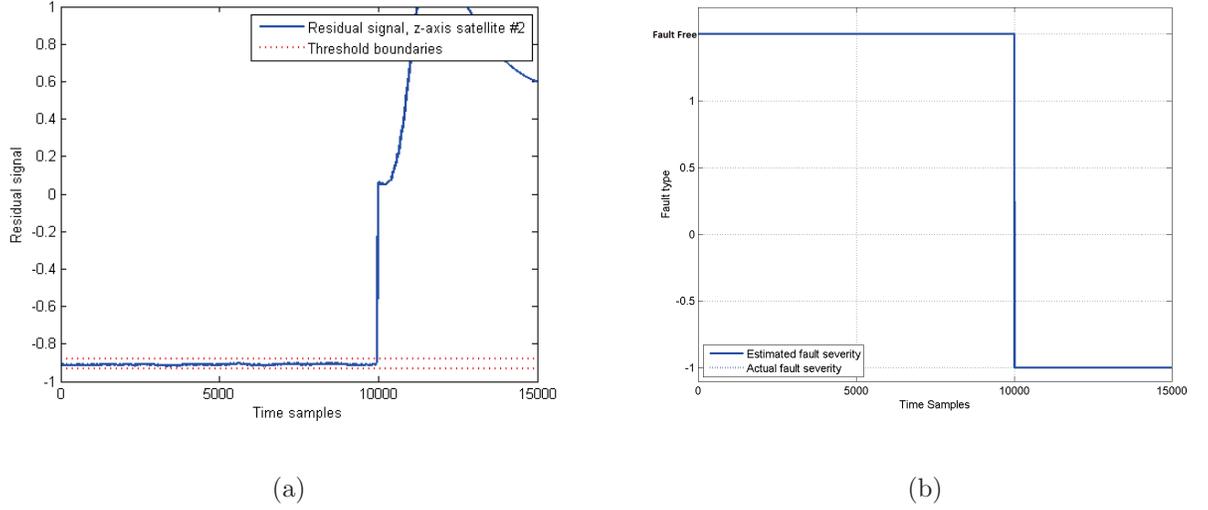
Figure 4.4: First scenario: (a)Residual signal from the formation level fault detection system (b) Output of DNN-based fault type classifier.

flying. The neural classifier receives the residual signal that is generated in the formation level fault detection scheme as the input data and determines the fault type. Fig. 4.5 shows that the proposed neural classifier can detect the fault type correctly and assigns the actuator fault to the correct fault class.

- Third scenario: In this case, a 50% increase in the nominal value of the viscous friction occurs in the x-axis of the satellite #1. Fig. 4.6 shows that the proposed dynamic neural classifier has the capability of classifying the actuator fault correctly.

4.2.5 Dynamic Neural Network-Based Fault Severity Estimation Method

In this section a dynamic neural network-based scheme is proposed for estimating fault severity in the faulty actuator in the formation flight mission. When a fault occurrence in one of the actuators in the formation is detected in the the formation

164
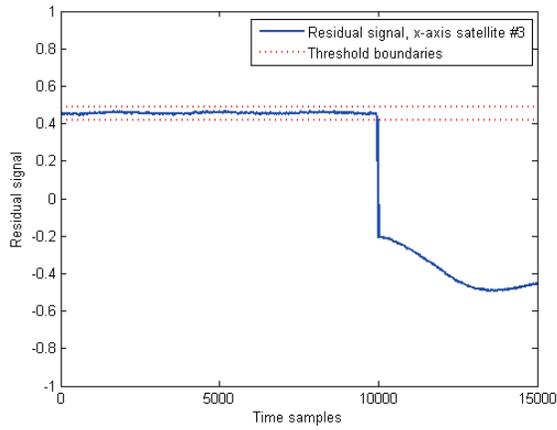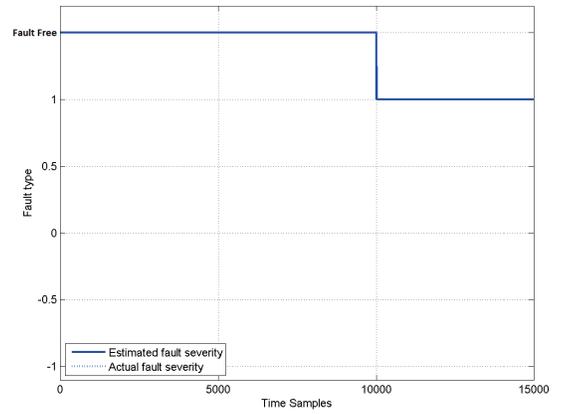
Figure 4.5: Second scenario: (a)Residual signal from the formation level fault detection system (b) Output of DNN-based fault type classifier.
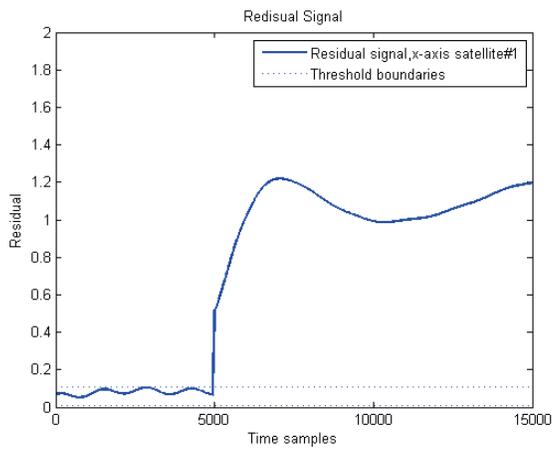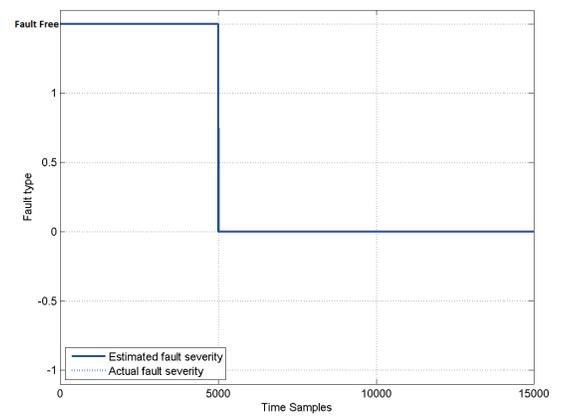
Figure 4.6: Third scenario: (a)Residual signal from the formation level fault detection system (b) Output of DNN-based fault type classifier.

165
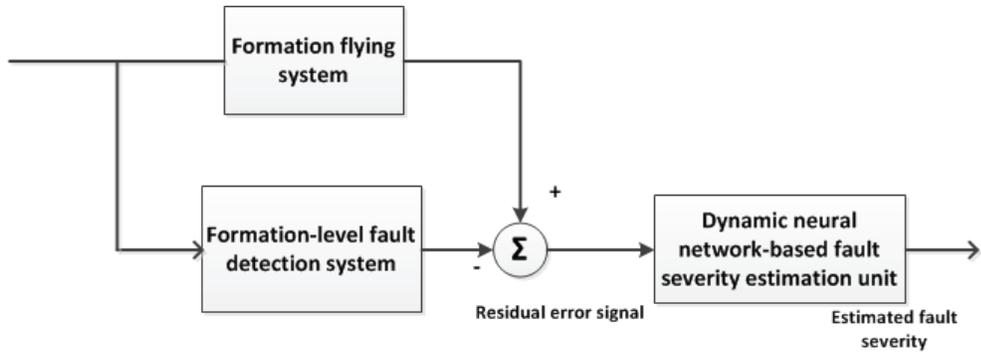
Figure 4.7: Dynamic neural network-based scheme for fault severity estimation.

level dynamic neural networks, the location of the faulty actuator is determined in the fault isolation step and the fault type is determined by using the proposed DNN-based method in Section 4.2.1. The next step is to propose a method for estimating fault severity in the faulty actuator in the formation. In order to fulfill this objective, in our proposed scheme, the DNN-based fault type classifier is followed by another dynamic neural network that is employed for estimating fault severity in the faulty actuator. This fault estimation DNN is also trained based on the residual signals that are obtained from the formation level fault detection system. The structure of the DNN-based fault severity estimation unit is depicted in Fig. 4.7.

The residual signals that are generated in the formation level fault detection systems under faulty operating conditions are processed such that the input of the fault severity estimation neural network is the difference magnitude in the residual signal before and right after the fault occurrence. A quantitative study of the effects of the motor current, the viscous temperature and the bus voltage fault severities on the residual signals that are generated in the corresponding faulty axis of the faulty satellite is provided in Tables 4.5-4.7, respectively. According to these tables, as the severity of actuator fault increases, the difference magnitude in the steady state residual signal at the fault occurrence time increases. This property is used to determine the severity of the fault in the actuators of a satellite in the formation

166

Table 4.5: Motor current fault severity at the time of fault occurrence.

Fault Severity	Healthy Magnitude of the residual signal at the fault time	Faulty Magnitude of the residual signal at the fault time	Difference Magnitude
5% I_m	-0.03625	-0.1017	0.06545
10% I_m	-0.0310	-0.1620	0.131
15% I_m	-0.0453	-0.2416	0.1963
20% I_m	-0.0260	-0.2880	0.262
30% I_m	0.1120	-0.2815	0.3935
45% I_m	0.8807	0.2916	0.5891
50% I_m	1.1291	0.47471	0.6544
55% I_m	1.089	0.3690	0.72
60% I_m	1.188	0.4026	0.7854
75% I_m	1.206	0.2240	0.982
80% I_m	1.1885	0.1410	1.0475
90% I_m	1.200	0.0173	1.1827
95% I_m	1.2126	-0.0080	1.2206

structure.

4.2.6   Training Phase

In this section, the residual signals which are generated by using the formation level dynamic neural network-based fault detection scheme are processed and the difference between the magnitude of the residual signal before fault occurrence and the magnitude of the residual signal right after the fault occurrence is applied as the input data to train the dynamic neural networks to estimate the fault severity.

In order to train the DNN-based fault type classifiers, the residual signals that are collected under various faulty operating condition of the spacecraft are used in training phase. Preprocessing steps are performed on the input/output data pairs so that all the data used for DNN training are normalized in the range of [-1, +1]. The training process is then carried out based on an extended dynamic back-propagation algorithm for each axis.

Table 4.6: Motor current fault severity at the time of fault occurrence.

Fault Severity	Healthy Magnitude of the residual signal at the fault time	Faulty Magnitude of the residual signal at the fault time	Difference Magnitude
5% τ_v	0.0143	0.0591	0.0448
10% τ_v	0.0140	0.1038	0.0898
15% τ_v	0.0140	0.1483	0.1343
20% τ_v	0.0540	0.2330	0.1790
30% τ_v	-0.0267	-0.2952	0.2685
45% τ_v	0.0118	0.4147	0.4029
50% τ_v	0.0670	0.5141	0.4471
55% τ_v	0.0093	0.5010	0.4917
60% τ_v	-0.015	-0.5520	0.537
75% τ_v	-0.2940	0.3774	0.668
80% τ_v	0.467	-0.2491	0.7161
90% τ_v	0.6680	-0.1378	0.8058
95% τ_v	-0.6048	0.222	0.8268

Table 4.7: Motor current fault severity at the time of fault occurrence.

Fault Severity	Healthy magnitude of the residual signal at the fault occurrence	Faulty magnitude of the residual signal at the fault occurrence	Difference magnitude
45% V_{BUS}	-0.862	0.1075	0.9695
50% V_{BUS}	-0.9561	0.1193	1.0754
55% V_{BUS}	-1.05	0.13115	1.18115
60% V_{BUS}	-1.108	0.1446	1.2526
65% V_{BUS}	-1.241	0.1548	1.3958
70% V_{BUS}	-1.334	0.1666	1.5006
75% V_{BUS}	-1.430	0.1784	1.6084
80% V_{BUS}	-1.525	0.191	1.716
85% V_{BUS}	-1.620	0.2021	1.8221
90% V_{BUS}	-1.715	0.215	1.93
95% V_{BUS}	-1.818	0.226	2.044

The network parameters are initialized with small random values and the IIR filter's denominator coefficients are initialized to zeros. The structure of the dynamic neural network contains one hidden layer of hyperbolic tangent activation functions and one output layer of linear activation functions. The neurons embedded in the structure of the dynamic neural network have second order IIR filters. The training process is started from a relatively small network structure and the optimum structure is obtained by incrementally increasing the number of hidden neurons until required performance specifications are met. The training phase is conducted for each DNN that is employed along each axis of the satellite. The best results are obtained using a N_{1-7-1} structure, which implies that there is one neuron in the input layer (the input of the network is the difference magnitude of the residual signal that is generated in the formation level fault detection system at the fault occurrence time), 7 neurons in the hidden layer and one neuron in the output layer (The output of the neural classifier is the fault severity). The learning rate parameter is set to 0.001. The training process is accomplished by using Monte Carlo's simulations under different noisy conditions for 30000 fault scenarios (including 10000 motor current fault scenarios, 10000 bus voltage fault scenarios and 10000 temperature fault scenarios). The networks are trained for different pairs of input/output data in presence of a normally distributed noise with zero mean and standard deviation of 0.01 differences between the maximum and the minimum values in the input/output data intervals. The performance of the dynamic neural networks during the training phase for 3 axis of satellite #1 is depicted in Fig. 4.8.

4.2.7 Testing Phase

The capability of the trained DNNs in estimating actuator fault severity is investigated in the testing phase. In this phase another input/output data set is used to
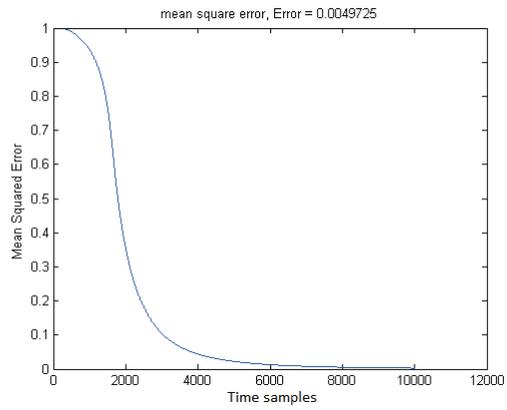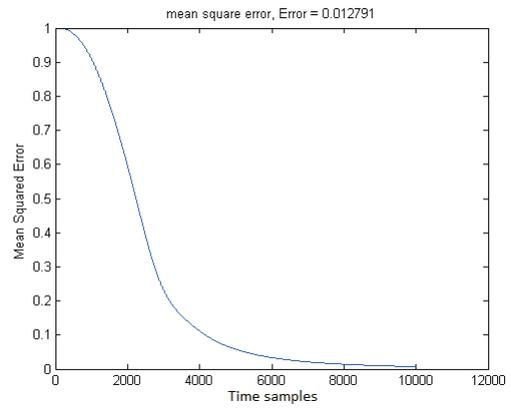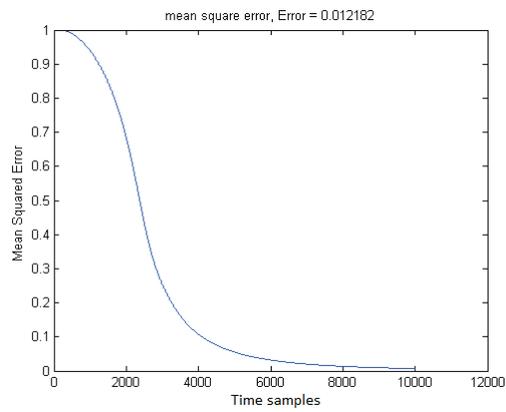
Figure 4.8: The performance index (mean squared error of the fault severity) curve for the dynamic neural network in fault severity estimation- satellite #1 (a) x-axis, (b) y-axis (c) z-axis.
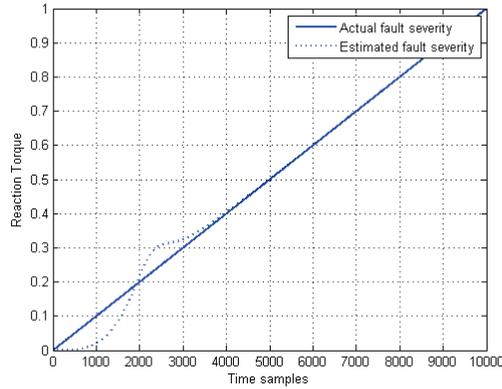
Figure 4.9: Testing curve (actual and estimated fault severity) for the DNNs in fault severity estimation level- Motor current fault.

evaluate the capabilities of the trained DNNs to estimate the fault severities. The testing step for the motor current faults is accomplished for 10000 different pairs of input residual signal data that is generated under 10000 various faulty cases (including 10000 motor current fault scenarios) is applied to the trained dynamic neural networks to investigate the capabilities of the trained networks. The residual signals that are generated by using the formation-level fault detection systems of the satellites in the formation in presence of a normally distributed noise with zero mean and standard deviation of 0.01 differences between the maximum and the minimum values in the input/output data intervals is applied as the input data to the neural networks in fault severity estimation level. Fig. 4.9 shows the actual fault severity and the output of the neural classifier in the testing phase. The results indicate that the trained DNNs have the ability to estimate the fault severity in the reaction wheels correctly. The testing phase for the other axes of the satellite can be accomplished in a similar way.

In order to investigate the capabilities of the proposed DNN-based method in estimating temperature fault severities in the faulty actuator of the faulty satellite in the formation, 10000 various temperature fault scenarios are considered and the

171
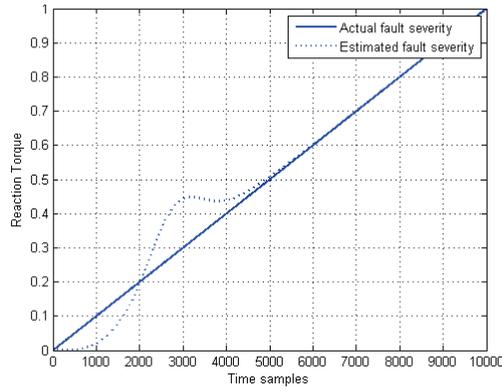
Figure 4.10: Testing curve (actual and estimated fault severity) for the DNNs in fault severity estimation level- Temperature fault.
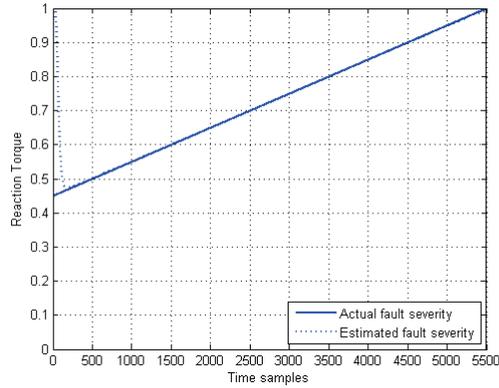
Figure 4.11: Testing curve (actual and estimated fault severity) for the DNNs in fault severity estimation level- Bus voltage fault.

actual fault severity and estimated value for the fault severity is depicted in Fig. 4.10.

In Fig. 4.11 the capabilities of the proposed method is tested for 5500 different bus voltage scenarios are investigated. The actual fault severities and the estimated fault severities (by using the DNN-based approach) is depicted in this figure.
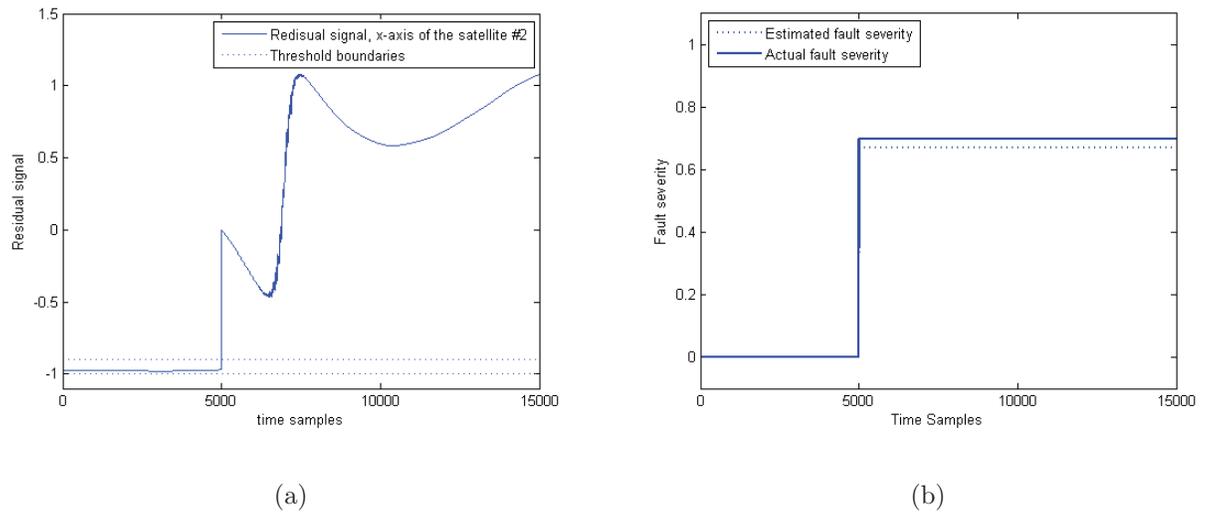
Figure 4.12: First scenario: (a) Residual signal from the formation level fault detection system (b) o utput of DNN-based fault severity estimator.

4.2.8 Fault Severity Estimation Results Using Dynamic Neural Network-Based Method

In order to investigate the capabilities of the proposed dynamic neural networks in estimating fault severity in the faulty actuator in the formation flight mission, various fault scenarios are considered. The DNNs for fault severity estimation level are applied following the fault type determination system in the formation flying mission. In this section, the following three different fault scenarios are considered:

- First scenario: In this scenario a bus voltage fault (70% drop from the nominal value) is occurred in the x-axis of the satellite #2 in the formation flying. The residual signal that is generated in the formation level fault detection scheme is applied to the neural classifier and Fig. 4.12 show that the proposed neural classifier can detect the fault type correctly and assign the actuator fault to the correct fault class.

- Second scenario: In this scenario a motor current fault (80% drop from the
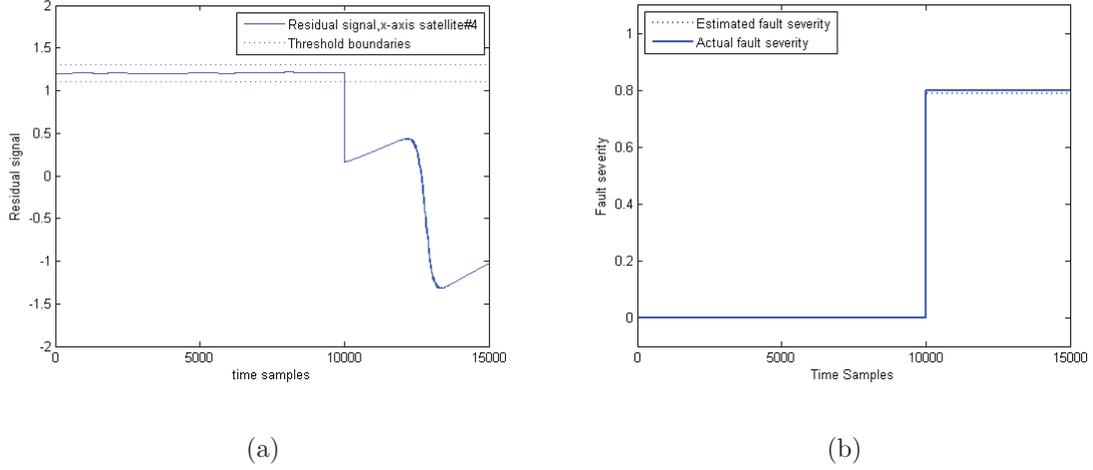
Figure 4.13: Second scenario: (a) Residual signal from the formation level fault detection system (b) output of DNN-based fault severity estimator.

nominal value) is occurred in the y-axis of the satellite #4 in the formation flying. The neural classifier receives the residual signal that is generated in the formation level fault detection scheme as the input data and determines the fault type. Fig. 4.13 shows that the proposed neural classifier can detect the fault type correctly and assign the actuator fault to the correct fault class.

• Third scenario: In this case, a 50% increase in the nominal value of the viscous friction occurs in the x-axis of the satellite #2. Fig. 4.14 shows that the proposed dynamic neural classifier has the capability of classifying the actuator fault correctly.
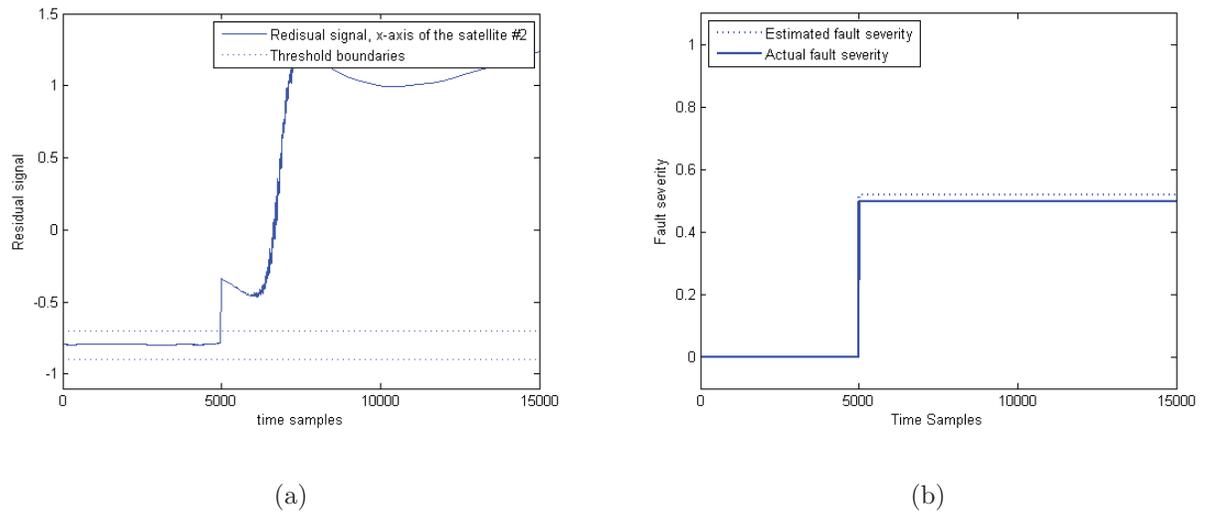
Figure 4.14: Third scenario: (a) Residual signal from the formation level fault detection system (b) output of DNN-based fault severity estimator.

4.3 A Static Neural Network-Based Methodology for Fault Type Classification and Fault Severity Estimation

In Chapter 3, it is shown that by using the proposed formation flying fault detection methodology, bus voltage faults greater than 45% drop from the nominal value can be detected. In addition, the proposed method has the capability of detecting motor current faults and temperature faults greater than 5% drop/increase from the nominal values. The proposed method can detect the fault occurrence and isolate the fault (i.e detect the location of the fault in the formation flying) at the same time. In this section a multilayer perceptron neural network that is depicted as in Fig. 2.1 and is directly applied following the dynamic neural network detectors to classify the residual signals that are generated by using the formation flying fault diagnosis system. This neural classifier receives information from the residual error

175
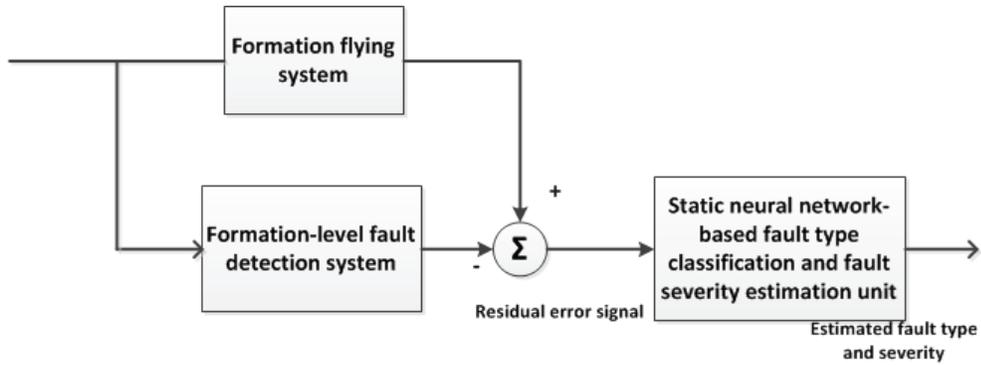
Figure 4.15: General structure of the fault type classification and fault severity estimation system.

signals and determines the type and the severity of the fult that has occurred in the faulty actuator.

In order to perform the classification task, the neural classifier has to be trained on the residual error signals that are generated in the formation level dynamic neural fault diagnosis system by using the back-propagation method and then the classifier performs the residual validation task and assigns each of the residual signals to one of the predefined fault type classes and estimate the severity of fault.

The general structure of the fault type classification and fault severity estimation system is depicted in Fig. 4.15. In this structure, the DNN that is employed along each axis of each satellite in the formation is followed by a static neural classifier that is employed for the fault type classification purposes. The classifiers are applied for classifying residual error signals which are generated during the steady state operation of the spacecraft and they have the capability of classifying single faults that have been injected in the reaction wheels of each axis of the spacecraft, including the voltage fault, motor current fault and viscous temperature fault. Using the proposed method, the severity of the actuator fault can be estimated too.

When a fault is detected in one of the axes of the satellite $\#i$ in the formation, the neural classifier embedded along the faulty axis of the faulty spacecraft receives

the magnitude of the residual signal before and after the fault occurrence. The static neural network is trained based on residual signals (value of the residual signals at the moment of the fault occurrence as well as before and after of the fault occurrence) and classifies the residual signals into one of the fault type categories.

In our proposed FDI scheme, when the system is fault free, the residual signal remains in the threshold boundaries. Once a fault occurs in the reaction wheel of one of the spacecraft in the formation, the residual signal exceeds the threshold and the fault is detected. When a severe fault occurs in the actuators, the residual signal exceeds the threshold, but when the fault severity is low, the residual signal exceeds significantly the threshold. The increased severity of the fault results in increasing the difference magnitude of the residual signal at the moment of fault occurrence before and after the fault occurrence.

4.4 A Static Neural Network-Based Fault Type Classification and Fault Severity Estimation Method

A static multilayer perceptron neural classifier is constructed along each axis of each spacecraft in the formation. These static neural networks receive the residual signals that are generated in the formation-level fault detection system and process the residual signal that is generated in the faulty axis of the faulty spacecraft in the formation and use the magnitude of the residual signal right before and after the fault occurrence as inputs. The first and the second output of the neural network are the fault type and the fault severity, respectively.

4.4.1 Training Phase

The proposed static neural networks are trained using the residual signal that is generated in the formation-level fault detection system of the faulty spacecraft in the mission, under different faulty conditions (including bus voltage fault scenarios, motor current fault scenarios and temperature fault scenarios). The learning process is carried out based on the back-propagation algorithm for 20000 input/output data set corresponding to motor current faults, 20000 input/output data set corresponding to the temperature fault cases and 11000 input/output data set corresponding to bus voltage fault scenarios, and the best results are obtained with the network structure of $N_{2-5-5-2}$, which implies that there are two inputs (which are the magnitude of the residual error signal before and after the fault occurrence), 5 neurons in the first hidden layer, 5 neurons in the second hidden layer and 2 outputs (the first output identifies the fault type and the second output determines the fault severity). The learning rate is set to 0.005. The network is trained for 10000 epochs until a performance index requirement is satisfied. Fig. 4.16 shows that the required performance index (i.e. the mean square error) is satisfied during the training phase.

4.4.2 Testing Phase

In order to evaluate the capabilities of the trained neural network, we use the trained static neural network to classify different fault types and estimate the severities of the faults that can occur in the reaction wheel of the spacecraft along one axis. In the testing step, the residual signals that are generated under 10000 different motor current fault scenarios, 10000 different temperature fault scenarios and 5500 different bus voltage scenarios are applied to the neural classifier and the output signals are depicted in Fig. 4.17- Fig. 4.19. These figures show that the proposed classifier can
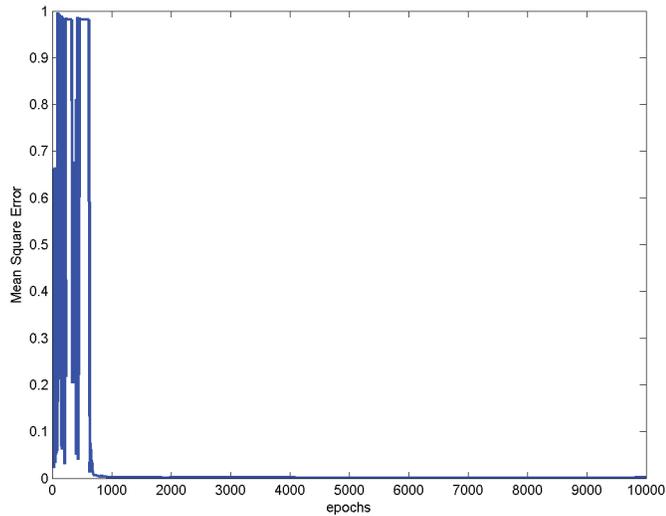
Figure 4.16: Learning curve for the static neural classifier network.

classify the fault type and estimate the fault severity with an acceptable accuracy.

In this step, first in order to evaluate the capability of this static neural network-based method, 10000 different motor current fault scenarios are considered. The residual signals that are generated using the DNNs in the formation flying level fault detection system under these 10000 different motor current fault scenarios are applied to the neural classifier.

The neural classifier receives the residual signal. The magnitude of the residual signal at the moment of fault occurrence (the magnitude of the residual signal right before and after of fault occurrence) are applied as the two inputs of the neural classifier. The output of the neural classifier under these 10000 motor current fault scenarios is shown in Fig. 4.17. This figure shows that when a motor current fault has occurred in a reaction wheel in the formation flight system, the proposed static neural classifier can detect the fault type correctly (the actual fault type class that is assigned for motor current faults is +1, and the static neural classifier can classify the fault type correctly. However, there are some miss classifications in some samples).
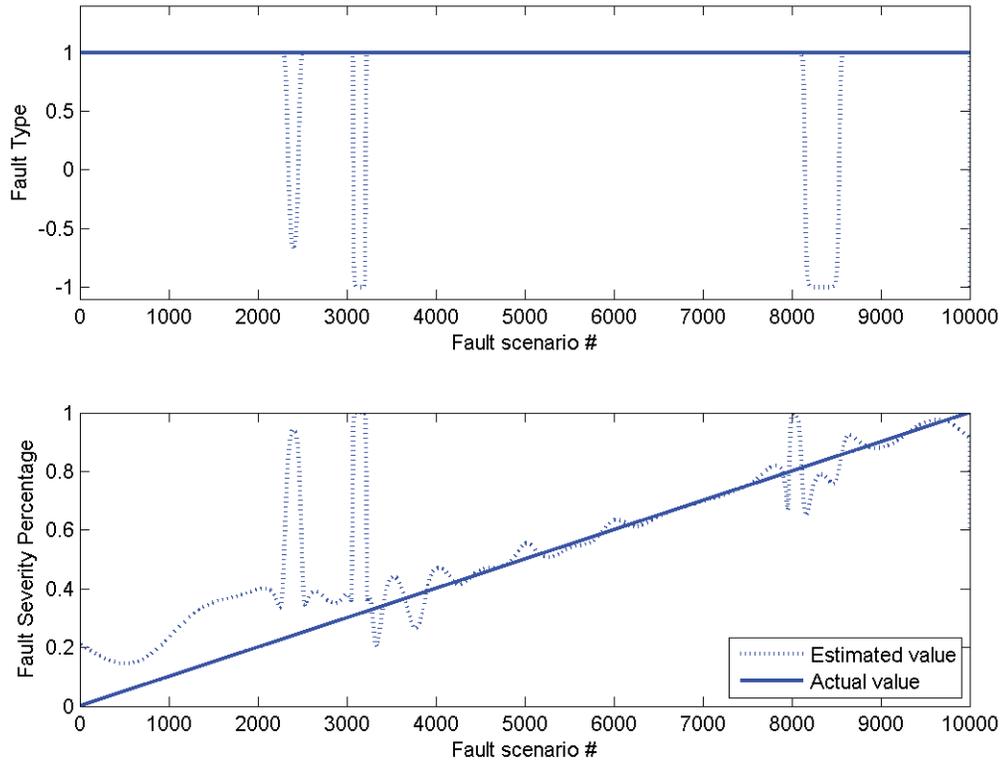
Figure 4.17: Fault classification results for 10000 different motor current fault scenarios.

According to Fig. 4.17 the proposed static classifier can estimate the fault severity. The actual and the estimated fault severities in various 10000 motor current fault cases are depicted in Fig. 4.17.

In order to evaluate the capability of the proposed neural classifier in classifying the temperature faults, 10000 different temperature faults are considered. The neural classifiers process the residual signals generated in DNNs of the formation flying system. These neural networks employ the magnitude of the residual signal at the moment right before and after of the fault occurrence as the input signal. Fig. 4.18 shows the actual fault type and fault severity and the estimated outputs of the neural network classifier for 10000 different temperature fault scenarios. It shows that the
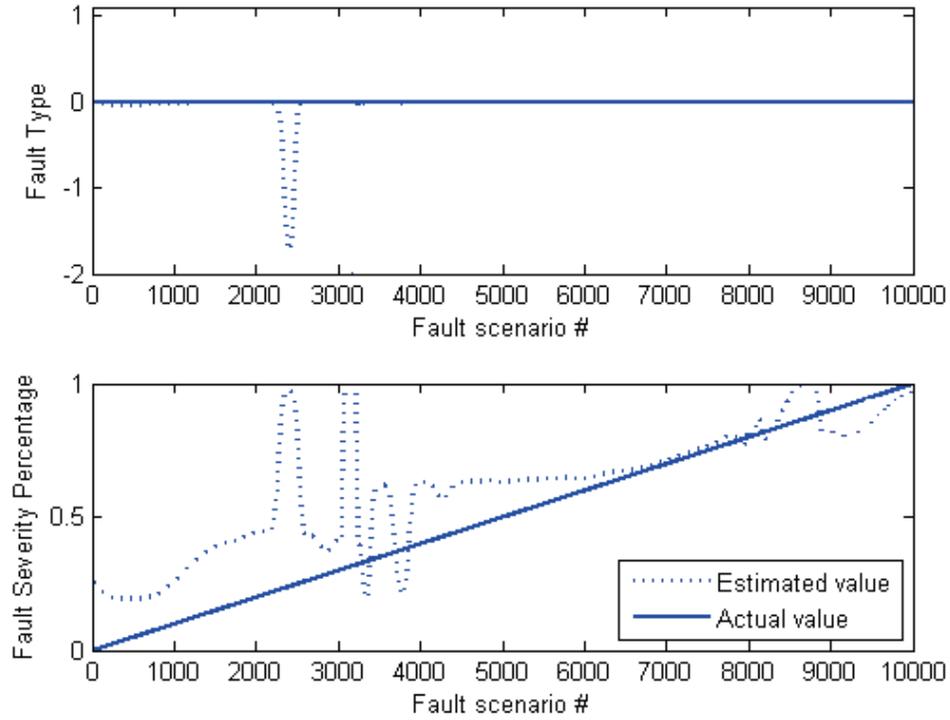
Figure 4.18: Fault classification results for 10000 different temperature fault scenarios.

proposed static neural network an detect the fault type and it can estimate the fault severity.

The capabilities of the proposed methodology in classifying the actuator fault type and the fault severity have been further investigated under 5500 different bus voltage scenarios. The residual error signals that are generated under 5500 different bus voltage scenarios have been applied as the input to the neural network classifier. The actual fault type and fault severity and the estimated values that are obtained by using static neural network are depicted in Fig. 4.19.
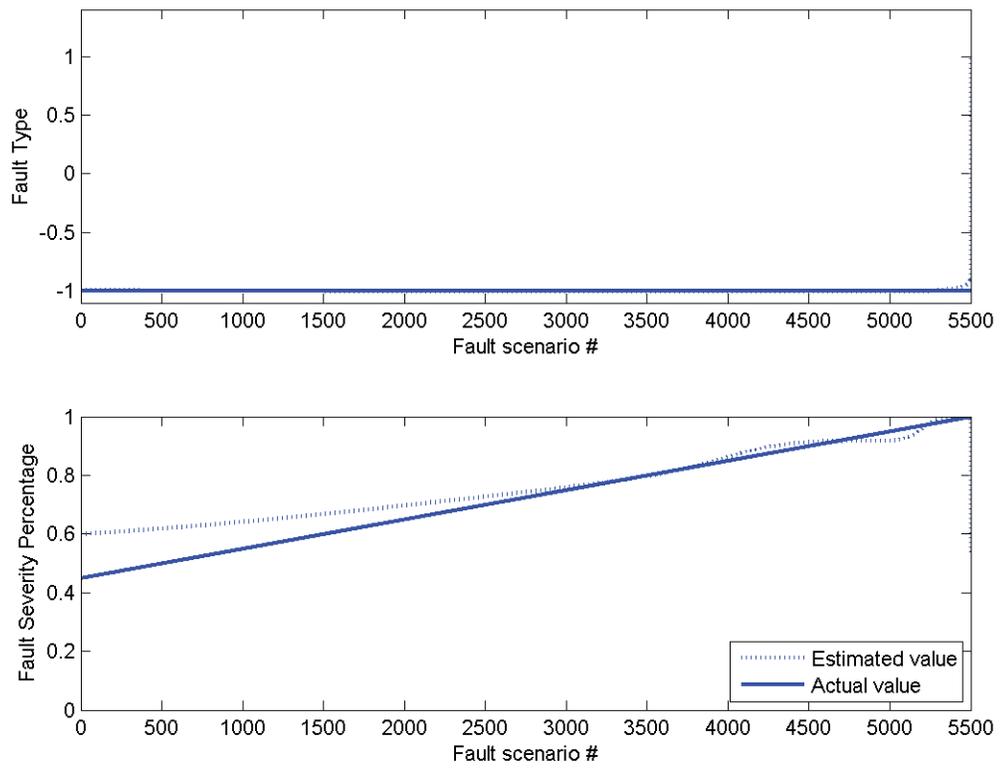
Figure 4.19: Fault classification results for 10000 different bus voltage fault scenarios.

4.4.3 Fault Type Determination and Fault Severity Estimation Results Using Static Neural Network-Based Method

In this section, in order to evaluate the capabilities of the proposed static neural network-based classification method, different fault scenarios is considered. In the following scenarios, the static neural network receives the residual signal that is generated under faulty situation in the formation level fault detection system and the magnitude of the residual signal before fault occurrence and right after the fault occurrence is applied as the two inputs to the static neural network. The two outputs of the static neural network, that are trained using back-propagation method, is the actuator fault type and actuator fault severity, respectively.

- First scenario: In this case a 45% drop from the nominal value of the bus voltage fault has occured in the reaction wheel of the z-axis of the satellite #2 in the formation flight mission. Fig. 4.20 shows the actual and estimated values for the type and the severity of the fault that has occurred in the faulty actuator in the formation.

- Second scenario: In the second scenario, a motor current fault (80% drop from the nominal value) has been injected in the reaction wheel along the y-axis of the satellite #4 in the formation flight mission. The residual signal generated in the formation level fault detection system and the estimated and the actual value of the fault severity and the fault type is depicted in Fig. 4.21.

- Third scenario: In this case a 50% increase in the nominal value of the viscous friction has occurred in the reaction wheel in the x-axis of the satellite #2 in the formation flight mission. The residual signals that are generated in the fault detection system in the formation level and the output of the static neural network are also shown in Fig. 4.22.
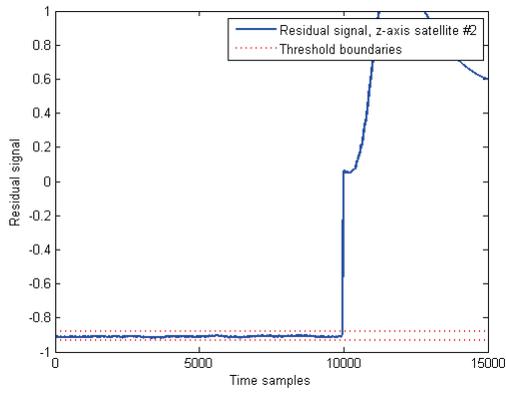
(a)
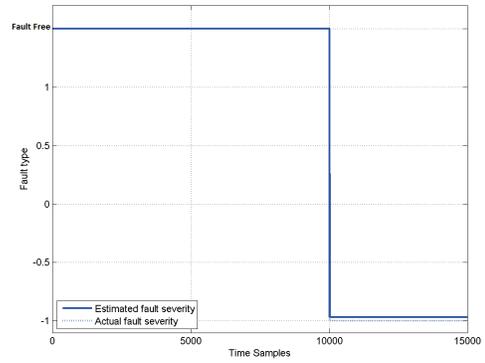
(b)
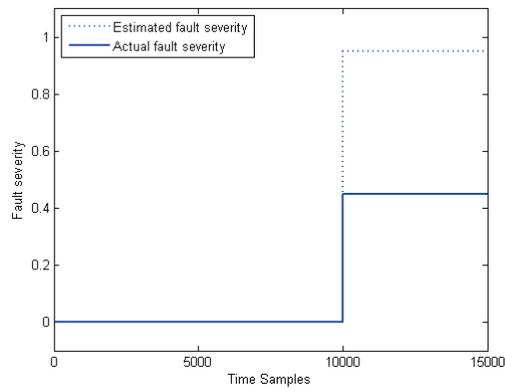
(c)

Figure 4.20: First scenario: (a) Residual signal from the formation level fault detection system (b) Fault type(c) Fault severity.
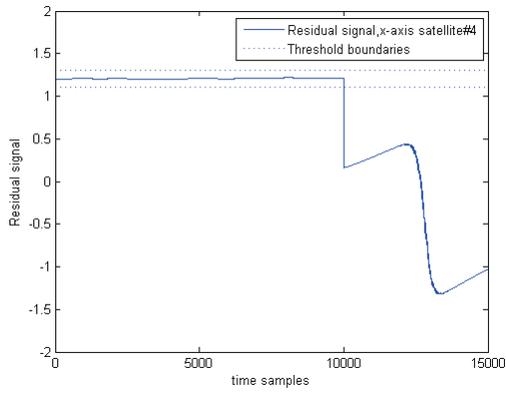
(a)
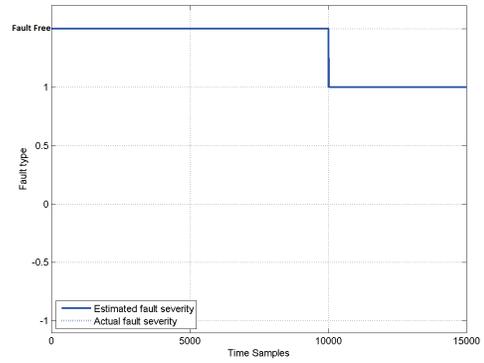
(b)
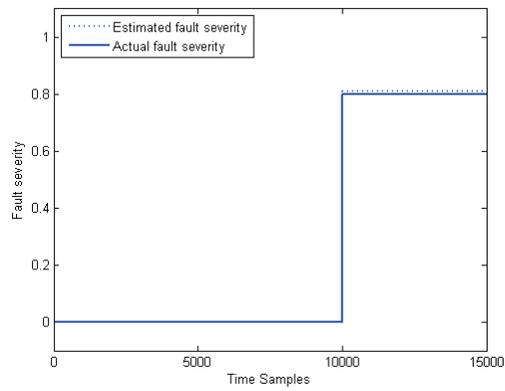
(c)

Figure 4.21: Second scenario: (a) Residual signal from the formation level fault detection system (b) Fault type(c) Fault severity.
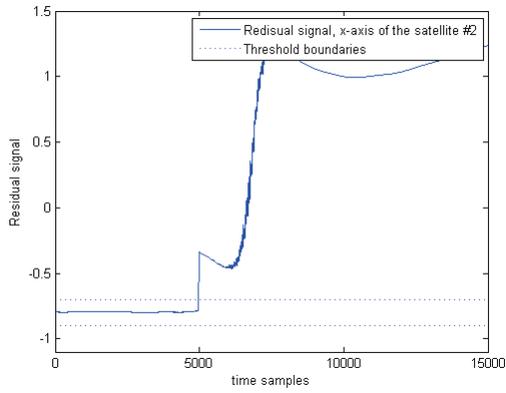
(a)
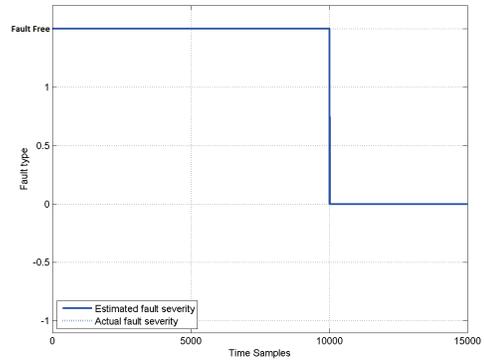
(b)
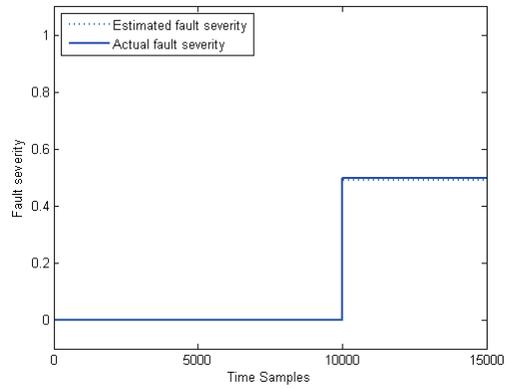
(c)

Figure 4.22: Third scenario: (a) Residual signal from the formation level fault detection system (b) Fault type(c) Fault severity.

4.5 Analysis of the Results

In this chapter, two different method for fault type detection and fault severity estimation in the actuators of a satellite in a formation flight mission is proposed. In the first approach, the classification task is performed by using dynamic neural networks that are introduced in Chapter 2. In the second approach, the conventional static neural networks are employed to detect the fault type and the fault severity in the faulty actuator in the formation flight mission. In order to evaluate the classification capabilities of our proposed schemes, the confusion matrix method is used.

4.5.1 Analysis of the Results for the Dynamic Neural Network-Based Method for Fault Type Classification and Fault Severity Estimation

In order to evaluate the fault type classification and the fault severity estimation capabilities of the proposed dynamic neural network-based method a confusion matrix analysis is used. The actual and estimated fault type and fault severity for 30 different motor current scenarios are depicted in Table 4.8. Thirty (30) different temperature fault scenarios are considered and the actual and the estimated fault type and fault severity estimation results are depicted in Table 4.9. Finally, in Table 4.10 the actual and estimated values for fault type and fault severity in the faulty actuator in the formation flying system under 20 different bus voltage scenarios are listed.

In Tables 4.8-4.10 the classification results for 80 different faulty scenarios, including 30 temperature fault scenarios, 30 motor current fault scenarios and 20 bus voltage fault scenarios that are described above are shown. Table 4.11 shows the number of patterns in each fault class and the number of patterns that are correctly/

Table 4.8: Actual and classification results under 30 different motor current fault cases - DNN method.

Fault type	Actual Fault Severity	Classified Fault Type	Estimated Fault Severity
Motor Current Fault	10%	+1	2.8%
Motor Current Fault	12%	+1	3.94%
Motor Current Fault	15%	+1	10.02%
Motor Current Fault	20%	+1	21.32%
Motor Current Fault	30%	+1	32.15%
Motor Current Fault	32%	+1	33.05%
Motor Current Fault	35%	+1	35.98%
Motor Current Fault	38%	+1	38.13%
Motor Current Fault	40%	+1	40.15%
Motor Current Fault	42%	+1	42.05%
Motor Current Fault	45%	+1	45.03%
Motor Current Fault	48%	+1	48%
Motor Current Fault	50%	+1	49.98%
Motor Current Fault	52%	+1	52%
Motor Current Fault	55%	+1	55%
Motor Current Fault	58%	+1	58%
Motor Current Fault	60%	+1	60%
Motor Current Fault	62%	+1	62%
Motor Current Fault	65%	+1	65%
Motor Current Fault	68%	+1	68%
Motor Current Fault	70%	+1	70%
Motor Current Fault	72%	+1	72%
Motor Current Fault	75%	+1	75%
Motor Current Fault	78%	+1	78%
Motor Current Fault	80%	+1	80%
Motor Current Fault	82%	+1	82%
Motor Current Fault	85%	+1	85%
Motor Current Fault	88%	+1	88%
Motor Current Fault	90%	+1	90%
Motor Current Fault	95%	+1	95%

Table 4.9: Actual and classification results under 30 different temperature fault cases - DNN method.

Fault type	Actual Fault Severity	Classified Fault Type	Estimated Fault Severity
Temperature Fault	10%	0.5	2.8%
Temperature Fault	12%	0.11	3.94%
Temperature Fault	15%	0.07	10.02%
Temperature Fault	18%	0.04	17.82%
Temperature Fault	20%	0.01	21.32%
Temperature Fault	22%	0.01	26.34%
Temperature Fault	25%	0	31.87%
Temperature Fault	28%	0	31.98%
Temperature Fault	32%	0	33.05%
Temperature Fault	35%	0	35.98%
Temperature Fault	38%	0	38.13%
Temperature Fault	40%	0	40.15%
Temperature Fault	42%	0	42.15%
Temperature Fault	45%	0	45.03%
Temperature Fault	48%	0	48%
Temperature Fault	50%	0	49.98%
Temperature Fault	52%	0	52%
Temperature Fault	55%	0	55%
Temperature Fault	58%	0	58%
Temperature Fault	60%	0	60%
Temperature Fault	62%	0	62%
Temperature Fault	65%	0	65%
Temperature Fault	70%	0	70%
Temperature Fault	72%	0	72%
Temperature Fault	75%	0	75%
Temperature Fault	80%	0	80%
Temperature Fault	82%	0	82%
Temperature Fault	85%	0	85%
Temperature Fault	92%	0	92%
Temperature Fault	95%	0	95%

Table 4.10: Actual and classification results under 20 different bus voltage fault cases - DNN method.

Fault type	Actual Fault Severity	Classified Fault Type	Estimated Fault Severity
Bus Voltage Fault	45%	-0.97	98.87%
Bus Voltage Fault	50%	-0.99	50%
Bus Voltage Fault	53%	-0.99	53%
Bus Voltage Fault	55%	-0.99	55%
Bus Voltage Fault	58%	-1	58%
Bus Voltage Fault	60%	-1	60%
Bus Voltage Fault	62%	-1	62%
Bus Voltage Fault	65%	-1	65%
Bus Voltage Fault	68%	-1	68%
Bus Voltage Fault	70%	-1	70%
Bus Voltage Fault	73%	-1	73%
Bus Voltage Fault	75%	-1	75%
Bus Voltage Fault	78%	-1	78%
Bus Voltage Fault	80%	-1	80%
Bus Voltage Fault	82%	-1	82%
Bus Voltage Fault	85%	-1	85%
Bus Voltage Fault	88%	-1	88%
Bus Voltage Fault	90%	-1	90%
Bus Voltage Fault	92%	-1	92%
Bus Voltage Fault	95%	-1	95%

Table 4.11: Actual fault type and classification results under different fault cases - DNN method.

Fault type	Number of faulty scenarios	Correctly classified	Wrongly classified
Bus voltage fault	20	20	0
Motor current fault	30	30	0
Temperature fault	30	29	1

Table 4.12: Actual fault severity and estimated fault severity under different fault cases - DNN method.

Fault type	Number of faulty scenarios	Correctly estimated	Poorly estimated	Wrongly estimated
Bus voltage fault	20	19	0	1
Motor current fault	30	25	5	0
Temperature fault	30	25	5	0

poorly classified. Table 4.12 shows a quantitative analysis of the fault severity estimation results for various actuator fault scenarios.

Table 4.13 shows the error in fault severity estimation under the above 80 faulty scenarios (including 30 motor current fault scenarios, 30 temperature fault scenarios and 20 bus voltage scenarios). The average fault severity estimation error is depicted in Table 4.13 for various actuator fault scenarios.

Table 4.13: Actual fault severity and estimation results under different fault cases - DNN method.

Fault type	Average fault severity estimation error
Bus voltage fault	2.7%
Motor current fault	0.9%
Temperature fault	1.5%

4.5.2 Analysis of the Results for the Static Neural Network-Based Method for Fault Type Classification and Fault Severity Estimation

In order to evaluate the classification capabilities of the proposed static neural network-based (SNN) method, 30 different motor current fault scenarios are considered and the 30 fault scenarios and the output of neural network classifier for these scenarios have been described clearly in Table 4.14. Table 4.15 shows the actual 30 temperature fault scenarios and the output of the neural classifier for the fault type and the fault severity values under these 30 scenarios. The estimated values and the actual values for fault type and fault severity results in 20 different fault scenarios are listed in Table 4.16.

In Tables 4.14-4.16 the classification results for 80 different faulty scenarios, including 30 temperature fault scenarios, 30 motor current fault scenarios and 20 bus voltage fault scenarios that are described above are shown. Table 4.17 and Table 4.18 show the number of patterns in each fault class and the fault type/fault severity estimation results for various fault scenarios respectively. Table 4.19 shows the fault severity estimation analysis results for static neural network based method.

Comparing the analysis results in Table 4.18 and Table 4.12 shows that the dynamic neural network-based method has higher accuracy in estimating fault severity (including bus voltage faults, motor current faults and temperature faults) and it has lower estimation error.

4.6 Conclusion

In this chapter, a fault isolation logic and methodology is developed first and for the purpose of fault type recognition and fault severity determination two methods

Table 4.14: Actual and classification results under 30 different motor current fault cases - SNN method.

Fault type	Actual Fault Severity	Classified Fault Type	Estimated Fault Severity
Motor Current Fault	10%	+1	21.98%
Motor Current Fault	12%	+1	29.91%
Motor Current Fault	15%	+1	38.04%
Motor Current Fault	20%	+1	40.81%
Motor Current Fault	25%	+0.78	32.83%
Motor Current Fault	30%	+1	40.83%
Motor Current Fault	32%	-1.01	50.63%
Motor Current Fault	35%	+1	46.32%
Motor Current Fault	38%	+1	23.85
Motor Current Fault	42%	+1	42.88%
Motor Current Fault	45%	+1	46.17%
Motor Current Fault	48%	+1	48.08%
Motor Current Fault	50%	+1	58.26%
Motor Current Fault	52%	+1	52.69%
Motor Current Fault	55%	+1	54.37%
Motor Current Fault	58%	+1	58.88%
Motor Current Fault	60%	+1	65.63%
Motor Current Fault	62%	+1	60.25%
Motor Current Fault	65%	+1	65.72%
Motor Current Fault	68%	+1	68.39%
Motor Current Fault	70%	+1	71.03%
Motor Current Fault	72%	+1	71.85%
Motor Current Fault	75%	+1	75.33%
Motor Current Fault	78%	+1	79.66%
Motor Current Fault	80%	+1	78.06%
Motor Current Fault	82%	-1.01	60.54%
Motor Current Fault	85%	-.99	75.07%
Motor Current Fault	88%	+1	89.4%
Motor Current Fault	90%	+1	88.12%
Motor Current Fault	95%	+1	96.36%

Table 4.15: Actual and classification results under 30 different temperature fault cases - SNN method.

Fault type	Actual Fault Severity	Classified Fault Type	Estimated Fault Severity
Temperature Fault	10%	0	25.67%
Temperature Fault	12%	0	31.88%
Temperature Fault	15%	0	38.8%
Temperature Fault	18%	0	41.87%
Temperature Fault	20%	0	44.5%
Temperature Fault	22%	-0.02	46.4%
Temperature Fault	25%	-0.18	85.5%
Temperature Fault	28%	0	38.76%
Temperature Fault	32%	0	85.6%
Temperature Fault	35%	0	61.9%
Temperature Fault	38%	0	21.8%
Temperature Fault	40%	0	62.5%
Temperature Fault	42%	0	59%
Temperature Fault	45%	0	63.1%
Temperature Fault	48%	0	63.6%
Temperature Fault	50%	0	63%
Temperature Fault	52%	0	64%
Temperature Fault	55%	0	64.1%
Temperature Fault	58%	0	64.8%
Temperature Fault	60%	0	64.3%
Temperature Fault	62%	0	65.7%
Temperature Fault	65%	0	67.2%
Temperature Fault	70%	0	71.2%
Temperature Fault	72%	0	73.7%
Temperature Fault	75%	0	77%
Temperature Fault	80%	0	82%
Temperature Fault	82%	0	79.7%
Temperature Fault	85%	0	95%
Temperature Fault	92%	0	80.8%
Temperature Fault	95%	0	85.2%

Table 4.16: Actual and classification results under 20 different bus voltage fault cases - SNN method.

Fault type	Actual Fault Severity	Classified Fault Type	Estimated Fault Severity
Bus Voltage Fault	45%	-1	43.25%
Bus Voltage Fault	50%	-1	61.51%
Bus Voltage Fault	53%	-1	62.98%
Bus Voltage Fault	55%	-1	63.55%
Bus Voltage Fault	58%	-1	64.77%
Bus Voltage Fault	60%	-1	66.21%
Bus Voltage Fault	62%	-1	67.95%
Bus Voltage Fault	65%	-1	69.23%
Bus Voltage Fault	68%	-1	70.81%
Bus Voltage Fault	70%	-1	72.16%
Bus Voltage Fault	73%	-1	73.15%
Bus Voltage Fault	75%	-1	76.45%
Bus Voltage Fault	78%	-1	78.65%
Bus Voltage Fault	80%	-1	80.02%
Bus Voltage Fault	82%	-1	82.08%
Bus Voltage Fault	85%	-1	86.48%
Bus Voltage Fault	88%	-1	89.06%
Bus Voltage Fault	90%	-1	91.15%
Bus Voltage Fault	92%	-1	91.13%
Bus Voltage Fault	95%	-1	94.69%

Table 4.17: Actual and classification results under different fault cases - SNN method.

Fault type	Number of faulty scenarios	Correctly classified	Wrongly classified
Bus voltage fault	20	16	4
Motor current fault	30	26	4
Temperature fault	30	29	1

Table 4.18: Actual fault severity and estimated fault severity under different fault cases - SNN method.

Fault type	Number of faulty scenarios	Correctly estimated	Poorly estimated	Wrongly estimated
Bus voltage fault	20	19	0	1
Motor current fault	30	18	2	10
Temperature fault	30	9	9	12

Table 4.19: Actual fault severity and estimation results under different fault cases - Static neural network (SNN) method.

Fault type	Average fault severity estimation error
Bus voltage fault	3.25%
Motor current fault	6.66%
Temperature fault	15.5%

are proposed. In the first methodology, a two-level dynamic neural network-based method is developed. In the first level, a dynamic neural network is trained by using the residual signals generated in the formation level fault detection system based on the extended back-propagation algorithm for the purpose of detecting fault types that occur in the reaction wheels in the formation flight system. In the second level, another dynamic neural network is trained based on the analysis of the residual signals that are generated in the formation level fault detection process for the purpose of estimating actuator fault severities.

In the second methodology, a static neural-network-based method is proposed for detecting fault type and estimating the fault severity in the faulty actuator in the formation flight system. In this methodology, the static neural networks are trained based on the residual signals that are generated in the formation level fault detection system by using conventional back-propagation method. The capabilities of the both proposed schemes (dynamic neural network-based scheme and static neural-network-based scheme) are evaluated under different fault scenarios. The results presented demonstrate a reliable approach for fault type classification and severity determination for actuator faults.

Chapter 5

Conclusion and Future Work

5.1 Summary of Contributions

In this thesis the problem of fault detection and isolation (FDI) for a formation flying of satellites is investigated. Due to the capability of dynamic neural networks (DNNs) to cope with nonlinearity, complexity, uncertainty and noisy and corrupted data, in this work DNNs are employed to solve the problem of fault detection and isolation of the attitude control subsystem (ACS) of a satellite. In this thesis a dynamic neural network-based FDI system is designed and developed to detect and isolate the faults in the reaction wheels of satellites located in any of three axes of the satellites in the formation. Various FDI systems for single spacecraft missions have been previously developed in the literature [43], [150], [13], [18], [29]. Unfortunately these local fault diagnosis schemes fail to detect and isolate low severity faults that occur in the re-action wheels of a spacecraft. Although these low severity faults may not cause any serious problem in a single satellite missions, they may cause serious impact on the satellite's attitude or rates in a formation flight mission of a network of satellites.

In this thesis, a decentralized FDI system is proposed for detecting and isolating actuator faults in a formation flight mission. Unlike the local FDI systems (that use

absolute measurements of a spacecraft) the formation flying FDI systems use relative attitude measurements collected from sensors of the 3-axes attitude control subsystem of the satellite in the formation. The formation flying FDI system is developed based on the DNN approach in order to identify normal and faulty modes of operation. The DNN is constructed based on the dynamic multilayer perceptron (DMLP) network in which static neurons are replaced with dynamic neuron model.

Two different FDI topologies have been investigated in this thesis. In the first topology the DNNs in each satellite are trained based on the relative attitude of that satellite with respect to its adjacent neighbor in the bidirectional ring topology. In this approach when a fault occurs in one axis of one of satellites in the formation, the DNN located along the faulty axis of faulty spacecraft can detect and isolate the fault immediately, and the DNN in the neighboring satellite can detect the fault after a time delay.

The capabilities of this approach are evaluated by using a confusion matrix analysis method. In this fault scheme, the DNN located in faulty axis of faulty spacecraft can detect 100% of the faulty signals correctly and the DNN of the neighboring spacecraft can detect 76% of the faulty signals correctly. The accuracey (87%) and precision (82%) level is also acceptable in this method.

In the second approach, DNNs of each spacecraft use the relative attitude measurements of that spacecraft with respect to its two nearest adjacent neighbors in the bidirectional ring topology. The capability of this proposed scheme is also investigated under different faulty scenarios and its capability is evaluated using the confusion matrix method. In this approach, the DNN located in the faulty axis of the faulty spacecraft can detect 100% of the faulty signals correctly (without a time delay) and the DNNs located in its two neighboring satellites can detect the actuator fault after a short time delay (compared to the first fault detection topology) and

they can classify 87% of faulty signals correctly. The accuracey (92%) and precision (88%) levels are improved as compared to the first fault detection topology.

The proposed fault diagnosis scheme has the capability of detecting and isolating faults at the same time. Fault isolation is the practice of determination of faulty actuator in the formation and isolating it from other actuators in the system. In general, three reaction wheels are embedded in a spacecraft system, and each of them is located along one of the three axes of the spacecraft. In our proposed formation flying fault detection system, a dynamic neural network is embedded along each axis of each satellite in the formation. In this way, not only one can detect a fault, but also isolate the faulty actuator in the formation.

In general three types of faults may occur in reaction wheels of a spacecraft; namely bus voltage faults, motor current faults and viscous temperature faults. In order to classify the type of faults in the attitude control subsystem of any of the satellites in the formation, two neural network-based methodologies (dynamic neural network-based (DNN) and static neural network-based (SNN)) are employed after the residual generator in each axis of each satellite. These neural network classifiers use information from the residual signal generated in the faulty axis of the faulty satellite (before and after the fault occurrence) to train the neural networks. Finally, two methodologies for fault severity determination are also proposed and developed. When the severity of the actuator faults in a satellite increase, the magnitude of the residual signal in the faulty axis of the faulty satellite in the formation before and after the fault occurrence increase. This property has been used for developing a fault severity determination scheme.

5.2   Thesis Contributions

The contributions of the work developed in this thesis are detailed as follows:

- In this thesis, a DNN-based decentralized fault detection and isolation method for the reaction wheels of the satellites in a formation flight is developed. In this method, the DNN located in each axis of a satellite in the formation is trained based on the relative attitude measurements of that satellite and its neighboring satellite(s). In this thesis, two different topologies have been investigated: In the first topology, the DNNs of the satellite $\#i$ in the formation is trained using the relative attitude of satellite $\#i$ and satellite $\#(i+1)$. In this fault detection scheme, when a fault occurs in one of the reaction wheels of satellite $\#i$ in the formation, the DNN located in the corresponding axis of the satellite $\#i$ can detect the fault without a time delay, and the DNN located in the corresponding axis of the satellite $\#(i-1)$ can detect the fault after a short time delay. In the second topology, the DNNs of the satellite $\#i$ in the formation are trained using the relative attitude of satellite $\#i$ and its two neighboring satellites, namely satellite $\#(i-1)$ and satellite $\#(i+1)$. In this fault detection method, when a fault occurs in a reaction wheel in satellite $\#i$, the DNN in the corresponding axis of satellite $\#i$ is capable of detecting the actuator fault immediately, and the DNNs in satellite $\#(i-1)$ and $\#(i+1)$ can detect the fault after a short time delay. By using these two proposed fault detection schemes, the fault occurrence in a satellite in the formation mission, can be detected either in the local fault detection system of the faulty satellite or in the fault detection systems of its neighboring satellite(s).

- The proposed fault detection schemes are capable of detecting low severity faults that occur in the reaction wheels of satellites in the formation. The single satellite fault detection system can detect high severity faults in the reaction wheels of the satellite, but it fails to detect low severity faults in the actuators of the satellite. These low severity actuator faults do not have any serious impact on

200

the attitude or rates of a single satellite, but in formation flying missions, low severity actuator faults can result in serious deviations from mission specifications and they may lead to catastrophic failure in the entire formation. Developing a fault detection scheme that is capable of detecting both high severity and low severity faults in the formation mission is the second contribution of this thesis.

- The proposed methodology shows a high level of accuracy (98%) and precision (100%) and the mis-classification rate and false faulty parameters are small (2%) in the confusion matrix analysis. Therefore, the proposed DNN-based fault detection method fulfills the expected requirements of accuracy and precision with minimum mis-classification rate and false alarms.

- The proposed methodology is capable of detecting and isolating the actuator faults at the same time. In both schemes, a DNN is located in three axes of each satellite in the formation. Once a fault occurs in one of the actuators of any of the satellites in the formation, the DNN that is located in the corresponding axis can detect the fault without a time delay. This property is used for isolation purpose.

- Two neural network-based methods (DNN-based method and SNN-based method) are employed to determine the fault type and the fault size in the faulty actuator. The DNN that is located in each axis of each satellite in the formation is followed by a static/dynamic neural network. These neural networks are trained based on the residual signal that is generated in the DNN-based residual generator in the faulty axis and then the trained neural networks are used to classify the fault type and estimate the fault severity.

5.3 Suggestions for Future Work

Based on the results obtained in this thesis, the suggested future work can be focused on the following areas:

- Since in this thesis a decentralized fault diagnosis scheme is proposed, a fault in one satellite can be observed by its adjacent satellites in the formation as well. Although this provides a more reliable fault diagnosis approach, in case of multiple faults a more advanced technique for isolating faulty actuators and fault type determination is required.

- A fault recovery system may be developed for the formation flight of satellites that fulfills the mission objective. An automated or operator-initiated fault recovery procedure can be developed to correct the effect of fault in the system after detecting and isolating the fault and bring the formation system back to the normal state.

- Developing a fault detection system that is capable of detecting both the actuator and sensor faults can also be considered as a future work.

- In this thesis, the time delay in the communications among the satellites in the formation is ignored. By considering the communication time delays, the precision of the fault detection process can be increased.

- Developing a fault detection system that can continue to work in case of loss/failure of an agent in the formation flying missions is also suggested for future work.

Bibliography

[1] D. P. Scharf, F. Y. Hadaegh, and S. R. Ploen, "A survey of spacecraft formation flying guidance and control (part I): Guidance",*in Proceedings of the American control conference*, Denver, Colorado, Vol. 2, pp. 1733-1739, June 2003.

[2] L. S. Breger, "Model Predictive Control for Formation Flying Spacecraft",*Bachelor of Science Aeronautics and Astronautics thesis, Massachusetts institute of Technology*,June 2004.

[3] M. Jian, "Formation Flying of Spacecrafts for Monitoring and Inspection",*Master thesis, Lulea University of Technology*, September 2009.

[4] S. P. Hughes, "Formation Flying Performance Measures for Earth-Pointing Missions", *Master thesis, Virginia Polytechnic Institute and State University*, December 1999.

[5] J. Korbicz, K. Patan, and A. Obuchowicz, "Dynamic neural networks for process modelling in fault detection and isolation systems",*International Journal of Applied Mathematics and Computer Science*, vol. 9, pp. 519-546, 1999.

[6] A. Yazdizadeh and K. Khorasani, "Nonlinear system identification using embedded dynamic neural networks",*IEEE international joint conference on computational intelligence*, Anchorage, AK, vol. 1, pp. 378-383, May 1998.

[7] K. Patan and J. korbicz, "Application of dynamic neural networks in modelling and identification", 3rd *Int. Symp. Methods and Models in Automation and Robotics, MMAR'96*, Miedzyzdroje, Poland, vol. 3, pp. 1141-1146, 1996.

[8] A. Bernieri, M. D'Apuzzo, L.Sansone, and M. Savastano, "A neural network approach for identification and fault diagnosis on dynamic systems", *in IEEE transactions on Instrumentation and Measurement*, vol. 43, pp. 867-873, December 1994.

[9] V. Venkatasubramanian, R.Rengaswany, and K.Yin, "A review of Process Fault detection and diagnosis- Part I- Quantitative model-based methods", *Computers & Chemical Engineering*, Vol.27, No. 3, pp. 293-311, March 2003.

[10] V. Venkatasubramanian, R.Rengaswany, K.Yin, and S. N. Kavuri, "A review of Process Fault detection and diagnosis- Part II- Qualitative models and search strategies", *Computers & Chemical Engineering*, Vol.27, No. 3, pp. 313-326, March 2003.

[11] V. Venkatasubramanian, R.Rengaswany, K.Yin, and S. N. Kavuri, "A review of Process Fault detection and diagnosis- Part III- history based methods", *Computers & Chemical Engineering*, Vol. 27, No. 3, pp. 327-346, March 2003.

[12] R. Patton, P. Frank, and R. Clark (Eds), "Issues of fault diagnosis for dynamic systems", *Springer Verlag*, 2000.

[13] A. Barua, P. Sinha, and K. Khorasani, "A diagnostic tree approach for fault cause identification in the attitude control subsystem of satellites", *in IEEE Transactions on Aerospace and Electronic Systems*, vol. 45, No. 3, pp. 983-1002, 2009.

[14] Q. Cheng, P. K. Varshney, J. H. Michels, C. M. Belcastro, "Distributed fault detection with correlated decision fusion", *in IEEE Transactions on Aerospace and Electronic Systems*, Vol. 45, No. 4, pp. 1448-1465, 2009.

[15] Y. Zhang and X. R. Li, "Detection and diagnosis of sensor and actuator failures using IMM estimator", *in IEEE Transactions on Aerospace and Electronic Systems*, Vol. 34, no. 4, pp. 1293-1311, October 1998.

[16] T. Jiang, K. Khorasani, and S. Tafazoli, "Parameter Estimation-Based Fault Detection, Isolation and Recovery for Nonlinear Satellite Models", *IEEE Transactions on Control Systems Technology*, vol. 16, no. 4, pp.799-808, July 2008.

[17] R. Mehra, S. Seereeram, D. Bayard, and F. Hadaegh, "Adaptive Kalman filtering, failure detection and identification for spacecraft attitude estimation", *in Proceedings of IEEE Control Applications Conference*, Albany, NY, pp. 176-181, 1995.

[18] N. Meskin and K. Khorasani, "Fault Detection and Isolation in a redundant reaction wheels configuration of a satellite", *ISIC. IEEE International Conference on Systems, Man and Cybernetics*, Montreal, QC, pp. 3153-3158,October 2007.

[19] J. Gertler, "A cautious look at robustness in residual generation", *in Proceedings of the IFAC Symp. on Fault Detection, Supervision and Safety for Technical Processes*, Kingston Upon Hull, U.K, vol. 1, pp. 133-139, 1997.

[20] P. Ferguson and J. How, "Decentralized estimation algorithms for formation flying spacecraft", *AIAA Guidance, Navigation and Control Conference*, August 2003.

[21] S. Simani, C. Fantuzzi, and R. Patton, "Model-based Fault diagnosis in dynamic systems Using Identification Techniques", *in Volume Information and System Science*, London, U.K, Springer, 2003.

[22] A. Alessandri, "Fault diagnosis for nonlinear systems using a bank of neural estimators", *Computers in industry*, vol. 52, pp. 271-289, December 2003.

[23] T. Sorsa, H. N. Koivo, and H. Koivisto, "Neural networks in process fault diagnostics", *IEEE transactions on Systems, Man, and Cybernetics*, vol. 21, No. 4, pp. 815-825, 1991.

[24] T. Marcu and L. Mira, "Robust detection and isolation of the process faults using neural networks", *IEEE Control Systems Magazine*, vol. 17, No. 5, pp. 72-79, October 1997.

[25] M. H. Terra and R. Tinos, "Fault detection and isolation in robotic manipulators via neural networks: A comparison among three architectures for residual analysis", *Journal of Robotic Systems*, vol. 18, pp. 357-374, 2001.

[26] R. Tinos, M. H. Terra, and M. Bergerman, "Fault detection and isolation in cooperative manipulators via artificial neural networks", *in Proceedings of the IEEE International Conference on Control Applications (CCA '01)*, Mexico City, USA, pp. 492-497, 2001.

[27] I. A. D. Al-Zyoud and K. Khorasani, "Detection of actuator faults using a dynamic neural network for the attitude control subsystem of a satellite", *IEEE International Joint Conference on Neural Networks*, Montreal, QC, vol. 3, pp. 1746-1751, July 2005.

[28] Z. Q. Li, L. Ma, and K. Khorasani, "A Dynamic Neural Network-based Reaction Wheel Fault Diagnosis for Satellites", *International Joint Conference on Neural Networks (IJCNN '06)*, Vancouver, BC, pp. 3714-3721, 2006.

[29] H. A. Talebi, K. Khorasani, and S. Tafazoli, "A Recurrent Neural Network-based Sensor and Actuator Fault Detection, Isolation for Nonlinear Systems with Application to a Satellite's Attitude Control Subsystem", *IEEE Transactions on Neural Networks*, Vol. 20, No. 1, pp. 45-60, Jan. 2009.

[30] E. S. Tehrani, K. Khorasani, and S. Tafazoli, "Dynamic neural network-based estimator for fault diagnosis in reaction wheel actuator of satellite attitude control system", *in Proceedings of IEEE International Joint Conference on Neural Networks. IJCNN '05.*, Montreal, QC, vol. 4,pp. 2347-2352, August 2005.

[31] W. Ren and R. W. Beard, "Decentralized scheme for spacecraft formation flying via the virtual structure approach", *Journal of Guidance, Control, and Dynamics*, vol. 27, pp. 73-82, Jan 2004.

[32] M. Ayoubi, "Fault diagnosis with dynamic neural structure and application to a turbo-charger", *in Proceedings of International Symp. on Fault detection supervision and safety for technical processes, SAFEPROCESS'94*, Espoo, Finland, vol. 2, pp. 618-623, 1994.

[33] J. Korbicz, K. Patan, and A. Obuchowicz, "Network of dynamic neurons approach to residual generators",5th *Int. Symp. Methods and Models in Automation and Robotics, MMAR'96*, Miedzyzdroje, Poland, vol. 2, pp. 645-650, 1998.

[34] J. Korbicz, A. Obuchowicz and K. Patan, "Network of dynamic neurons in fault detection systems", *IEEE international conference on Systems, Man, and Cybernetics*, San Diego, CA, Vol. 2, pp. 1862-1867, 1998.

[35] M. Ayoubi, "Nonlinear dynamic systems identification with dynamic neural networks for fault diagnosis in technical processes", *IEEE conference on Systems, Man, and Cybernetics*, San Antonio, TX, vol. 3, pp. 2120-2125, 1994.

[36] K. S. Narendra and K. Parthasarathy, "Identification and control of dynamical systems using neural networks", *IEEE Transactions on Neural networks*, Vol. 1, no. 1, pp. 4-27, Mar 1990.

[37] X. M. Ren, A. B. Rad, and p. T. Chan, "Identification and control of nonlinear systems using dynamic neural networks", *in Proceedings of the 4th World Congress on Intelligent Control and Automation*, Shanghai, P.R.China, Vol. 3, pp. 2002- 2006, 2002.

[38] A. Yazdizadeh and K. Khorasani, "Nonlinear system identification using embedded dynamic neural networks", *IEEE International Joint Conference on Neural Networks*, Anchorage, AK, vol. 1, pp. 378-383, May 1998.

[39] A. M. Shaw, F. J. Doyle III, and J. S. Schwaber, "A dynamic neural network approach to nonlinear process modeling", *Computers & Chemical Engineering*, Vol. 21, No. 4, pp. 371-385, 1997.

[40] R. Isermann, "Supervision, fault-detection and fault-diagnosis methods An introduction", *Control Engineering Practice*, Vol. 5, No. 5, pp. 639-652, 1997.

[41] P. M. Frank and B. K. Seliger, "Fuzzy logic and neural network applications to fault diagnosis", *International Journal of Approximate Reasoning*, Vol. 16, No. 1, pp. 67-88, Jan 1997.

[42] M. Karpenko, N. Sepehri and D. Scuse, "Diagnosis of process valve actuator faults using a multilayer neural network", *Control Engineering Practice*, Vol. 11, Issue. 11, pp. 1289-1299, Nov. 2003.

[43] I. A. D. Al-Zyoud, "Neural network-based actuator fault detection and isolation for the attitude control subsystem of a satellite", *Master thesis, Concordia University*, 2005.

[44] J. Korbicz and K. Patan, "Dynamic neural networks with filter of different orders", 4th *Int. Symp. Methods and Models in Automation and Robotics, MMAR'97*, Miedzyzdroje, Poland, Vol. 2, pp. 745-750, 1997.

[45] A. Yazdizadeh, K. Khorasani, and R. V. Patel, "Identification of a two-link flexible manipulator using adaptive time delay neural networks", *IEEE Transactions on Systems, Man, and Cybernetics*, Vol. 30, no. 1, pp. 165-172, 2000.

[46] N. K. Sinha, M. M. Gupta, D. H. Rao, "Dynamic neural networks: an overview", *in Proceedings of IEEE International Conference on Industrial Technology*, Vol. 1, pp. 491-496, Jan 2000.

[47] D. H. Rao and M. M. Gupta, "Performance comparison of dynamic neural networks as applied to robot inverse kinematic computations", *American Control Conference*, Baltlmore, Maryland, Vol. 2, pp. 2153- 2157, June 1994.

[48] A. Yazdizadeh and K. Khorasani, "Adaptive time delay neural networks structures for nonlinear system identification", *Neurocomputing*, vol. 47, pp. 207-240, 2002.

[49] D. H. Rao and M. M. Gupta, "Dynamic neural unit and function approximation", *IEEE International Conference on Neural Networks*, San Francisco, CA, vol. 2, pp. 743-748, 1993.

[50] M. Hagan, H. Demuth and M. Beale, "Neural Network Design", *Boston London: PWS publisher*, 1996.

[51] D. H. Rao and M. M. Gupta, "A neural processor for coordinating multiple systems with dynamic uncertainties", *in Proceedings of the Second International Symposium on Uncertainty Modeling and Analysis*, College Park, MD, pp. 633-640, April 1993.

[52] K. Patan and T. Parisini, "Stochastic learning methods for dynamic neural networks: simulated and real-data comparisons", *in Proceedings of the American Control Conference*, Anchorage, AK, vol. 4, pp. 2577- 2582, 2002.

[53] K. Patan and T. Parisini, "Identification of neural dynamic models for fault detection and isolation: the case of a real sugar evaporation process", *Journal of Process Control*, Vol. 15, Issue. 1, pp. 67-79, Feb 2005.

[54] K. H. Bhavnani and R. P. Vancour, "Coordinate Systems for Space and Geophysical Applications", *Scientific report for Hanscom air force base*, No. 9, Massachusetts, Dec 1991.

[55] P. C. Hughes, "Spacecraft Attitude Dynamics", *Courier Dover Publications.*, Newyork, 2012.

[56] B. Wie, "Space vehicle dynamics and control", Reston, VA, *AIAA Education*, pp. 318-323, 1998.

[57] E. J. Overby, "Attitude control for the Norwegian student satellite nCube", *Master thesis, Department of Engineering Cybernetics, Norwegian University of Science and technology*, May. 2004.

[58] W. Ren and R. W. Beard, "Distributed consensus in multi-vehicle cooperative control: Theory and Applications", *Springerverlag London Limited*, 2008.

[59] J. T. Y. Wen and K. K. Delgado, "The attitude control problem", *IEEE Transactions on Automatic control*, Vol. 36, No. 10, pp. 1148-1162, Oct 1991.

[60] C. Kaplan, "Leo satellites: Attitude determination and control components; Some linear attitude control techniques", *Master thesis, Graduate School of Natural and Applied Sciences, Middle east Technical University*, Apr. 2006.

[61] J. L. Shwartz, "The Distributed Spacecraft Attitude Control System Simulator: From Design concept to Decentralized Control", *Doctor of Philosophy thesis, Virginia Polytechnic Institute and State University*, Jul. 2004.

[62] P. K. C. Wang and F. Y. Hadaegh, "Coordination and control of multiple microspacecraft moving in formation", *J. Astronautical Sci.*, vol. 44, no. 3, pp. 315-355, 1996.

[63] P. K. C. Wang, F. Hadaegh, and K. Lau, "Synchronized formation rotation and attitude control of multiple free-flying spacecraft", *AIAA Journal of Guidance and Control*, vol. 22, pp. 28-35, Jan 1998.

[64] F. Y. Hadaegh, W. M. Lu, and P. K. C. Wang, "Adaptive control of formation flying spacecraft for interferometry", *NASA Jet Propulsion Laboratory: Technical report*, 1998.

[65] Q. Yan, G. Yang, V. Kapila, and M. S. De Queiroz, "Nonlinear dyanamics and adaptive control of multiple spacecraft in periodic relative orbits", *AAS Guidance and Control Conference*, Breckenridge, CO, pp. 159- 174, 2000.

[66] M. S. De Queiroz, V. Kapila, and Q. Yan, "Adaptive nonlinear control of multiple spacecraft formation flying", *Journal of Guidance, Control, and Dynamics*, vol. 23, pp. 385-390, 2000.

[67] R. W. Beard, J. Lawton, and F. Y. Hadaegh, "A coordination architecture for spacecraft formation control", *IEEE Transactions on Control Systems Technology*, Vol. 9, no. 6, pp. 777-790, 2001.

[68] M. A. Lewis and K. H. Tan, "High precision formation control of mobile robots using virtual structures", *Autonomous Robots*, vol. 4, pp. 387-403, 1997.

[69] R. W. Beard and F. Y. Hadaegh, "Constellation templates: An approach to autonomous formation flying", *in Proceedings of World Automation Congress, ISIAC*, Anchorage, AK, pp. 177.1-177.6, May 1998.

[70] R. W. Beard, "Architecture and algorithms for constellation control", *Technical report: Jet Propulsion Lab., California Inst. Technol.*, Pasadena, CA, March 1998.

[71] C. R. McInnes, "Autonomous ring formation for a planar constellation of satellites", *Journal of Guidance, Control, and Dynamics*, vol. 18, no. 5, pp. 1215-1217, 1995.

[72] T. Balch and R. C. Arkin, "Behavior-based formation control for multi-robot teams", *IEEE Transactions on Robotics and Automation*, vol. 14, no. 6, pp. 926-939, 1998.

[73] X. Yun, G. Alptekin, and O. Albayrak, "Line and circle formation of distributed physical mobile robots", *Journal of Robotic Systems*, vol. 14, no. 2, pp. 63-76, 1997.

[74] C. Qin and J. Y. S. Luh, "Coordination and control of a group of small mobile robots", *in Proceedings of IEEE International Conference on Robotics and Automation*, San Diego, CA, vol. 3, pp. 2315-2320, May 1994.

[75] P. K. C. Wang, "Navigation strategies for multiple autonomous mobile robots moving in formation", *Journal of Robotic Systems*, vol. 8, pp. 177-195, 1991.

[76] B.J. Young, "Mobile robots: Coordination and control", *Master thesis, Brigham Young University*, 2000.

[77] B.J. Young, R.W. Beard, and J.M. Kelsey, "A control scheme for improving multi-vehicle formation maneuvers", *in Proceedings of the American Control Conference*, Arlington, VA, vol. 2, pp. 704-709, 2001.

[78] R. S. Smith and F. Y. Hadaegh, "Control topologies for deep space formation flying spacecraft", *in Proceedings of the American Control Conference*, Anchorage, AK, vol. 4, pp. 2836-2841, 2002.

[79] J. L. Speyer, "Computation and transmission requirements for a decentralized linear-quadratic-gaussian control problem", *IEEE Transactions on Automatic Control*, vol. 24, pp. 266-269, 1979.

[80] C. Brown, "Elements of Spacecraft design", *AIAA, Education series*, 2002.

[81] F. F. B. Zazzera, "Spacecraft Attitude Dynamics and Control, Course notes", *Politecnice de Milano*, Available at:
`http://www.aero.polimi.it/~bernelli/bacheca/didattica/ADCS_notes_part2.pdf`.

[82] R. Kristiansen, O. Egeland and P. J. Nicklasson, "A comparative study of actuator configuration s for satellite attitude control", *Modelling, Identification and Control*, vol. 26, no. 4, pp. 201-220, 2005.

[83] W. H. Clohessy and R. S. Wiltshire, "Terminal guidance system for satellite rendezvous", *Journal of the Aerospace Sciences*, Vol. 27, No. 9, pp. 653-658, 1960.

[84] B. Bialke, "High fidelity mathematical modeling of reaction wheel performance", 21st *Annual American Astronautical Society Guidance and Control Conference*, San Diego, CA, pp. 483-496, Feb. 1998.

[85] "Computer Science Knowledge Discovery in Database," Available at:
`http://www.cs.uregina.ca/simdbd/cs831/notes/confusion_matrix/`
`confusion_matrix.html`

[86] M. K. S. Alsamadi, K. B. Omar, and S. A. Noah, "Backpropagation Algorithm, the best algorithm among the multi-layer perceptron algorithm", *International Journal of Computer Science and Network Security (IJCSNS)*, vol. 9, No. 4, April 2009.

[87] D. P. Scharf, F. Y. Hadaegh, and S. R. Ploen, "A survey of spacecraft formation flying guidance and control. Part II: control", *in Proceedings of the American Control Conference*, Boston, MA, vol. 4, pp. 2976-2985, 2004.

[88] N. Tudoroiu and K. Khorasani, "Fault detection and diagnosis for satellite's attitude control system (ACS) using an interactive multiple model (IMM) approach", *in Proceedings of IEEE Conference on Control Applications*, Toronto, ON, pp. 1287-1292, Aug. 2005.

[89] H. A. Talebi, R. V. Patel, and K. Khorasani, "Fault detection and isolation for uncertain nonlinear systems with application to a satellite reaction wheel actuator", *IEEE International Conference on Systems, Man and Cybernetics*, Montreal, QC, pp. 3140-3145, Oct. 2007.

[90] H. A. Talebi and K. Khorasani, "An intelligent sensor and actuator fault detection and isolation scheme for nonlinear systems", 46th *IEEE Conference on Decision and Control*, New Orleans, LA, pp. 2620-2625, Dec. 2007.

[91] R. J. Patton, F. J. Uppal, S. Simani, and B. Polle, "Robust FDI applied to thruster faults of a satellite system", *Control Engineering Practice*, Vol. 18, Issue. 9, pp. 1093-1109, September 2010.

[92] A. Barua and K. Khorasani, "Hierarchical fault diagnosis and health monitoring in multi-platform space systems", *IEEE Aerospace conference*, Big Sky, MT, pp. 1-13, March 2009.

[93] A. Barua and K. Khorasani, "Multi-level fault diagnosis in satellite formations using fuzzy rule-based reasoning", 2nd *International Symposium on Systems and Control in Aerospace and Astronautics, ISSCAA* , Shenzhen, China, pp. 1-6, Dec. 2008.

[94] A. Joshi, V. Gavriloiu, A. Barua, A. Garabedian, P. Sinha, and K. Khorasani, "Intelligent and learning-based approaches for health monitoring and fault diagnosis of RADARSAT-1 attitude control system", *IEEE International Conference on Systems, Man and Cybernetics, ISIC*, Montreal, QC, pp. 3177-3183, October 2007.

[95] A. Valdes and K. Khorasani, "A pulsed plasma thruster fault detection and isolation strategy for formation flying of satellites", *Applied Soft Computing*, Vol. 10, Issue. 3, pp. 746-758, June 2010.

[96] P. Wang and F. Hadaegh, "Minimum-fuel formation reconfiguration of multiple free-flying spacecraft", *Journal of the Astronautical Sciences*, Vol. 47, no. 1, pp. 77-102, 1999.

[97] S. Li, R. Mehra, R. Smith, R. Beard, "Multi-spacecraft trajectory optimization and control using genetic algorithm techniques" *in Proceedings of IEEE Aerospace Conference* , Big Sky, MT, vol.7, pp. 99-108, 2000.

[98] R. Mehra and C. Sultan, "Path planning under collision avoidance constraints for formation flying missions", *International. Symp. Formation Flying Missions & Tech*, Toulouse, France, 2002.

[99] G. Singh and F. Hadaegh, "Collision avoidance guidance for formation flying applications", *in AIAA Guidance, Navigation, and Control Conference and Exhibit*, August 2001.

[100] D. P. Scharf, F. Y. Hadaegh, and B. Kang, "On the validity of the double integrator approximation in deep space formation flying", *in Int. Symp. Formation Flying Missions & Tech*, Toulouse, France, 2002.

[101] M. E. Campbell, "Planning Algorithm for large satellite clusters", *in Proceedings of AIAA Guidance, Navigation and Control Conference*, Monterey, CA, 2002.

[102] M. Campbell and T. Schetter, "Formation flying mission for the UW Dawgstar satellite", *in Proceedings of IEEE Aerospace Conference*, Big Sky, MT, vol. 7, pp. 117-125, 2000.

[103] C. D'Souza, "Optimal guidance law for formation flying and stationkeeping", *Journal of Guidance, Control, and Dynamics*, Vol. 23, No. 3, pp. 385-390, 2002.

[104] L. Mailhe, C.Schiff, and D. Folta, "Initialization of formation flying using primer vector theory", *in Int. Symp. Formation Flying Missions & Tech*, Toulouse, France, 2002.

[105] B. Engberg and R. Twiggs, "Operations Planning and Formation flying: Analyzing resource usage in formation assembly", *in AIAA/USU annual conference on small satellites*, Logan, UT, 1999.

[106] E. Atkins and Y. Pennecot, "Autonomous satellite formation assembly and reconfiguration with gravity fields", *in Proceedings of IEEE Aerospace Conference*, Vol. 2, pp. 783-796, 2002.

[107] L. Mailhe, C.Schiff, and S. Hughes, "Formation flying in highly elliptical orbits: Initializing the formation", *in Int. Symp. Space Flight Dyn.*, Biarritz, France, 2000.

[108] D. Folta and D. Quinn, "A 3-d method for autonomously controlling multiple spacecraft orbits" , *IEEE Aerospace Conference*, Snowmass at Aspen, CO, Vol. 1, pp. 51-60, March 1998.

[109] H. Schaub and K. Alfriend, "Impulsive spacecraft formation flying control to establish specific mean orbit elements", *J. Guid. Contr & Dyn.*, Vol. 24, No. 4, pp. 739-745, 2001.

[110] S. Vadali, H. Schaub, and K. Alfriend, "Initial conditions and fuel-optimal control for formation flying of satellites", *AIAA Guid., Nav., & Contr. Conf.*, 1999.

[111] T. Lovell and S. Tragesser, "Analysis of the reconfiguration and maintenance of close spacecraft missions", *in AAS/AIAA Space flight Mech*, 2003.

[112] C. McLaughlin, K. Alfriend, and T. Lovell, "Analysis of reconfiguration algorithms for formation flying experiments", *in Int. Symp. Formation Flying Missions & Tech*, Toulouse, France, 2002.

[113] S. Vadali and S. Vaddi, "Orbit establishment for formation flying of satellites", *in AAS/AIAA Space flight Mech*, pp. 181-194, 2000.

[114] M. Mesbahi and F. Hadaegh, "Formation flying control of multiple spacecraft via graphs, matrix inequalities and switching", *J. Guid. Contr & Dyn.*, Vol. 24, No. 2, pp. 369-377, 2001.

[115] M. Mesbahi and F. Hadaegh, "A robust control approach for the formation flying of multiple spacecraft", *in European Control Conf.*, matrix 10, no. 2, 1998.

[116] A. Robertson, G. Inalhan, and J. P. How, "Spacecraft formation flying control design for the Orion mission", *in Proceedings of AIAA Guidance, Navigation, & Control Conf.*, pp. 1562-1575, 1999.

[117] A. Robertson, G. Inalhan, and J. P. How, "Formation control strategies for a separated spacecraft interferometer", *in Proceedings of American Control Conference*, San Diego, California, pp. 4142-4147, 1999.

[118] P. K. C. Wang, J. yee, and F. Hadaegh, "Synchronized rotation of multiple autonomous spacecraft with rule-based controls, experimental study", *J. Guid. Contr & Dyn.*, Vol. 24, No. 2, pp. 352-359, 2001.

[119] R. H. Vassar and R. B. Sherwood, "Formation keeping for a pair of satellites in a circular orbit", *J. Guid. Contr & Dyn.*, Vol. 8, No. 2, pp. 235-242, 1985.

[120] C. C. Chao and H. Bernstein, "Onboard stationkeeping of geosynchronous satellites using a global positioning system receiver", *J. Guid. Contr & Dyn.*, Vol. 17, No. 4, pp. 778-786, 1994.

[121] D. C. Redding, N. J. Adams, and A. T. Kubiak, "Linear- Quadratic station keeping for the STS orbiter", *J. Guid. Contr & Dyn.*, Vol. 12, No. 2, pp. 248-255, 1989.

[122] M.S. de Queiraz, Q. Yan, G. Yang, and V. Kapila, "Global output feedback tracking control of spacecraft formation flying with parametric uncertainty," *in Proceedings of IEEE Conference on Decision and Control*, Phoenix, Arizona, USA, pp. 584-589, 1999.

[123] Q. Yan, G. Yang, V. Kapila, and M. S. de Queiroz, "Nonlinear dynamics and output feedback control of multiple spacecraft in elliptical orbits" *in Proceedings of American Control Conference*, Chicago, Illinois, pp. 839-843, 2000.

[124] F. Graziani, G. B. Palmerini, and P. Teofilatta, "Design and control strategies for global coverage constellations", *J. Brazilian Soc. Mech. Sci.*, vol. 16, pp. 181-187, 1994.

[125] G. B. Palmerini, "Guidance strategies for satellite formations," *AAS/AIAA Astrodynamics conference*, pp. 135-145, 2000.

[126] M. A. Lewis and K. H. Tan, "High precision formation control of mobile robots using virtual structures", *Autonomous Robots*, vol. 4, No. 4, pp. 387-403, 1997.

[127] M. Tillerson, L. Breger, and J. P. How, "Distributed coordination and control of formation flying spacecraft," *in Proceedings of IEEE American Control Conference*, pp. 1740-1645, 2003.

[128] P.K.C. Wang, "Navigation strategies for multiple autonomous mobile robots moving in formation", *Journal of Robotic Systems*, vol. 8, No. 2, pp. 177-195, 1991.

[129] M. R. Anderson and A.C. Robbins, "Formation flight as a cooperative game," *AlAA Guidance, Navigation and Control Conference*, Vol. 1, pp. 244-251, 1998.

[130] T. Baleh and R. C. Arkin, "Behavior-based formation control for multirobot teams", *IEEE Transactions on Robotics and Automation*, vol. 14, No. 6, pp. 926-939, 1998.

[131] F. Y. Hadaegh, A. R. Ghavimi, G. Singh, and M. Quadrelli, "A centralized optimal controller for formation flying spacecraft", *International Conference on lntel Technologies*, Bangkok, Thailand, 2000.

[132] J. L. Speyer, "Computation and transmission requirements for a decentralized linear-quadratic-gaussian control problem", *IEEE Transactions on Automatic Control*, vol. 24, No. 2, pp. 266-269, 1979.

[133] W. B. Dunbar and R. M. Murray, "Model predictive control of coordinated multi-vehicle formations," *IEEE Conference on Decision and Control*, Las Vegas, Nevada, USA, pp. 4631-4636, December 2002.

[134] O. Montenbruck and E. Gill, "Satellite Orbits: Models, Methods, and Applications", *Springer Verlag*, 2000.

[135] D. A. Vallado, "Fundamentals of Astrodynamics and Applications", Vol. 12, *Springer*, 2001.

[136] M. J. Sidi, "Spacecraft Dynamics & Control: A Practical Engineering Approach", Vol. 7, *Cambridge University Press*, 2002.

[137] L. King, G. Parker, S. Deshmukh, and J. H. Chong, "A study of interspacecraft coulomb forces and implications for formation flying", *Journal of Propulsion and Power*, Vol. 19, No. 3, pp. 497-505, 2003.

[138] E. Wnuk and J. Golebiewska, "Geopotential and luni-solar perturbations in the satellite constellation and formation flying dynamics", *Advances in the Astronautical Sciences*, Vol. 114, pp. 545-559, 2003.

[139] J. C. Hoskins, K. M. Kaliyur, and D. M. Himmelblau, "Fault diagnosis in complex chemical plants using artificial neural networks", *American Institute of Chemical Engineers Journal*, Vol. 37, No. 1, pp. 137-141, 1991.

[140] L. H. Ungar, B. A. Powell, and S. N. Kamens, "Adaptive networks for fault diagnosis and process control", *Computers and Chemical Engineering*, Vol. 14, pp. 561-572, 1990.

[141] V. Venkatasubramanian and K. Chan, "A neural network methodology for process fault diagnosis", *American Institute of Chemical Engineers Journal*, Vol. 35, No. 12, pp. 1993-2002, 1989.

[142] K. Watanabe, I. Matsura, M. Abe, M. Kubota, and D. M. Himmelblau, "Incipient fault diagnosis of chemical processes via artificial neural networks", *American Institute of Chemical Engineers Journal*, Vol. 35, No. 11, pp. 1803-1812, 1989.

[143] J. Y. Fan, M. Nikolaou, and R. E. White, "An approach to fault diagnosis of chemical processes via neural networks", *American Institute of Chemical Engineers Journal*, Vol. 39, No. 1, pp. 8288, 1993.

[144] A. E. Farell and S. D. Roat, "Framework for enhancing fault diagnosis capabilities of artificial neural networks", *Computers and Chemical Engineering*, Vol. 18, No. 7, pp. 613-635, 1994.

[145] C. S. Tsai and C. T. Chang, "Dynamic process diagnosis via integrated neural networks", *Computers and Chemical Engineering*, Vol. 19, pp. 747-752, 1995.

[146] W. Becraft and P. Lee, "An integrated neural network/expert system approach for fault diagnosis", *Computers and Chemical Engineering*, Vol. 17, No. 10, pp. 1001-1014, 1993.

[147] J. A. Leonard and M. A. Kramer, "Limitations of backpropagation approach to fault diagnosis and improvements with radial basis functions", *In AIChE annual meeting*, Chicago, 1990.

[148] B. R. Bakshi and G. Stephanopoulos,"Wave-net: a multiresolution, hierarchical neural network with localized learning", *American Institute of Chemical Engineers Journal*, Vol. 39, No. 1, pp. 57-81, 1993.

[149] T. Marcu, L. Mirea, and P. M. Frank, "Development of Dynamic Neural Networks With Application to Observer-Based Fault Detection and Isolation", *International Journal of Applied Mathematics and Computer Science*, Vol. 9, no. 3, pp. 547-570, 1999.

[150] L. Li, L. Ma and K. Khorasani, "A Dynamic Recurrent Neural Network Fault Diagnosis and Isolation Architecture for Satellites Actuator/Thruster Failures", *in Proceedings of second International Symposium on Neural Networks*, Chongqing, China, pp. 574-583, 2005.

[151] S. S. Tayarani-Bathaie, Z. N. Sadough Vanini, and K. Khorasani, "Fault detection of gas turbine engines using dynamic neural networks," 25th *IEEE Canadian Conference on Electrical & Computer Engineering (CCECE)*, Montreal, QC, pp. 1-5, April 2012.

[152] P. Frank, "Fault diagnosis in dynamic systems using analytical and knowledge-based redundancy: A survey and some new results," *Automatica*, Vol. 26, pp. 459-474, 1990.

[153] A. Valdes, "Dynamic Neural network-based pulsed plasma thruster (PPT) fault detection and isolation for the attitude control subsystem of formation flying satellites", *Master thesis, Concordia University*, 2008.

[154] G. W. Hill, "Researches in the lunar theory", *American Journal of Mathematics*, Vol. 1, pp. 5-26, 1878.